Spring 2018

Improving the performance of finned latent heat thermal storage devices using a Cartesian grid solver and machine-learning optimization techniques

Michael Augspurger
University of Iowa

IMPROVING THE PERFORMANCE OF FINNED LATENT HEAT THERMAL STORAGE DEVICES USING A CARTESIAN GRID SOLVER AND MACHINE-LEARNING OPTIMIZATION TECHNIQUES

by

Michael Augspurger

A thesis submitted in partial fulfillment
of the requirements for the Doctor of
Philosophy degree in Mechanical Engineering
in the Graduate College of the University of Iowa

May 2018

Thesis Supervisor: Professor H.S. Udaykumar

Graduate College
The University of Iowa
Iowa City, Iowa

CERTIFICATE OF APPROVAL

PH.D. THESIS

This is to certify that the Ph.D. thesis of

Michael Augspurger

has been approved by the Examining Committee
for the thesis requirement for the Doctor of Philosophy
degree in Mechanical Engineering at the May
2018 graduation.

Thesis Committee: _____

H.S. Udaykumar, Thesis Supervisor

_____

James Buchholz

_____

K.K. Choi

_____

Hongtao Ding

_____

Corey Markfort

ACKNOWLEDGEMENTS

Starting a new career at midlife requires the cooperation and support of a lot of people, both within and outside of the university. The faculty at Augustana College and the University of Iowa have not only been extremely helpful in teaching me to be an engineer, but in understanding the complications of my non-student-like daily life. Those on my committee—James Buchholz, K.K. Choi, Hongtao Ding, and Corey Markfort—deserve mention, as do my friends and teachers at Augustana—James Van Howe, Cecilia Vogel, Josh Dyer, Nathan Frank, and Stacey Rodman. My labmates—Jared, Nirmal, Aaron, Ehsan, Oishik, John, Pratik, Sid, Kayley, and Alexia, among others—have provided support, insight, and laughs. And I honestly could not have completed this project with the help of my advisor, H.S. Udaykumar: more than just providing direction for this project, he supplied helpings of patience and wisdom along the way.

But even more important, I have received unending support from my home. My wife Jane hardly blinked an eye when I told her I was thinking about quitting my first career so that I could start taking undergraduate-level physics courses. And while perhaps they did not know any better, my children Soli, Nat, and Toby found it perfectly natural that I should be starting 23rd grade in the fall when they were entering 1st,4th, and 6th.

ABSTRACT

The high energy density and stable temperature fields of latent heat thermal storage devices (LHTSD) make them promising in a range of applications, including solar energy storage, solar cooking, home heating and cooling, and thermal buffering. The chief engineering challenge in building an effective LHTSD is to find a way to complement the storage capabilities provided by the low-conductivity phase-change material with a suitable enhanced heat transfer mechanism.

The principal aim of this project is to develop a tool to improve the design of a small-scale LHTSD, such as one that might be used in solar cooking for a family. An effective small-scale storage device would need to absorb solar energy quickly, release the energy at a high temperature, be affordable, and be manageable within a small household. An LHTSD using solar salts fulfills the latter two requirements: solar salts, a near-eutectic mixture of $NaNO_3$ and KNO_3 (60/40% by mass) commonly used in thermal storage applications, are inexpensive and widely available, and the use of latent heat storage means a relatively small chamber can hold enough energy to cook a family meal. The challenge, however, is to design a device that absorbs and releases energy from the solar salts, which have a very low thermal conductivity. The most practical tool to improve the spread of heat through the salts is a finned metal core within the LHTSD.

This project uses numerical simulation to determine the most effective design of this finned core. A Cartesian grid solver is developed that is capable of simulating the convection-dominated melting processes within the storage device. The phase boundary is tracked using the enthalpy method, and conjugate heat transfer is calculated with a strongly coupled implicit scheme.

A number of techniques are then used to with this solver in order to better understand the factors that affect the performance of a LHTSD and to improve the design of such devices. The thesis is organized as an introductory section followed by three case

studies. In the first section, the project is introduced, and the governing equations and core numerical methods are described. In addition, a set of test simulations demonstrate that results using the developed numerical scheme match those of a range of experimental and numerical benchmarks.

Each of the case studies aims to adapt the numerical scheme to a more specific problem concerning LHTSDs. In the first, the performance of four fin designs are compared over long-term (48 hour) simulations; the aim is to test the potential performance of the four LHTSDs given realistic solar conditions in New Delhi, India. In the second case study, a set of physical experiments are performed in an empty and a finned LHTSD, and matched 3-dimensional numerical simulations are used to explore the thermal, melt, and flow behavior of the solar salts with the chambers. The final study uses the computational scheme to optimize the design of the finned core of an LHTSD over a large parameter space. To optimize the best design, the key parameters are first prescreened to find which three parameters have the largest effect on the objective equation. A machine-learning optimization code using the dynamic Kriging method (DKG) is then used to build a response surface from which the optimized design can be determined.

These three cases demonstrate the potential of the numerical scheme to explore the performance of finned LHTSD designs in a range of ways: the scheme can be used to predict behavior of devices in realistic conditions, to explore the behavior of solar salts during the melting and solidification process, and to determine an optimal design within a large parameter space. In doing so, they show the potential of this tool to help improve the performance and practicality of small-scale LHTSDs.

PUBLIC ABSTRACT

An effective means to store of solar energy as heat would help ameliorate the variability issues typical of solar-based energy systems. More specifically, the development of a device to store solar heat, even if only for a number of hours, would be a step towards the creation of a practical and convenient solar cooker.

Perhaps the most promising approach to inexpensive small-scale heat storage involves the use of phase change materials as a medium for thermal storage systems. Latent heat storage systems have the advantage of lower temperature ranges and higher rates of energy storage per unit volume than sensible heat storage devices. The most common, simple, and low-cost strategy uses highly conductive finned structures to help conduct heat into and out of the phase change material.

The main purpose of this thesis is to use numerical simulation and advanced optimization procedures to improve the design of a finned small-scale thermal storage device, such as one that might be used with a solar cooker. An effective storage device needs to absorb solar energy quickly, release the energy at a high temperature, be affordable, and be manageable within a small household. The simulations are used to predict behavior of devices in realistic conditions, to better understand phase change material behavior during the melting and solidification process, and to optimize the design of the storage device within a large parameter space. The thesis demonstrates the potential of this approach to improve the efficiency and practicality of small-scale thermal storage devices.

TABLE OF CONTENTS

LIST OF TABLES

LIST OF FIGURES

INTRODUCTION

For several decades, there has been a growing interest in developing inexpensive, clean and efficient cook stoves for use in the developing world. This growing interest draws its impetus from the fact that traditional cooking methods create significant economic, environmental, and health problems for communities around the world. The World Health Organization, for instance, reports that cooking smoke, trapped indoors in the cooking process, leads to approximately two million deaths a year, the vast majority of which take place in low or middle income countries [5]. Excessive harvesting of fire wood in areas with growing populations leads to deforestation and its accompanying environmental problems, and this deforestation in turn leads to the need, particularly among women and children, to spend a significant portion of the day in search of cooking fuel [6]. Finally, the shortage of wood means that these individuals have less time to pursue longer term economic viability through education or cottage industry work [7].

Solar cookers, in particular, offer an ideal solution to this problem: smokeless cooking done with abundant free energy. Engineers have done impressive technical work developing a range of efficient and workable solar cookers [8-10]. But this has not let to the widespread adoption of solar cookers [11]. The chief cause of this failure is that the existing cookers have required that their users adapt their community cooking habits to the needs of the cooker. Cooking methods, available food, and traditional foods in developing areas are often quite particular to that community: many solar cooker designs do not take these particularities into account, and so people have been reluctant to adopt them. In response to this problem, there has been a more recent push to consider a "holistic framework" or "end-user" approach in designing a cooker and evaluating its success [6, 7, 12, 13]. This has led some solar cooker researchers, for instance, to test the effectiveness of their cookers in the context of local food cultures [14, 15].

One result of this change in approach is a renewed interest in developing solar cookers that can provide a source of heat in the evening and morning. It is not surprising that most people, especially those in areas that might benefit most from solar cooking, traditionally prepare meals indoors and when the sun is not at its peak. Many solar cookers, though, require that cooking take place during the day and in the outdoors. The development of an effective means to store solar heat, even if only through the evening hours, would be a step towards the creation of an attractive, end-user adapted cooker [16].

Perhaps the most promising approach to inexpensive small-scale heat storage involves the use of phase change materials (PCM) as a medium for thermal storage systems [17-19]. Latent heat storage systems have the advantage of lower temperature ranges and higher rates of energy storage per unit volume than sensible heat storage devices. Because the solidification process occurs over a significant time period at a known heat of solidification, they also offer the possibility of a long-lasting, steady-temperature source for cooking [8, 20-22]. More generally, thermal storage in solar power plants and cookers is extremely useful to ameliorate the variability issues typical of solar-based energy systems and to provide energy on demand [23-26].

However, the design of an efficient small-scale latent heat solar thermal storage device (LHTSD) presents significant challenges. A central difficulty in building an effective LHTSD lies in the low thermal conductivity of most phase change materials. In order to melt the PCM as quickly as possible and to draw heat rapidly from the storage during discharge, it is necessary to find a way to move heat efficiently into and out of the device. Investigators have suggested numerous ways to do this, including the use of microencapsulation, interspersed high conductivity particles, and metal matrices, among others [27-32].

However, the most common, simple, and low-cost strategy uses highly conductive finned structures to help conduct heat into and out of the PCM [33-39]. For solar cookers, this approach seems the most promising for two reasons. First, such cookers depend on

concentrated solar energy on a single receiving surface. As a result, it is necessary that the heat transfer enhancement technique be adaptable to the asymmetry of the temperature field, which is difficult to achieve using techniques such as high conductivity particles or a metal matrix. As a result, the finned core offers the best strategy to move large amounts of energy from the receiving surface into the interior of the LHTSD. Second, because the cost and the ease of construction and maintenance of the device must be kept in mind if a cooker is to be widely adopted, the simpler technology of a finned core is preferable to more recent technological developments such as microencapsulation.

Significant work has been done in recent years on using fins to enhance latent heat thermal storage [34, 35, 38-41]. Most of these works demonstrate the effectiveness of fins as a conduction enhancement strategy. Nearly all of them, however, acknowledge the heavy dependence of the effectiveness of the fins on the overall geometry of the model itself. Thermal behavior in phase change systems is highly dependent not only on viscosity and conductivity of the materials, but also on aspect ratio, container size, and specific geometry [33]. In other words, while the shape, length, volume, and placement of the fins is crucial to performance, there are no clear rules for fin design that apply across the myriad variations in PCM characteristics, container geometry, container material properties, and boundary conditions.

The complex interactions amongst these design variables make it difficult to compare the effectiveness of different cooker designs [42]. In addition, dependable experimental results can be difficult to attain, because of the difficulties in observing and evaluating temperature fields, melting fronts, and convection patterns within a solid, opaque LHTSD. These complications make numerical optimization appealing, and indeed much recent work on solar thermal storage devices has been done using simulations [18, 25, 36, 43, 44].

But simulation of latent heat thermal storage comes with its own challenges. First, these simulations must deal with complex geometries and moving melt boundaries; these

factors complicate the meshes necessary to perform computations, and can lead to time-consuming meshing processes, convergence issues, and/or longer run times. Second, a robust conjugate heat transfer treatment is needed to handle the vastly different temperature gradients at the interface between the highly conductive fins and the latent heat medium. And finally, the low diffusivity of the latent heat medium means that heat transfer within that medium will be heavily dominated by convection, leading to significantly different time and length scales for the movement of heat within the liquid (molten) salt, within the solid salt, and within the metal fins

First, to deal with meshing problems, this work employs an adaptive locally refined octree Cartesian mesh [45] that both allows the grid to adapt to the changing mesh interface and eliminates the need to create a mesh for the multiple complex geometries that would be used in a design optimization process. Like much recent work [36, 46-51], the melting boundary here is tracked using the well-established enthalpy-porosity method [33, 52]. But the present work differs in its approach to the computational grid. Some research on PCM simulations have used finite element approaches [39, 50], but most recent work on simulations of the melting of PCMs with fins has used fixed grids [34-36, 38, 40, 41]. The chief problem with a fixed grid, whether uniform or not, is that the entire field must be meshed as if it were an area of high gradients, anticipating that such gradients will arise during the evolution of the phase change process. The current work circumvents the burden of utilizing a computationally onerous fine mesh by using a locally and dynamically refined Cartesian mesh grid; in this case the grid can be refined in the interface region as the simulation advances (see Figure 1). In the initial stages of a frozen simulation, for example, the grid can be very coarse since convection is weak and heat transfer is dominated by conduction. But as the simulation develops, the grid is refined to match local conditions within the field, which leads to a better balance of efficiency and accuracy in simulations. In addition to allowing a more efficient grid throughout a phase-change simulation,

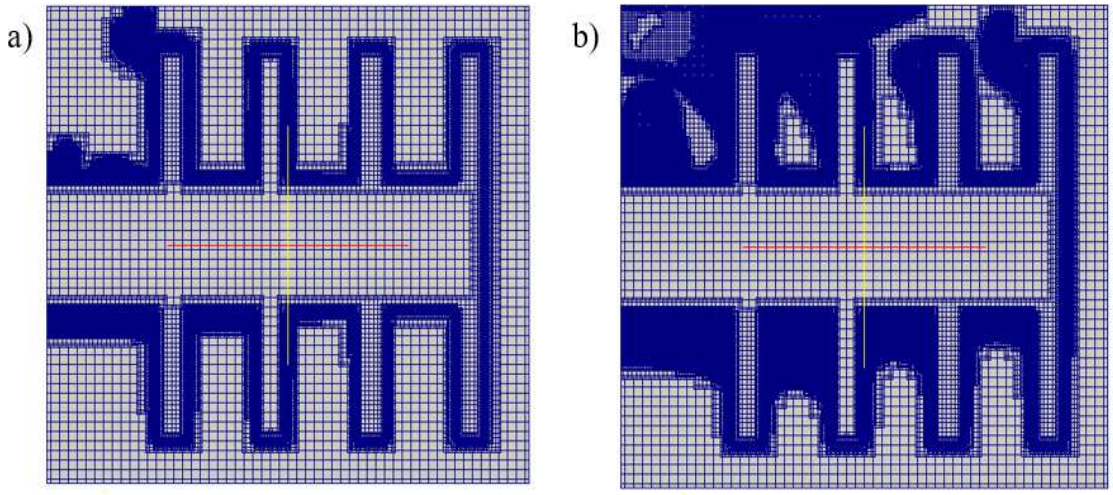

Figure 1. Mesh for LHTSD design at early (a) and later (b) stage of melting.

dynamically refined Cartesian meshes offer the advantage of alleviating mesh generation issues when a large number of geometrical models are used, such as in optimization studies.

The second major challenge for numerical simulations of melting PCMs is the transfer of heat from the highly conductive fin material into the low conductivity salts. In this work, the conjugate heat transfer is handled using a fully implicit single-field method: the robustness of this method allows the solver to handle complex geometries and highly disparate conductivities. The interface conditions at the aluminum-salt interface are handled with a sharp interface approach, which extends the methods presented in [53, 54]. These processes are complicated, however, by the use of a dynamic Cartesian grid. With a fixed non-Cartesian grid, the grid points can be designed to lie along the interface between the PCM and the fin material, which means that boundary conditions can be set along that boundary. Some algorithms separate the temperature field into two fields (one for PCM, one for fin material) [37, 41], while others solve all temperatures simultaneously [34, 40],

but both approaches apply boundary conditions directly at the interface. With a Cartesian grid, however, this is not possible, since the grid points are generally not coincident with the interface. Therefore, techniques must be developed to treat conjugate heat transfer at sharp interface robustly in the presence of an adaptively refined mesh.

Still, this work shows that the combination of the adaptive Cartesian grid and the single field implicit solution to conjugate heat transfer leads to a robust and efficient treatment of the interface. And while adaptive Cartesian grid methods have been used to simulate phase change [45, 55-60], the current work is the first application of these methods to the optimal design of LHTSDs with embedded fin structures. For such applications, the approach is attractive. First, it enables quick turnaround on geometry changes, since no grid generation is required; this is particularly important for optimization processes, which require a high number of simulations with different geometries. Furthermore, its efficient use of highly refined grid spaces allows the simulation of larger, more complex geometries. And finally, its implicit solution process for the conjugate heat transfer problem is robust and efficient.

The third challenge with which these simulations must grapple is created by the vastly different time and length scales inherent in a simulation of a LHTSD. On one hand, the real time scales for the solar cookers are very long: to simulate the charging of the LHTSD, for instance, it is necessary to simulate the hours between sunrise and sunset. In order to simulate thermal storage and discharge, at minimum a twenty-four hour simulation is needed. On the other hand, a LHTSD designed to cook two meals and hold its heat overnight must be large: some of the simulations in this work are based on a LHTSD with an approximately 30 liter cylindrical container. These large time and length scales are in contrast to the small scales of the flow: the complex fin geometries, high temperature gradients, thin initial melt volumes, and strong convection patterns necessitate small time steps and a fine computational mesh. Simulations combining these different time and length scales requires significant parallel computer resources and a robust simulation code.

One contribution of the current work is to demonstrate the feasibility of direct Navier-Stokes simulations of full-scale latent-heat solar thermal storage devices.

This project is structured as an introductory section followed by three case studies. In the introductory section, the governing equations and core numerical methods are described, and a set of test simulations demonstrate that results using the developed numerical scheme match those of a range of experimental and numerical benchmarks. The three case studies then adapt the numerical scheme to a particular problem concerning LHTSDs. First, the performance of a small number of designs are compared over long-term (48 hour) simulations; the aim is to test the potential performance the designs assuming realistic solar conditions. In the second case study, physical experiments are performed in an empty and a finned LHTSD; 3-dimensional numerical simulations are designed to match the temperature-field results of the experiemnts, and the results are used to explore the thermal, melt, and flow behavior of the solar salts. The final study aims to optimize the design of the horizontally-finned core over a large parameter space. The key parameters are first prescreened to find which three parameters have the largest effect on the efficiency of the LHTSD. A response surface is then constructed using the dynamic Kriging method; this response surface is analyzed to find the optimal chamber design.

These case studies show the capability of the numerical scheme to explore the performance of finned LHTSD designs. Simulations can be used to predict behavior of devices in realistic conditions, to better understand PCM behavior during the melting and solidification process, and to optimize the design of the LHTSD within a large parameter space. They demonstrate in the process the potential of this approach to improve the efficiency and practicality of small-scale LHTSDs.

CHAPTER ONE
BENCHMARKING AND INITIAL TESTING

This first chapter explains the numerical scheme used throughout the thesis. Furthermore, it compares simulation results using this code to experimental and numerical benchmarks for conjugate heat transfer and melting boundary behavior. Finally, simulations of two finned LHTSD designs are performed to demonstrate the capability of this approach to evaluate the behavior of small-scale LHTSDs.

1.1 Numerical Methods

1.1.1 Governing Equations

For numerical ease, the simulations in the first chapter use a non-dimensionalized set of equations. In these cases, the characteristic length L_0 is the height of the container L, while characteristic velocity u_o is $(g\beta\Delta TL)^{1/2}$, where g is the gravitational force, and β is the coefficient of expansion. As the test and benchmark simulations all involve a chamber at an initial temperature T_{init} heated at 1-2 walls that are at a higher temperature T_{wall}, ΔT is set as T_{wall}-T_{init}. The characteristic pressure p_o and time t_o are ρu_o^2 and L/u_o, respectively, where ρ is the density. The resulting non-dimensional mass balance equation is:

$$\frac{\partial U}{\partial X} + \frac{\partial V}{\partial Y} = 0 \qquad (1)$$

where U and V are the non-dimensional velocities. The momentum balance equations are:

$$\frac{\partial U}{\partial \tau} + \frac{\partial (UU)}{\partial X} + \frac{\partial (UV)}{\partial Y} = -\frac{\partial P}{\partial X} + \left(\frac{1}{Gr^{\frac{1}{2}}}\right)\left(\frac{\partial^2 U}{\partial X^2} + \frac{\partial^2 U}{\partial Y^2}\right) + AU \qquad (2)$$

$$\frac{\partial V}{\partial \tau} + \frac{\partial (UV)}{\partial X} + \frac{\partial (VV)}{\partial Y} = -\frac{\partial P}{\partial Y} + \left(\frac{1}{Gr^{\frac{1}{2}}}\right)\left(\frac{\partial^2 V}{\partial X^2} + \frac{\partial^2 V}{\partial Y^2}\right) + AU + \theta \quad (3)$$

In the above, Pr ($(\nu\rho C_p)/k$) is the Prandtl number, Gr ($(g\beta\Delta TL^3)/\nu^2$) is the Grashof number, C_p is the specific heat and ν is the kinematic viscosity. θ is the non-dimensionalized temperature, which is defined as $(T - T_{init})/(T_{wallt} - T_{init})$, where T_{init} is the temperature of PCM and fin structure at $\tau = 0$ and T_{wall} is a characteristic temperature defined by the particular simulation (e.g., temperature of a heated wall).

The nondimensionalized energy balance equation is:

$$\frac{\partial \theta}{\partial \tau} + U\frac{\partial \theta}{\partial X} + V\frac{\partial \theta}{\partial Y} = \left(\frac{1}{Gr^{\frac{1}{2}}Pr}\right)\left(\frac{\partial^2 \theta}{\partial X^2} + \frac{\partial^2 \theta}{\partial Y^2}\right) + \left(\frac{1}{St}\right)\left(\frac{\partial F_{liquid}}{\partial \tau}\right) \quad (4)$$

where St ($(C_p\Delta T)/L$) is the Stefan number.

1.1.2 Discretization Scheme

The nonlinearity of the above equations requires that they be discretized and solved numerically. The two-dimensional governing equations are discretized using an implicit second-order central differencing scheme, in which continuity is enforced using a pressure-based velocity correction scheme. In the first part of the fractional-step method, the intermediate velocity $\vec{u}^*$ is determined using the following discrete form of the momentum equation:

$$\alpha_1 \vec{u}^* + \alpha_2 \vec{u}^{n-1} + \alpha_3 \vec{u}^{n-2} + H^{n,k-1} = -\nabla p^{n,k-1} + Gr^{-\frac{1}{2}} \nabla^2 \vec{u}^n + A\vec{u}^n + T^{n,k-1}\hat{k} \quad (5)$$

Here n is the current time step, k is the current iteration within the time step, α is a time-step related coefficient, $\hat{k}$ is the unit vector in the direction of gravity, and A is the Carmen-Kozeny term described above. The liquid fraction value used for the Carmen-Kozeny term is a time-projected value based on the liquid fraction value from the previous two steps.

The convection term H is discretized using a second-order central differencing method and is treated explicitly. The α coefficients are time-stepping coefficients, and are defined as:

$$\alpha_1 = \frac{2\,\Delta t^n \Delta t^{n-1}}{\Delta t^{n+1}{}^2 + \Delta t^n \Delta t^{n+1}} \qquad \alpha_2 = \frac{-\Delta t^n - \Delta t^{n-1}}{\Delta t^n\,\Delta t^{n-1}} \qquad \alpha_3 = \frac{2\,\Delta t^n \Delta t^{n-1}}{\Delta t^{n-1}{}^2 + \Delta t^n \Delta t^{n-1}} \tag{6}$$

where Δt^n is the time step for the current step and Δt^{n-1} is that for the previous step. Separating the explicit and implicit terms, the equation becomes:

$$(\alpha_1 - A - Gr^{-\frac{1}{2}}\nabla^2)\,\vec{u}^* = -\nabla p^{n,k-1} - \alpha_2\,\vec{u}^{n-1} - \alpha_3\,\vec{u}^{n-2} - H^{n,k-1} - T^{n,k-1}\hat{k} \tag{7}$$

It is important for sake of convergence that the liquid fraction coefficient A be moved into the coefficient matrix (as cast in equation (8)) as opposed to being retained in the source term. This prevents small changes in velocity from iteration to iteration from causing large changes in the source term, which can lead to problems with convergence. The right hand side of the discretized equation consists of the explicit terms. The discrete momentum equation (7) is then solved to find the intermediate velocity field $\vec{u}^*$.

In the second step, $\vec{u}^*$ is corrected by an imposed pressure field that ensures that the velocity field is divergence free. This is done by using a Helmholtz decomposition to set the final divergence-free velocity field $\vec{u}^n$ equal to the intermediate velocity field plus an irrotational velocity correction formed by the gradient of the scalar φ:

$$\vec{u}^n = \vec{u}^* + \frac{\nabla\varphi}{\alpha_1} \tag{8}$$

α_1 is a time step coefficient defined exactly as in equation (6) above. Since the divergence of $\vec{u}^n$ is zero, taking the divergence of equation (8) leads to the Poisson equation:

$$\nabla^2\varphi = -\alpha_1\,\nabla\,\vec{u}^* \tag{9}$$

This equation is solved for φ, and the final pressure and final velocity are determined using a rotational pressure correction scheme to find the pressure, viz.:

$$\vec{u}^n = \vec{u}^* - (\frac{1}{\alpha_1})\nabla\varphi \tag{10}$$

$$p^n = \varphi - \nu \nabla \cdot \vec{u}^n \tag{11}$$

As noted above, in the momentum equation the solid-liquid embedded interface is accounted for using a sharp interface method [53, 54, 60, 61] without the use of forcing terms to account for interface boundary conditions.

The phase-change boundary is determined using the enthalpy-porosity method [51, 52, 62, 63]. After the velocity and pressure fields are finalized, enthalpy is calculated for each cell and this is used to find F_{liquid}. Enthalpy h^n is defined as:

$$h^n = C_p\, T^{n,k-1} + \gamma\, F_{liquid}^{n,k-1} \tag{12}$$

In the above, γ is the latent heat of the PCM, while C_p is its constant specific heat. The liquid fraction F_{liquid} is then set according to this enthalpy value:

$$F_{liquid} = \begin{cases} 0, & if\ h^n < h^{frozen} \\ \dfrac{h^n - h^{frozen}}{2C_p\varepsilon + \gamma}, & if\ h^{frozen} < h^n < h^{melted} \\ 1, & if\ h^n > h^{melted} \end{cases} \tag{13}$$

The temperature interval ε represents half of the phase change temperature range (i.e. the "mushy" region). $h^{frozen} = C_p\,(T_{melt} - \varepsilon)$ is the enthalpy of a completely frozen cell at the lower bound of the mushy region, and $h^{melted} = C_p\,(T_{melt} + \varepsilon) + \gamma$ is the enthalpy of a completely melted cell at the upper bound of this region.

The discretized energy equation is:

$$\left(\alpha_1 - \left(\frac{1}{PrGr^{\frac{1}{2}}}\right)\nabla^2\right) T^n = \alpha_2 T^{n-1} - \alpha_3 T^{n-2} + H^{n,k-1} + \left(\frac{1}{St}\right)\left(F_{liquid}^{n,k-1} - F_{liquid}^{n-1}\right) \tag{14}$$

The αs are time-stepping coefficients as in equation (7). The convection term H is calculated explicitly using a second-order central differencing scheme. The liquid fraction source term is calculated explicitly using the liquid fraction value from the previous

iteration. The Laplacian on the left hand side is discretized using a second-order central differencing scheme.

1.1.3 Conjugate Heat Transfer

The temperature at each point in the field away from the interface is calculated using a standard 5-point stencil in two dimensions (see figure 1) and the discretization in equation (14) above. However, if any of the 4 neighbors of a point (i, j) lie in a material different from (i, j), the point is defined as an interface point. In this case, the discretization of the energy equation is treated using a sharp interface formulation and a conjugate heat transfer treatment at the interface between the two materials.

The boundary conditions at the interface are:

$$T_{interface,mtrl1} = T_{interface,mtrl2} \qquad k_{mtr1}\frac{\partial T}{\partial n} = k_{mtr2}\frac{\partial T}{\partial n} \qquad (15)$$

k_{mtrl1} and k_{mtrl2} are the thermal conductivity of the first and second materials. n is the vector normal to the interface in the direction from material one to material two.

For an interface point (i,j), some neighboring points are in the same material, while others are in the opposing material. Because the temperature gradient across the interface depends on the k_{mtrl1}, k_{mtrl2}, and the placement of the interface, it is necessary to identify a "ghost" temperature value for the points in the opposing material. The ghost value is the temperature value at the neighboring point if the temperature field in the (i,j) material were extended into the opposing material. With a ghost value specified, the temperature at (i,j) can be solved as in the case of a single material in the same way as for a bulk/ interior point. For example, discretizing the Laplacian in the left hand side of equation (14) for point $x_{i,j}$ in Figure 2 with a second-order central differencing scheme leads to:

$$(\alpha_1 + 4\beta)T_{i,j} - \beta T_{i-1,j} - \beta T_{i,j-1} - \beta T_{i+1,j,ghost} - \beta T_{i,j+1,ghost} \quad (16)$$
$$= \alpha_2 T^{n-1} - \alpha_3 T^{n-2} + H^{n,k-1} + \left(\frac{1}{St}\right)(F_{liquid}^{n,k-1} - F_{liquid}^{n-1})$$

where $\beta = \left(\frac{1}{\mathrm{Pr}*\mathrm{Gr}^{\frac{1}{2}}}\right)(\frac{1}{\Delta x^2})$.

However, to solve the temperature as a single field, it is necessary to obtain the ghost temperatures in terms of the "real" temperature field. For example, the ghost temperature for a neighboring point, say $x_{i,j+1,}$ is the temperature value at that point if the temperature field from $x_{i,j}$ to the interface along the gridline were to be extended all the way to $x_{i,j+1}$. Therefore, the ghost temperature at the point $x_{i,j+1}$ in Figure 2, written in terms of the "real" temperature field and the interface temperature, is:

$$T_{i,j+1,ghost} = \left(1 + \frac{L_{i,j+1}}{L_{i,j}}\right)T_{interface} - \left(\frac{L_{i,j+1}}{L_{i,j}}\right)T_{i,j} \quad (17)$$

where $L_{i,j}$ is the distance between point $x_{i,j}$ and the interface in the direction of $x_{i,j+1}$ and $L_{i,j+1}$ is the distance between the interface and the point $x_{i,j+1}$. Note that the ghost value now depends on the interface temperature which is provided by the boundary conditions.

Combining the boundary conditions with equation (15) produces a definition of $T_{interface}$ in terms of the real temperatures at $x_{i,j}$ and $x_{i,j+1}$:

$$T_{interface} = \frac{(T_{i,j+1} + Z\,T_{i,j})}{1+Z}, where\ Z = (\frac{L_{i,j+1}}{L_{i,j}})(\frac{k_{i,j}}{k_{i,j+1}}) \quad (18)$$

Note that Z is nothing but the ratio of thermal resistances for the materials across the interface. Inserting equation (18) into equation (17) produces a definition of the ghost temperature in terms of the real temperatures at $x_{i,j}$ and $x_{i,j+1.}$

$$T_{i,j+1,ghost} = \frac{\left(1 + \left(\frac{L_{i,j+1}}{L_{i,j}}\right)\right)(T_{i,j+1} + Z\,T_{i,j})}{1+Z} - \left(\frac{L_{i,j+1}}{L_{i,j}}\right)T_{i,j} \quad (19)$$

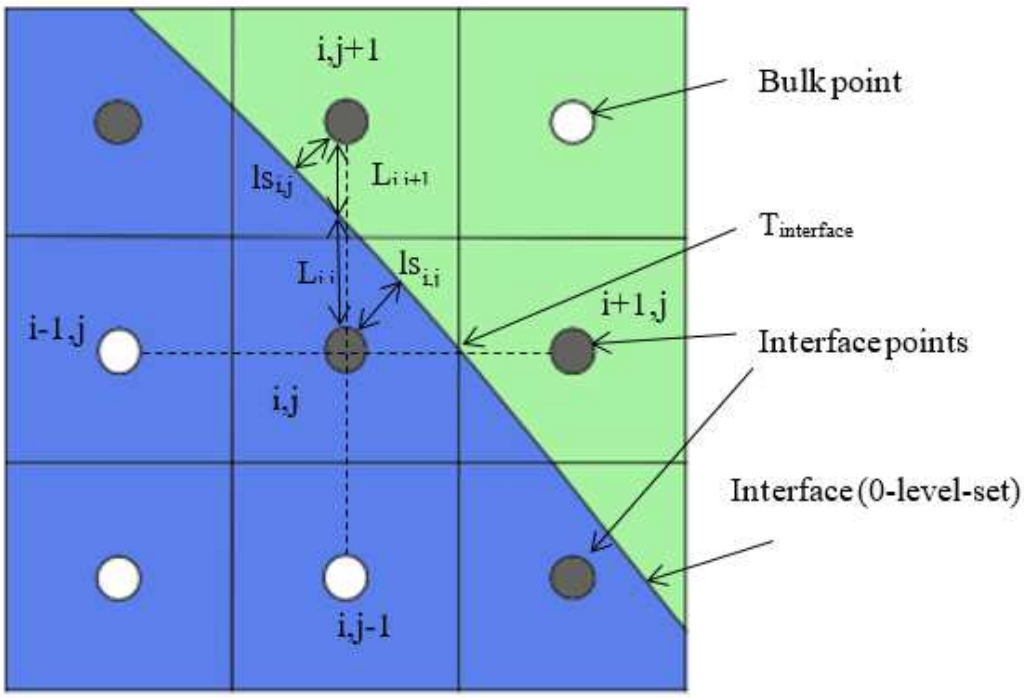

Figure 2. A typical cell configuration near the two material interface. The dotted lines show the 5 point stencil for a point i,j: if one or more of the dotted gridlines cross the interface, the point is defined as an interface point.

With this equation, the ghost temperature of any neighboring point in the opposing material can be replaced with the real temperature values in discrete form of the energy equation.

The remaining issue in equation (19) is to find the resistance ratio parameter Z. To find Z, it is noted that the ratio of level-set values such as $ls_{i,j}$ and $ls_{i,j+1}$ in Figure 2 are much more efficiently accessed than one of gridline lengths such as $L_{i,j}$ and $L_{i,j+1}$. In addition, these two ratios are equal with the assumption that the interface boundary is linear in the region of opposing grid points (i.e. there are no sharp corners). As a result, in implementation it is convenient to use a ratio of level-sets in evaluating the parameter Z:

$$Z = \left(\frac{ls_{i,j+1}}{ls_{i,j}}\right)\left(\frac{k_{i,j}}{k_{i,j+1}}\right) \tag{20}$$

where $k_{i,j}$ and $k_{i,j+1}$ are the thermal conductivities in the two materials.

In this way, the boundary temperatures are solved implicitly with the rest of the temperature field. The implicit approach proves to be crucial in stiff problems such as the conjugate gradient cases studied here.

1.1.4 Essentially Non-oscillatory (ENO) Convection Scheme

Several characteristics of the simulations in this work lead to numerical stiffness and very quickly to oscillations in the temperature fields. These characteristics include the large difference in thermal diffusivity across the aluminum-salt interface, the narrow melted region that occurs early in simulations, and the fact that the highest velocity and temperature gradients, particularly with vertical geometries, occur next to the solid interface. As a result, it is necessary to include schematic devices that can tamp down the resulting temperature oscillations without losing significant accuracy.

The primary tool used to alleviate oscillations is a second-order essentially non-oscillatory (ENO) convection scheme [64]. The ENO scheme works by first determining whether a significant oscillation exists at each point; if there is an oscillation, the central differencing discretization is replaced by an upwinding discretization, which adds further artificial diffusion. Divided differences are used to determine whether an upwind or central discretization should be used. The first step uses divided differences to calculate whether the temperature field is smoother within the three points centered at the point itself, or the three points centered at its upwind neighbor. At point i the divided difference D is calculated as:

$$D_i = \frac{\frac{(T_{i+1} - T_i)}{\Delta x_{i+1}} - \frac{(T_i - T_{i-1})}{\Delta x_i}}{\Delta x_{i+1} + \Delta x_i} \tag{21}$$

Assuming that Δx is constant in the region of the main point, as it always is in areas of high temperature and velocity gradients, we can remove the Δx terms from the equation. The simplified divided difference d reduces to:

$$d_i = T_{i+1} - 2T_i + T_{i-1} \tag{22}$$

This result is compared to the simplified divide difference at the upwind neighbor:

$$d_{upwind} = T_{i-2} - 2T_{i-1} + T_i \tag{23}$$

where for notation purposes cell $i-1$ is assumed to be upwind of i. The results of these calculations determine whether a central difference or upwind scheme (both second-order) will be used to calculate the gradient of the temperature. A large divided difference at i indicates the presence of oscillations, and in that case, the upwind scheme is used to introduce further artificial diffusivity. The convection term is discretized as such, assuming here a velocity moving in the positive direction:

$$u\frac{\partial T}{\partial x} = \begin{cases} u_i\left(\frac{T_{i+1} - T_{i-1}}{2\Delta x}\right), if\ d_i \geq C * d_{upwind} \\ u_i\left(\frac{3T_i - 4T_{i-1} + T_{i-2}}{2\Delta x}\right), if\ C * d_{upwind} > d_i \end{cases} \tag{24}$$

where C is a coefficient controlling the amount of upwinding used. If C = 0, no upwinding is used, while if it is well above 1, upwinding is used much more often. In these simulations, C is set to 1. The scheme works by moderating the temperatures of cells that are out of sync with the surrounding cells. For instance, if the cell *i* is warmer than both its neighbors, it will be marked for upwinding. As a result, its outflux will be higher than it would be otherwise $\left(u_{i+\frac{1}{2}}T_i > u_{i+\frac{1}{2}}T_{i+\frac{1}{2}}\right)$ and its influx will be smaller $\left(u_{i+\frac{1}{2}}T_{i-1} < u_{i+\frac{1}{2}}T_{i-\frac{1}{2}}\right)$, and the temperature of the cell will be cooled. In this way, the algorithm smooths out oscillations in the temperature field.

1.1.5 Overall Solution Procedure

Given the velocity, pressure, temperature, and liquid fraction fields at time t, the solution for the next time step is determined using the following procedure:

1. Update the locally refined mesh based on velocity and temperature fields at time t.

2. Iterate through the following steps (until convergence) in order to advance the discretized equations in time:
    a. Compute convection term using a second-order explicit central differencing scheme.
    b. Complete first fractional step to calculate $\vec{u}^*$, Eq. (7).
    c. Solve pressure Poisson equation to determine pressure and velocity at t + Δt, Eq. (8)-(11).
    d. Compute liquid fraction at t + Δt, Eq. (13).
    e. Solve energy equation to find temperature at t + Δt, Eq. (14).
    f. Check convergence of pressure and velocity fields. This is done by taking the norm of the step change in pressure and velocity fields at the current iteration and comparing this to these same norms for the previous iteration. If the change between iterations for either pressure or velocity is more than a small convergence criterion (i.e. 1.0e-5), the process returns to step 2a.

The above algorithm is applied below to benchmark the calculations and to test the design of a small thermal storage device.

1.2 Benchmarks

1.2.1 Phase Change Benchmark

The melting of gallium is a well-established experimental benchmark for phase-change problems. The geometry for the simulation involves a horizontal rectangular container filled with solid gallium at T_{melt}, the left wall held at a constant temperature above T_{melt}, and the right wall held at T_{melt}. The top and bottom walls are all insulated. Following the experiments of Gau et al. [65], two versions of the experiment were simulated, with

Table 1: Parameters for Gallium Simulations				
Aspect Ratio (H/L)	**.714**	**.5**	**Material Characteristics**	
Prandtl number	.21578	.21578	Conductivity (k)	32.0 W/m*C
Grashof number	2.8096e07	1.0363e07	Specific Heat (C_p)	381.5 J/kg*C
Rayleigh number	6.0626e05	2.236e05	Latent Heat (L_H)	80160 J/kg
Stefan number	.03912	.03912	Density (rho)	6095 kg/m^3
Characteristic time	293.0 s	147.1 s	Kinematic viscosity	2.9696e-07 m^2/s
$T_{wall, cold}$, $T_{wall, hot}$	29.78, 38.3 C	29.78, 38.0	Thermal expansion (B)	1.2e-04 C^{-1}

height/length ratios of .714 and .5, respectively, where length is the distance between the hot and cool walls (see Table 1 for parameters).

The results of the simulations match well with both the experimental results and other numerical simulations [66], and the multicellular streamline patterns match the simulations done by Hannoun [67]. Note that the current data creates a slightly more undulating solid-liquid front than the experimental results (see Figure 4); this has been a common problem with numerical simulations of melting gallium [68]. Wittig has recently argued that two-dimensional simulations of gallium melting overestimate the formation of steady convection cells because they do not account for drag on the horizontal walls [46]. However, the liquid-solid fronts in the current simulations are less undulating than those in Hannoun (see Figure 3), and more importantly the overall position and the shape of the liquid-solid fronts agree well with the experimental results.

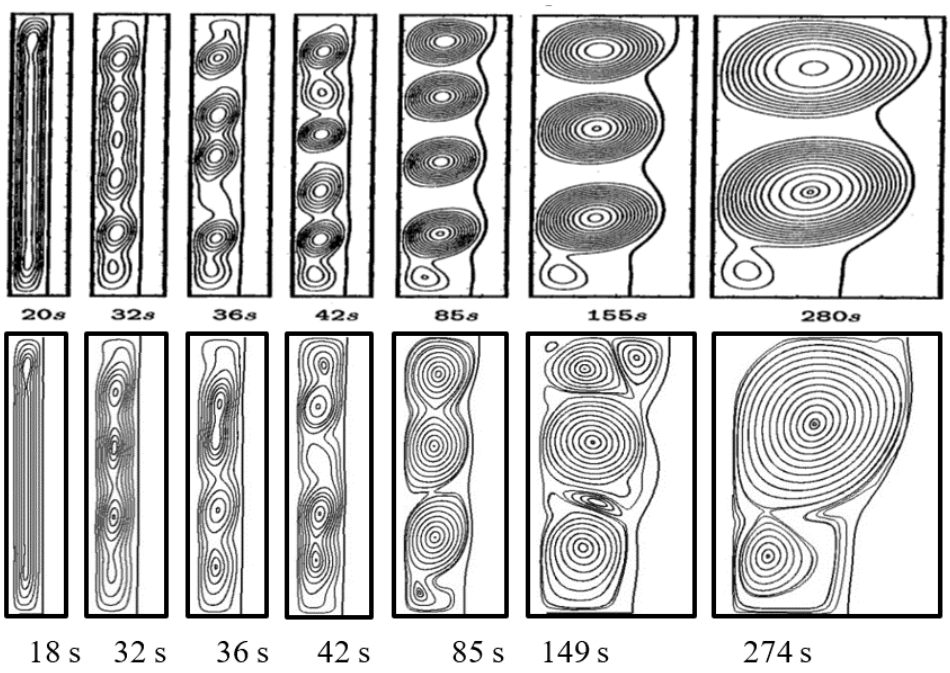

Figure 3. Streamlines during development of 0.5 aspect ratio (H/L) Gallium simulation. Upper images are from Hannoun et al.; lower images are from current data.

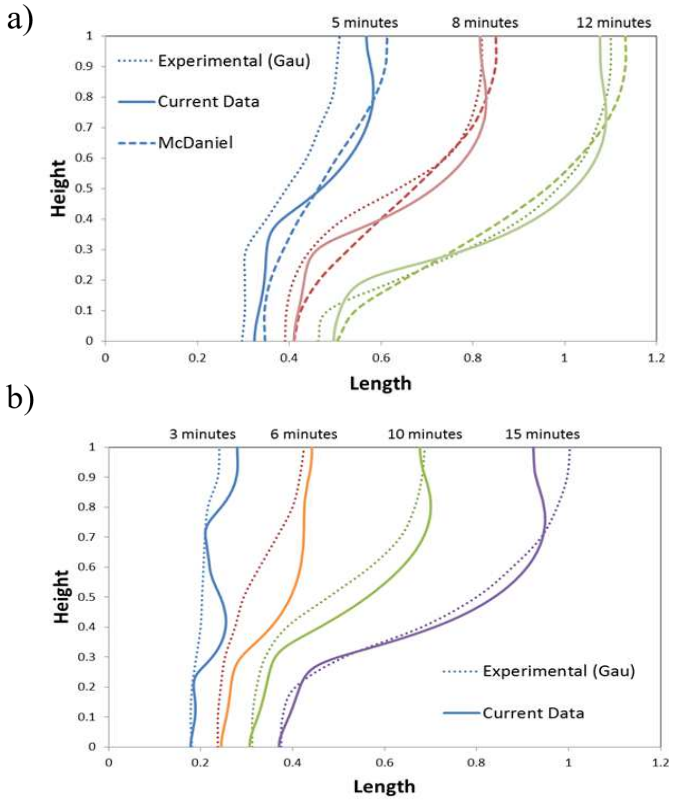

Figure 4. The location of the Gallium melting front (liquid fraction = 0.75) for aspect ratio (H/L) of (a) 0.5 and (b) 0.714.

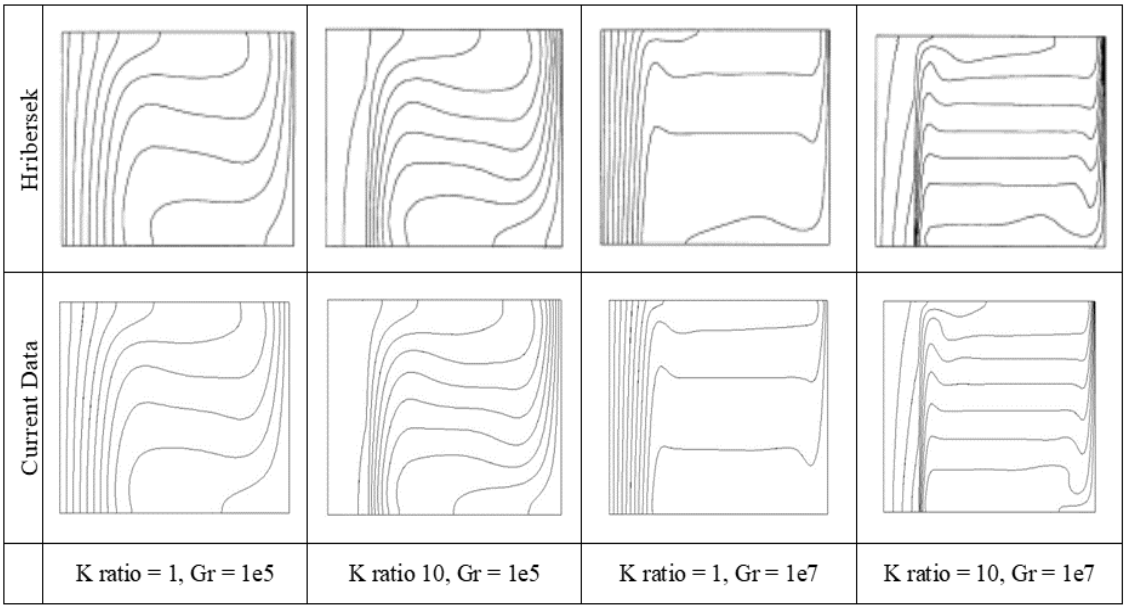

Figure 5. Isotherms at steady-state natural convection for different k ratios and Grashof numbers. The left wall is held at T_{hot}, the right wall is held at $T_{initial}$; the field contains a solid from x=0 to x=.2, and a fluid from x=.2 to x =1.

1.2.2 Conjugate Heat Transfer Benchmark

Conjugate heat transfer results are benchmarked against results obtained by Hribersek [69]. The simulations are conducted for natural convection in a rectangular cavity. As in the previous benchmark simulation, the left wall is heated at a constant T_{hot}, the right wall is held constant at T_{cold}, and the top and bottom walls are insulated. However, in this setup the container has two sections. On the left side, from x=0 to x=.2, is a vertical solid plate. On the right, from x=.2 to x =1, is a liquid at a uniform initial temperature T_{cold}. The conjugate heat transfer must be solved at the solid-liquid interface as the heat moves through the solid into the liquid and creates natural convection in the fluid in the right side of the chamber.

Using the numerical approach detailed above for the conjugate heat transfer, tests were performed for specific heat ratios (k_{solid}/k_{liquid}) of 1 and 10 and Grashof numbers 1.0e5

and 1.0e7 and the results were compared with those of Hribersek. The current calculations agree very closely with the benchmark, both in the isotherms calculated (shown in Figure 5 for a range of specific heat ratios and Grashof numbers) and in the temperatures along the solid-fluid interface (shown in Figure 6).

1.2.3 Combined Phase Change and Conjugate Heat Transfer Benchmark

Having ascertained the accuracy of the phase change and conjugate heat transfer calculations above, the combined effects of phase change and conjugate heat transfer are benchmarked against the simulations of Gharebaghi and Sezai [34]. This is a simulation of the melting of paraffin wax within an aluminum heat sink in the configuration shown in

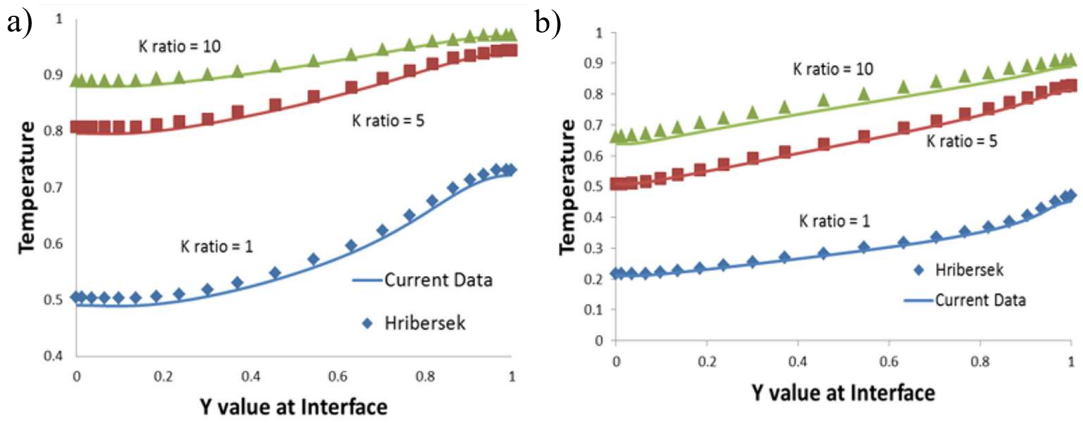

Figure 6. Temperature along the solid interface at steady-state natural convection flow for (a) Grashof = 1e05 and (b) Grashof = 1e07. Left wall at T=1.0 and right wall at T= 0.0.

Figure 7a. It consists of a two dimensional rectangular enclosure with constant temperature on the top and bottom of the enclosure; the two lateral sides have an aluminum plate that is within the computational field, and a no flux boundary applies on the outside boundary of the fin. The heat from the top and bottom moves into the PCM enclosure directly from

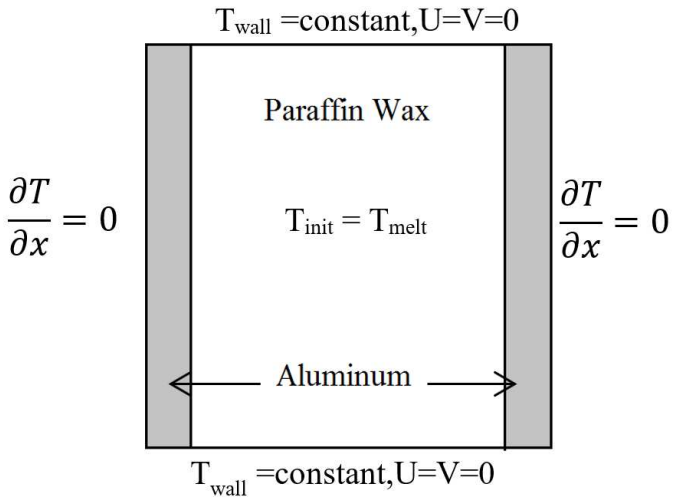

Figure 7. The geometry of the combined conjugate heat transfer and phase change benchmark simulation, where $T_{wall} > T_{init}$.

the top and bottom and through conjugate heat transfer from the aluminum sides. This combination of conjugate heat transfer and convection-dominated melting provides a simplified version of the simulations for the thermal storage device at the center of the present work.

The results from the current simulations agree very well with the benchmarks (Figure 8) with the difference that the current work shows a slower melting process towards the end of the simulations (Figure 8(b)). The source of this difference seems to be the extent of the convection within the chamber in the later stages of the simulation. When the wax is fully melted (f=1.0), the current work shows little temperature fluctuation at the horizontal midplane, while the benchmark simulation indicates a wavy temperature profile (Figure 8(a)). This temperature fluctuation might have been produced by residual convection. This would explain the slower completion of the melting process in the current work: with less convection in the latter stages, the melting of a low conducting material

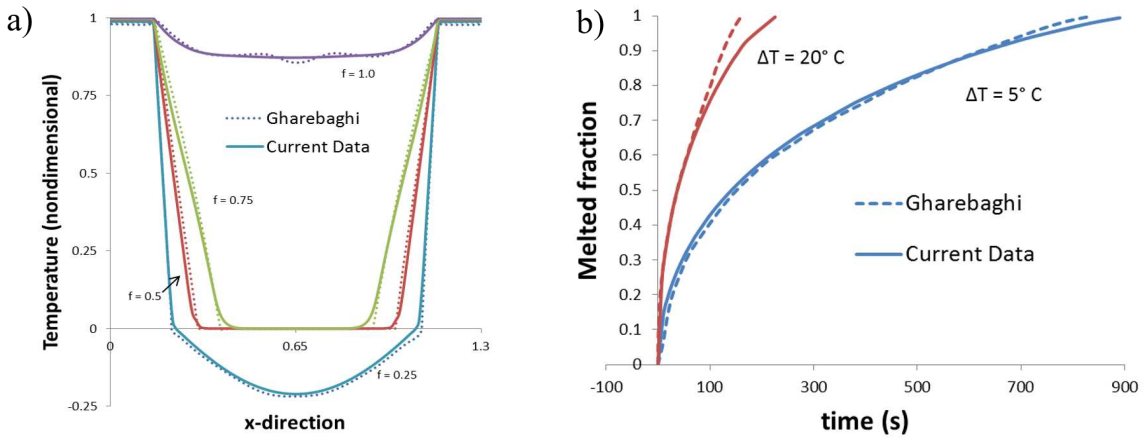

Figure 8. Combined benchmarks. (a) temperature profile at the horizontal midplane of the enclosure at various states of melting ($f = F_{liquid}$). (b) melted fraction over time for two simulations, where $\Delta T = T_{wall} - T_{init.}$

like wax would be slower. This would also explain why the difference between the benchmark and the current work is larger for the larger ΔT simulation (Figure 8(b)), as one would expect convection to be a more significant factor in the simulation with the larger temperature difference. Despite these differences the overall melting behavior for the bulk of the melting process is well captured.

1.3 Thermal Storage Device Tests

The numerical scheme detailed above accurately represents the conjugate heat transfer, melting, and convection patterns typical of a simple PCM-based heat storage process. We turn now to the focus of this project, the melting of solar salts with the aid of a complex finned aluminum core. While the move from the melting of wax or gallium in a rectangular container to the melting of salts in a solar-powered LHTSD might seem a small jump, the change in material, geometry, and boundary conditions creates significant numerical challenges. In particular, the size of the LHTSD, the much higher differences between boundary temperatures and initial temperatures, and the low viscosity and thermal

Table 2: Material Properties and Parameters for LHTSD Test

Solar Salts	
Kinematic viscosity (ν)	3.59e-06 m^2/s
Thermal diffusivity (α)	1.500e-07 m^2/s
Latent heat	145.9 kJ/kg
Prandtl number	23.95
Grashof number	1.712e8
Stefan number	0.797
Melting temperature	221 ^{0} C
Specific heat (C_p)	1550 J/kgK
Density (ρ)	1980 kg/m^3
Thermal conductivity (k)	.460 W/mK
Thermal expansion (β)	.0003748 ^{0} C^{-1}

Aluminum	
Thermal diffusivity (α)	6.65e-05 m^2/s
Specific heat (C_p)	893 J/kgK
Density (ρ)	2730 kg/m^3
Thermal conductivity (k)	162 W/mK

Simulation Parameters	
Initial temperature (T_{init})	213.5 ^{0} C
Wall temperature (T_{hot})	288.5 ^{0} C
Characteristic length (L)	.2 m
Characteristic time (t_o)	.8516 s
Characteristic vel. (u_o)	.2346 m/s
Mushy region	213.5-228.5 ^{0} C

conductivity of the melted salts lead to Grashof numbers on the order of 10^8 and Rayleigh numbers well above 10^9. The complexity and asymmetry of the finned structure and long time-scales further complicate the simulations. A chief contribution of this work is to demonstrate the practicality and usefulness of these more difficult simulations in a design and optimization process.

As explained in the introduction, the purpose of the unit considered for study is to store solar energy for a household-use solar cooker [70], although the general techniques apply to larger scale LHTSDs as well. In such solar cooker designs, solar energy is focused on one side of the LHTSD using a lens or curved mirror. The solar heat melts the PCM over the course of the day, and as the PCM resolidifies, the LHTSD remains at a constant temperature (the temperature of transformation of the PCM). In this project, the PCM of choice is solar salt, which is a blend of sodium nitrate and potassium nitrate [23, 71]. The

melting point of the salts, about 221 degrees C, is ideal: it is low enough that solar cookers should be able to reach the heat, but it is high enough that cooking would be possible during the release of the latent heat [72]. The problem with solar salts, however (as with most PCMs), is its low heat conductivity: it is difficult to work the solar heat into the storage device beyond the surface of the material. To address this problem, a highly conductive finned core is added to the container. This core, here made of aluminum, helps move the thermal energy into the bulk of the PCM during the heating process and also helps to create an even heat on the surface of the LHTSD during the cooking process.

To demonstrate the potential of the described method in evaluating different LHTSD designs, two potential designs for the fin structure of small-scale solar-powered LHTSD are tested to assess whether the thermal storage efficacy of a particular design can be enhanced. The complex geometry of this finned core makes it difficult to optimize a design through intuition or experimentation. Two design tests are presented here. Both batteries have an equal overall volume as well as an equal volume of PCM and aluminum; they have an equal number of similarly sized fins, and the fins are equally spaced. The key difference is the shape of the core. In the first design, the core is a straight cylinder that goes through the center of the fins. In the second design, the core is slanted downward to take advantage of the convection-dominated heat transfer (see Figure 9).

The initial and boundary conditions and the material property parameters for both simulations are the same (see Table 1 for parameters). The initial temperature of the aluminum and salts is set at 213.5 C, which is the lower bound of the phase change temperature region for the salts. The left hand border of the aluminum core is held constant at 288.5 C, to simulate the focused solar energy at the top of the core. The 2ε value, representing the range of temperatures at which a cell's liquid fraction is between 0 and 1, is 15 degrees. The chief measures of effectiveness are the ability of LHTSD to draw heat into the device and its success in melting the salt quickly and evenly.

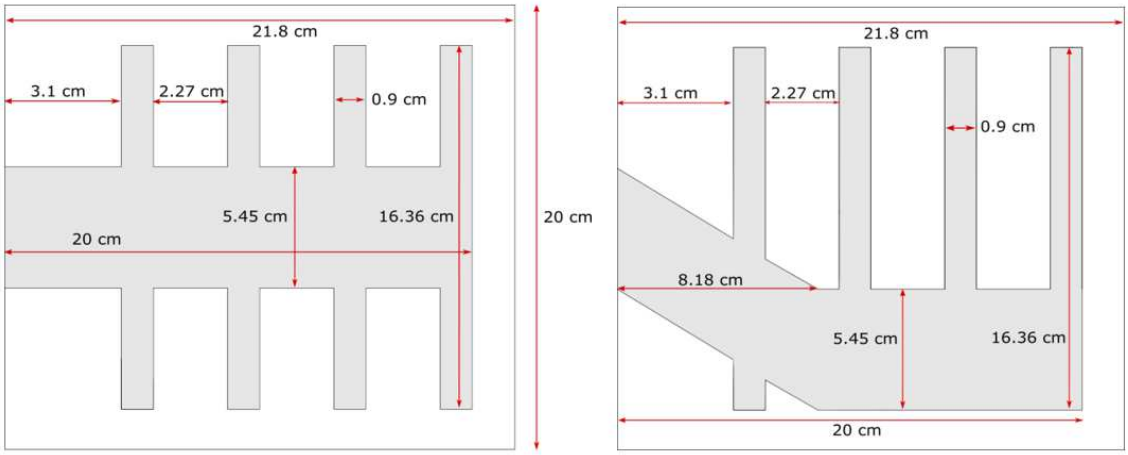

Figure 9. The geometry of the straight and slanted LHTSD designs, respectively.

The first finned structure was chosen for its simplicity: it would be relatively easy to produce, which is an important factor for a product designed for developing countries. However, since heat transfer in such situations is dominated by convection, difficulty efficiently melting the lower part of the PCM was anticipated. The second design was an attempt to use design intuition to modify the fin structure. The results below demonstrate the facility of the Cartesian grid approach to change the fin geometry without changing the computation mesh; it also demonstrates that relying on intuition to modify fin design in a LHTSD may not lead to anticipated results and therefore a more sophisticated optimization strategy will be necessary.

The temperature, liquid fraction, and velocity magnitude fields for the simulation of this first design are shown in Figure 10. The heat from left wall moves quickly into the aluminum, but the field within the aluminum core changes very little after this initial phase. The behavior of the salts above and below the aluminum core is significantly different. The heat transfer in the bottom of the structure is dominated by conduction, which results in small velocity magnitudes and a slow moving solid-liquid front that remains relatively horizontal throughout the simulation. The heat transfer above the aluminum, however, is

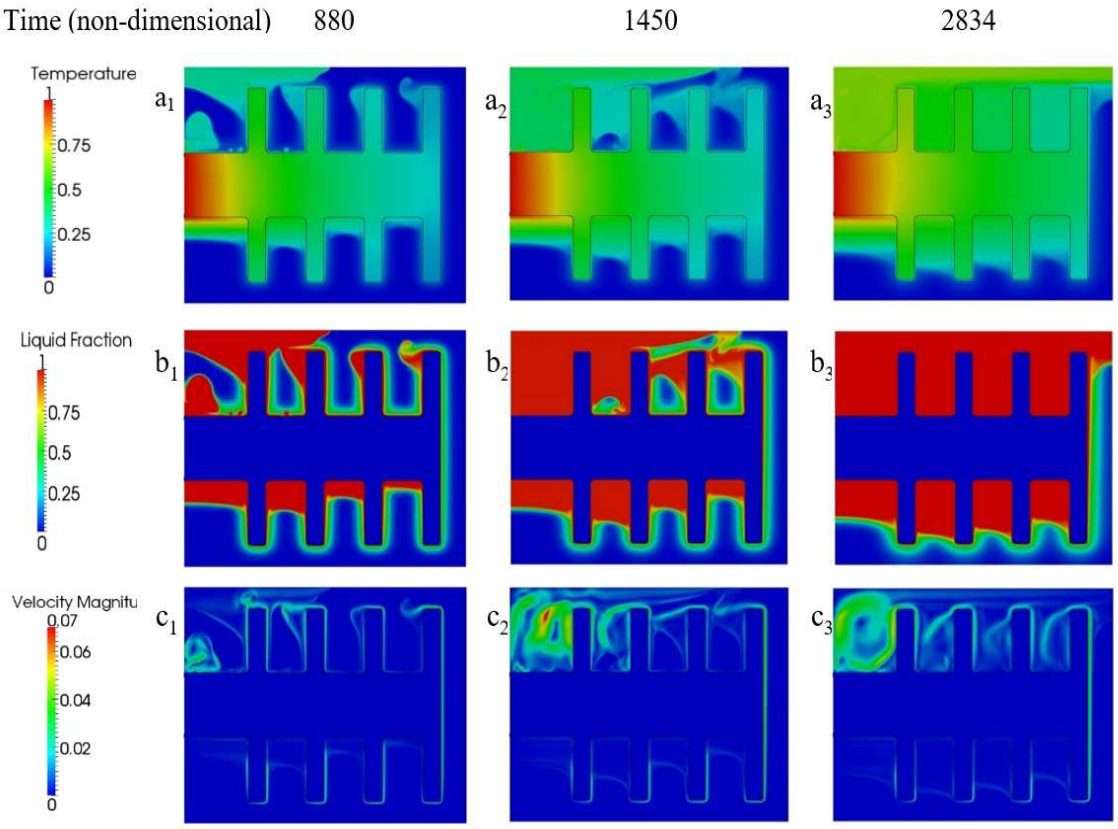

Figure 10. Temperature, Fliquid, and velocity magnitude fields for the straight fin design LHTSD at three time steps.

dominated by convection: the velocity magnitudes are much higher here, and irregular melting front is formed by plumes of moving molten salt.

At $\tau = 880$, the amount of melted salt above and below the aluminum is similar (see Figure $10b_1$). Up to this point, the effectiveness of conduction and convection are not markedly different. However, by $\tau = 1450$, the convection process above the core has led to a much higher fraction of melted salts (Figure $10b_2$), and by the time the PCM is largely melted, there are still significant unmelted portions in the bottom of the LHTSD (Figure $10b_3$).

The persistence of an unmelted layer of salts at the bottom of the cavity led directly to the second design. The slanted aluminum core was designed to encourage a stronger transfer of heat into the bottom half of the LHTSD and open up more space for the convective heat transfer that dominated the second two thirds of the simulation. However, while the redesigned slanted finned structure was significantly more effective at drawing heat into the center of the LHTSD, it turned out to be less effective in melting the salts in an even and efficient manner (see Figure 11). To see why this is, it is helpful to divide the heating process for both LHTSDs into four phases.

First, in both simulations there was an initial period of steep increase in mean

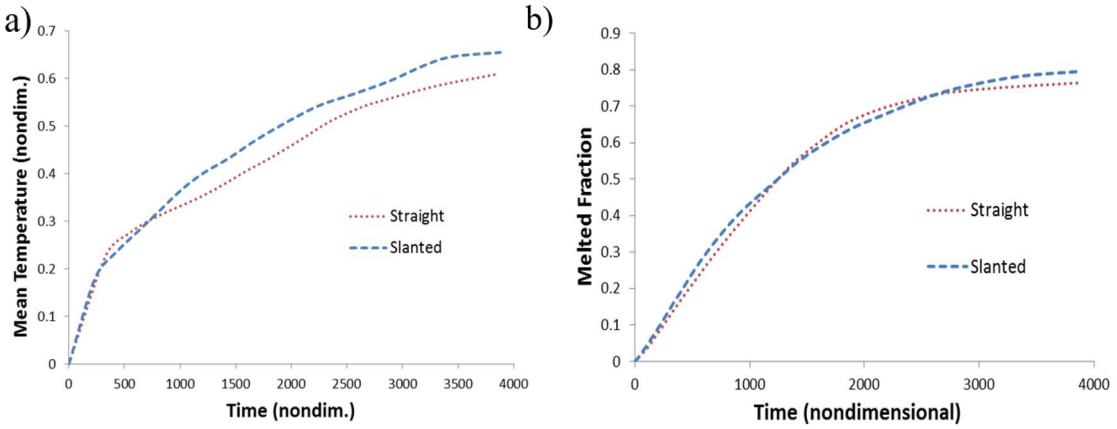

Figure 11. The (a) mean temperature and (b) melted fraction of the two LHTSDs

temperature due to the relative initial lower temperature of the solar salts (see Figure 11): this period, which lasts approximately until $\tau = 250$, is dominated by conduction. Because there is no fluid movement and both designs have the same solid characteristics, it is not surprising that their behavior is very similar. There is one small difference between the two simulations in this phase: it lasts slightly longer in the straight finned structure, likely because of the increased diffusion in the negative y-direction (Figure $10a_1$ and Figure $12a_1$).

Because of this difference, the mean temperature in the straight finned structure simulation initially reaches slightly higher values.

In the next phase, however, the slanted LHTSD demonstrates the main advantage of its design. Between approximately $\tau = 300$ and $\tau = 1000$, due to the greater overall natural convection, the slanted design pulls heat into the unit much more effectively (Figure 11). This is evident in the slope of the mean temperature line, which is higher during this period for the slanted design compared to the straight fin design. Figure $10c_1$ and Figure $12c_1$ show that the velocity magnitudes in the slanted simulation are considerably higher. Because of this increased convection-induced movement, the fluid salts are moving quickly over the hot core of the slanted design, and this leads to higher melted fraction for the slanted design around the $\tau = 880$ mark (see Figure $10b_1$ and Figure $12b_1$, as well as in the graph of melted fraction in Figure 11).

However, in the third phase (from $\tau = 1000$ to $\tau = 2500$), the slanted LHTSD falls behind the straight design in terms of melting the salts. Figure $10a_2$ and Figure $12a_2$ show that the salts in the upper left corner of the slanted simulation are considerably warmer than those in the straight simulation. So the mean temperature remains higher in the slanted design (Figure 11a), but this heat gain is not spread as evenly as it is in the first simulation: the straight design does a better job of heating its aluminum core and bringing heat into the center of LHTSD. Furthermore, since the upper left corner is fully melted in this phase, the convection advantages of the slanted design disappear. This change in the convective characteristics can also be seen in Figure $10c_2$ and Figure $12c_2$, which show that the maximum velocity magnitudes for the two simulations are very similar during this period. Finally, Figure 11a demonstrates that the slopes of the mean temperature increases are also very similar: because of the changes in convective behavior, the slanted design is no longer pulling in more heat than the straight design.

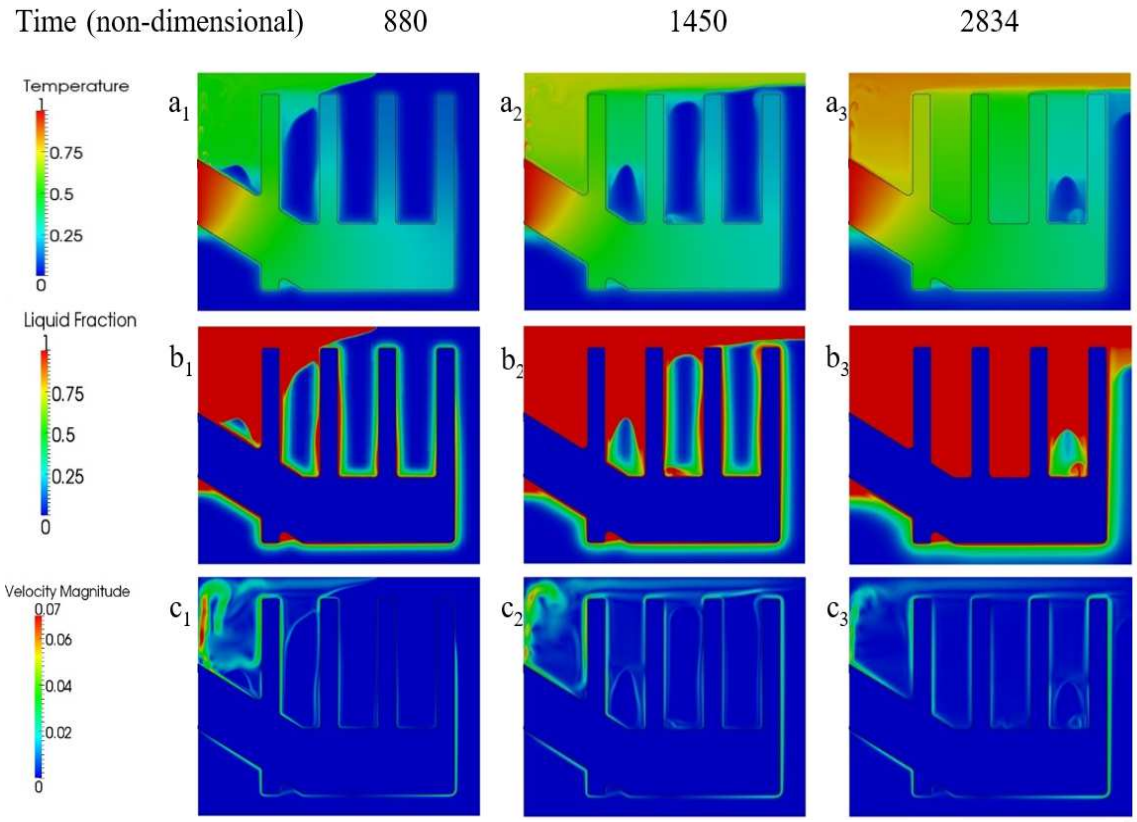

Figure 12. Temperature, F_{liquid}, and velocity magnitude fields for the slanted fin design LHTSD at three time steps.

In the last phase of the simulations (from $\tau = 2500$ to $\tau = 4000$), the slanted design pulls slightly ahead in the amount of melted salt. This is because it is able to more fully melt the bottom section of the PCM (Figure $10b_3$ and Figure $12b_3$), and as the melting process wanes, the slanted finned structure is able to finish the melting on the upper half that had already been completed by the straight design. The melting process for both designs levels off well before 100% of the material is melted, but the final level of the slanted design is higher than that of straight fin design.

In summary, the second design does achieve one of its goals, which was to melt more of the salts in the lower half of the LHTSD. However, its weaknesses point to further directions for testing and optimization. Clearly, the larger heat flux for the slanted design

in the second phase demonstrates that convection is crucial to moving heat quickly into the salts. But the early onset of convection must be able to reach a large volume of the low conductivity salts: the advantages of the second design were lost at later times because of the small confined volume in the upper left corner of the LHTSD. Finally, the aluminum fins must have some way to reach the bottom of the battery: even in the second design, the salts in the bottom of these test simulations are not melted even in the very late stages. Further optimization of the fin design must seek to address these deficiencies of the slanted fin design.

1.4 Conclusion

The initial testing of these two simplified designs demonstrates the ability of this numerical approach to simulate the melting of solar salts in a complex geometry. Furthermore, the results show the potential of the approach to evaluate the effectiveness of different fin designs. Its chief advantages is that it allows efficient optimization studies of phase change in complex geometries without the requirement of complicated grid generation and maintenance, while retaining the accuracy of finely-meshed simulations by recourse to local adaptive meshes that resolve interfaces.

The remainder of the thesis develops the potential of this process for LHTSD optimization in several different directions. First, the work investigates the possibility and utility of a more realistic simulations of the charging and discharging of solar-powered LHTSD: these simulations incorporate dynamic boundary conditions that imitate the diurnal solar pattern and compute results for a full two-day (48 hour) period. Second, a set of three dimensional simulations of a small-scale LHTSD are compared to experimental results in order to better describe and understand the development of the heat transfer processes within the solar salts. Finally, the numerical approach is combined with a

dynamic Kriging metamodel optimization process to optimize the design of a bottom-heated cylindrical LHTSD with a horizontal fin structure.

CHAPTER TWO
DIURNAL SIMULATION OF SOLAR COOKER

In this chapter, the effect of combining metal fins (Al) for heat spreading and recovery with phase change material (a mixture of $NaNO_3$ and KNO_3) on the performance of a thermal storage device over a 48-hour period is investigated. High-resolution transient simulations are performed covering two days of solar energy influx and heat extraction. The energy inputs of the simulations are based average solar radiation during a 48 hour solar cycle in New Delhi, India in June with a 1.5 m^2 solar reflector. Four different fin designs for an insulated LHTSD to be used with a solar cooker are tested. The four designs are compared based on their ability to spread heat evenly and rapidly into the PCM and the ease with which heat can be withdrawn from the device for cooking. The tests demonstrate the potential for using long term, multiday numerical simulations in the evaluation of LHTSD designs.

The chief challenge in performing these tests is the vastly different time and length scales inherent in a simulation of a LHTSD. On one hand, the real time scales for the solar cookers are very long: at the very least, it is necessary to simulate the hours between sunrise and sunset. In order to simulate thermal storage, at minimum a twenty-four hour simulation is needed. Second, a LHTSD designed to cook two meals and hold its heat overnight must be large: the LHTSD simulated here contains over a 30 cm tall. These large time and length scales are in contrast to the small scales of the flow: the complex fin geometries, high temperature gradients, and strong convection patterns necessitate small time steps and a fine computational mesh.

Simulations combining these different time and length scales requires significant parallel computer resources and a robust simulation code. As a result, no studies have thus far demonstrated the possibilities of such long-term tests for the optimization of LHTSD

design. The contribution of the current work is to perform a series of realistic full scale two-dimensional simulations of latent heat solar cooker designs. Four separate fin designs, each with the same mass of fin material and PCM but with different internal configurations, are simulated over 48 hour periods. The fin material used is aluminum, and the PCM is so-called "solar salts," a near-eutectic mixture (60/40% by mass) of $NaNO_3$ and KNO_3 commonly used in thermal storage applications [23, 71]. The designs are compared on their ability to spread heat quickly through the LHTSD, to melt the PCM evenly, and to allow the efficient and rapid withdrawal of energy for cooking. These comparisons demonstrate the potential for optimization of latent heat thermal storage devices using long-term numerical simulations.

2.1 Numerical Methods

The numerical scheme used in these simulations is explicated in detail in the first chapter. The chief change from the governing equations used in the first chapter is that the equations used here are dimensional. The incompressible Navier-Stokes equations are solved using the Boussinesq approximation and an enthalpy-porosity formulation. The mass balance equation is:

$$\frac{\partial u}{\partial x} + \frac{\partial v}{\partial y} = 0 \tag{25}$$

where u and v are the (dimensional) velocities. The momentum balance equations are:

$$\frac{\partial u}{\partial t} + u\frac{\partial u}{\partial x} + v\frac{\partial u}{\partial y} = -\frac{1}{\rho}\frac{\partial p}{\partial x} + \nu\left(\frac{\partial^2 u}{\partial x^2} + \frac{\partial^2 u}{\partial y^2}\right) + Au \tag{26}$$

$$\frac{\partial v}{\partial t} + u\frac{\partial v}{\partial x} + v\frac{\partial v}{\partial y} = -\frac{1}{\rho}\frac{\partial p}{\partial y} + \nu\left(\frac{\partial^2 v}{\partial x^2} + \frac{\partial^2 v}{\partial y^2}\right) + Av + g\beta(T - T_{melt}) \tag{27}$$

In the above, ν is the kinematic viscosity, ρ is the density, T is the temperature, T_{melt} is the melting temperature of the PCM, and β is the coefficient of thermal expansion. The value

of A, the permeability term (with units of length), is defined using a Carmen-Kozeny term, which both matches the physical behavior of a porous medium and eases numerical problems at the melting boundary [52]:

$$A = \frac{C\left(1 - F_{liquid}\right)^2}{\left(F_{liquid}^3\right) + B} \tag{28}$$

F_{liquid} is the liquid fraction, and C (units of length) and B (unitless) are constants chosen to allow small velocities in partly frozen cells but to suppress velocity in solid cells. This allows for the relaxation of the velocity from the solid into the melt and alleviates stiffness. Here $C=10^3$ m and B= .001.

The energy balance equation is:

$$\frac{\partial T}{\partial t} + u\frac{\partial T}{\partial x} + v\frac{\partial T}{\partial y} = \alpha\left(\frac{\partial^2 T}{\partial x^2} + \frac{\partial^2 T}{\partial y^2}\right) + L_{heat}\left(\frac{\partial F_{liquid}}{\partial t}\right) \tag{29}$$

In this equation, α is the thermal diffusivity, defined as $\frac{k}{\rho C_p}$, where k is the thermal conductivity and C_p is the heat capacity. L_{heat} is the latent heat of melting.

The discretization scheme used in this chapter is identical to that used in the first chapter.

2.2 Simulation Setup

The basic operation of the simulated cooker is straightforward. The thermal storage device is a cylindrical container filled with a PCM (solar salts) and a finned metal (Al) core. During the daytime, the cylinder rests on its side. In this position, the exposed circular top of the aluminum core, labeled "Heat Inlet/Outlet" in Figure 13, is a horizontal surface. In order to charge the LHTSD, a large concentrating mirror (such as a Scheffler reflector [73]) focuses solar radiation on the inlet—that is, on the top of the aluminum core. The aluminum core heats up, thus pulling energy into the device. Over the course of a day, the influx of solar energy melts the PCM and raises the temperature of the salts over the melting

point. In the evening, the process is reversed. The cylinder is set upright, so that the aluminum heat inlet now serves as the outlet of heat for cooking: it becomes a "burner" which cooks at the temperature of the aluminum core. As energy leaves the LHTSD through this burner, the PCM begins to solidify. As it does, the PCM remains at a relatively constant solidification temperature for a long period of time, keeping the aluminum outlet at a stable temperature near the melting point of the solar salts (approximately 221 °C). In the morning, if sufficient heat remains in the LHTSD, the device can be used to cook a second time. As the sun climbs higher, the heat collection process begins again, and the procedure is repeated.

A number of characteristics define an efficient LHTSD. First, the device must store the heat supplied during one day of charging at a reasonable temperature. For cooking purposes the temperature desired is in the range of 200-300 °C. Too high a storage temperature will not be beneficial; it will also lead to high losses of heat during storage. Second, heat must be spread rapidly in the device to prevent hot spots. This applies both during heat input as well as heat extraction for cooking. Since heat will be supplied over a period of several hours but will be withdrawn in two one-hour sessions, the stricter demand is during heat withdrawal. If the PCM is molten during withdrawal natural convection can assist in conveying heat to the Aluminum heat spreaders and thereby to the receiver plate. Therefore it is desirable to maintain the PCM in the molten state as far as possible during the heat recovery phase. One measure used to determine the ability of a particular design to minimize hot spots is the temperature standard deviation. At any given moment, the standard deviation of the temperature for a material *j* is defined as:

$$\sigma_T^j = \left(\frac{\sum_{i=1}^{n} \left(\left(T_i - T_{ave}^j \right)^2 * area_i \right)}{area_{total}^j} \right)^{\frac{1}{2}} \tag{30}$$

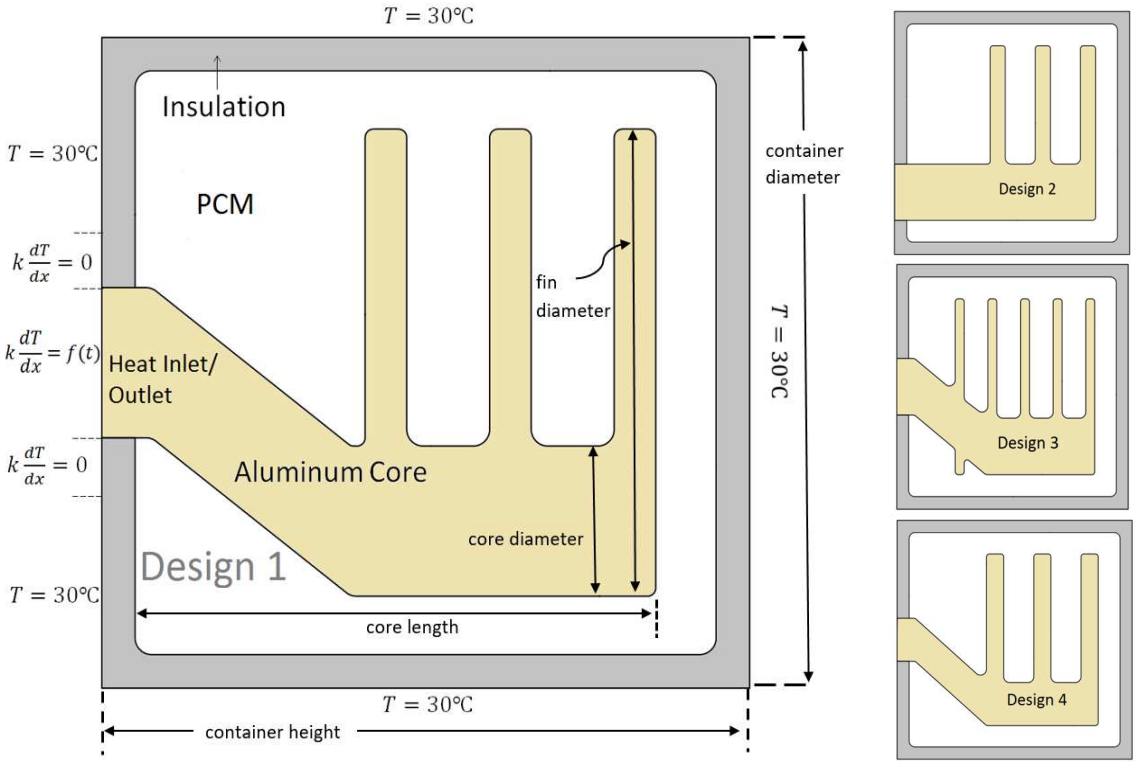

Figure 13. The four tested designs. The boundary area with no flux extends 0.02 m on each side of the exposed aluminum core. Exact measurements are given in Table 3.

where i represents a cell within the simulation domain of material j, $area_i$ is the area of the cell i, and $area^j_{total}$ is the total area for material j. T^j_{ave} is the average temperature of that material, defined as

$$T^j_{ave} = \frac{\sum_{i=1}^{n}(T_i * area_i)}{area^j_{total}} \quad (31)$$

A low standard deviation during the outflux stage, particularly within the aluminum, indicates that a LHTSD is efficiently pulling heat from the salts through the outlet plate. Finally, a good design will store the bulk of its energy as latent heat. If the heat can be stored mostly in latent form, the temperature at which heat is withdrawn (i.e. the cooking temperature) will be nearly constant; cooking as the temperature is falling with time would be difficult. However PCMs generally have very low thermal conductivity; therefore heat

spreading, particularly when the PCM is in the solid state requires a suitable amount of metal in the device.

The key variable determining the effectiveness of a LHTSD design is the geometry of the finned Al core. In the present study, four designs for the aluminum finned core were tested. The designs were chosen to test the effects of three design parameters on the thermal storage and recovery characteristics of the device: the shape and location of the core within the LHTSD, the number of fins, and relative thickness of the fins and core. The four designs are shown in Figure 13. Design 1 is the standard design. Since earlier work confirmed that a chief difficulty in the melting process was moving the heat into the bottom part of the LHTSD, the core of each of the four designs is directed through the bottom of the container. One parameter is changed for each of the other designs. Design 2 offsets the inlet to the device to further assure melting in the bottom of the container. Design 3 has five fins rather than three; because of this, the spacing between the fins is different, and the first fin is placed closer to the inlet/outlet than the first fins in the other designs (this means that the first fin is actually on the slanted part of the core, as shown in Figure 13). Design 4 has thicker fins; as a result, because the amount of salt and aluminum in the LHTSD is kept equal for all four designs, design 4 also has a more slender core.

Table 3: Shared Design Characteristics

Container Characteristics (without insulation)		**Material Characteristics**	
Height	0.35 m	Solar salt (volume)	0.02754 m^3
Diameter	0.35 m	Solar salt (mass)	53.70 kg
Volume	0.03367 m^3	Aluminum (mass)	16.75 kg
Insulation Thickness	0.1 m	Aluminum % (by volume)	18.2%
		Salt % (by volume)	81.8%

The images in Figure 13 illustrate an important limitation of the current work: the fact that these simulations must be run in a two-dimensional space. On the one hand, computational limitations make it impossible to consider the use of a three dimensional simulation, given the size of the container, the characteristics of the melted salts, the high temperature gradients within the simulations, and the length of these simulations. Even in two dimensions, these simulations were run on 256 processors and still required up to 4 weeks to run. Clearly, three dimensional versions of the simulations are out of the question. On the other hand, these geometries cannot be exactly represented in two dimensions, because they are not axisymmetric, particularly with respect to the gravitational vector. As a result, the geometries shown in Figure 13 are two dimensional approximations of the geometries, sliced with a vertical plane that coincides with the axis of the cylindrical containers. As a result, the simulations provide only a limited sense of the behavior of the melted salts within these designs. However, the advantages of the long term simulations make this an acceptable limitation for two reasons. First, only by accepting this limitation is it possible to observe the development of heat and fluid flows over the course of full

Table 4: Design Parameters

Parameter	**Design 1**	**Design 2**	**Design 3**	**Design 4**
Core diameter (m)	0.09	0.09	0.09	0.07
Core length (m)	0.3136	0.3136	0.3136	0.3136
Core volume (m^3)	0.001995	0.001995	0.001995	0.001207
Fin diameter (m)	0.28	0.28	0.28	0.28
Fin thickness (m)	0.025	0.025	0.015	0.0284
Number of fins	3	3	5	3
Fin volume (m^3)	0.004141	0.004141	0.004141	0.004918
Al. surface area (m^2)	0.4775	0.4682	0.6984	0.4804

diurnal cycles. Second, the behavior of the salts in the four simulations ably demonstrates the different types of flows that develop in response to the given design choices, even if the smaller details of the flows might be different in a three dimensional simulation.

While the fin and core design varied for each of the tests, the other material characteristics of the LHTSD and the overall size of the container are identical (see Table 3). This includes the size of the container, its shape, the diameter of the fins, and the amounts of salt and aluminum. The size of the device was determined by considering the energy necessary to cook two full meals for a family of four, estimated at 6120 kJ [74]. In order that this energy be available at constant heat at T_{melt}, it is important that most of this energy be stored latently. Storing this amount of latent heat in solar salts requires 41.95 kg of salt, which fills .0215 m^3 (since not all of that energy is available for retrieval at a high temperature, the designs here hold over 50 kg of solar salts). Furthermore, the

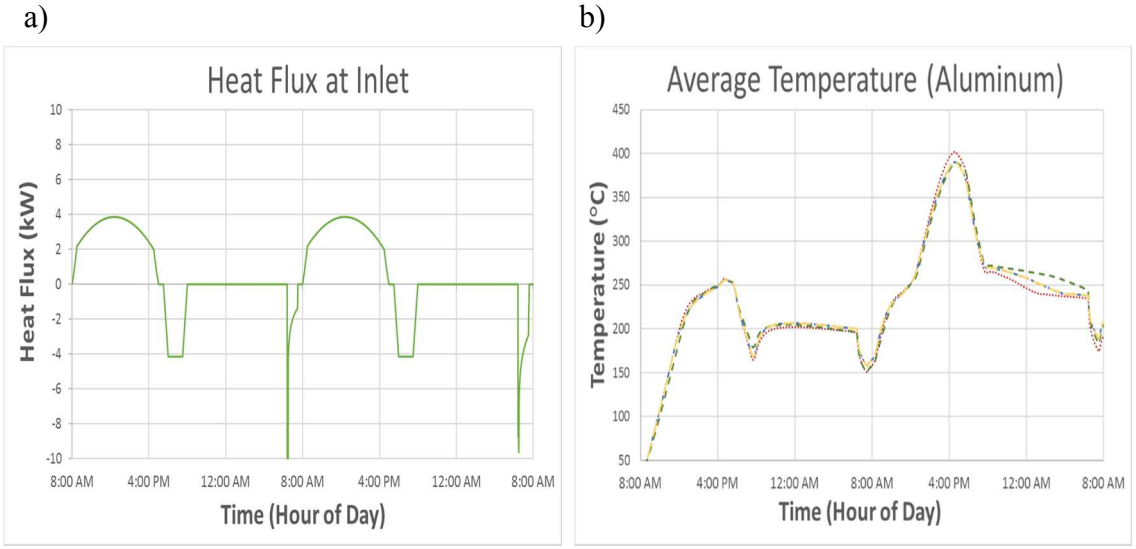

Figure 14. (a) The evening outflux (5:30-8:00 PM) is a Neumann BC equivalent to -850 kW. The morning outflux (6:30-7:40 AM) is a Dirichlet condition (130 °C), and so the precise outflux varies depending on the simulation. The flux pattern is the same for both days. (b) Average aluminum temperature over full 2 days. Notice that the starting temperature for the second day is much higher than that for the first day.

majority of the volume of LHTSD should be salt, since the salt can store energy more efficiently than the aluminum and can maintain a constant temperature: in this case, the salt percentage by volume was set at 81.8% for each of the designs. Solar salts were chosen as the PCM because they are readily available, inexpensive, and because the melting point of the salts, about 221 °C, is ideal: it is low enough that solar cookers should be able to reach the heat, but it is high enough that cooking would be possible during the release of the latent heat [72]. Aluminum is chosen because of its low cost, high thermal conductivity and heat capacity, and relatively low density. Please note that the container characteristics in Table 3 refer to the cylindrical shape of the container; therefore the height listed is the left-to-right distance in the illustrations in Figure 13, while the diameter is the top-to-bottom measurement.

In addition, the device in each simulation is surrounded by 0.1 m of insulation made of ground rice husks (an inexpensive and abundant material in developing countries like India) that has impressive insulating qualities [75, 76]. To avoid unnecessary computational expense, the insulation in the simulations is only 0.02 m thick, and the

Table 5: Material Properties and Parameters

Solar salts	
Kinematic viscosity (ν)	3.59×10^{-6} m^2/s
Thermal diffusivity (α)	1.50×10^{-7} m^2/s
Latent heat	145.9 kJ/kg
Melting temperature	231 °C
Melt range (ε)	+/- 10 °C
Specific heat (C_p)	1550 J/(kg K)
Density (ρ)	1950 kg/m^3
Thermal conductivity (k)	0.460 W/(m K)
Thermal expansion (β)	0.0003748 °C^{-1}

Aluminum	
Thermal diffusivity (α)	6.65×10^{-5} m^2/s
Specific heat (C_p)	893 J/(kg K)
Density (ρ)	2730 kg/m^3
Thermal conductivity (k)	162 W/(m K)

Ground Rice Husks	
Thermal diffusivity (α)	2.51×10^{-7} m^2/s
Specific heat (C_p)	1686.2 J/(kg K)
Density (ρ)	123.6 kg/m^3
Thermal conductivity (k)	0.0523 W/(m K)

thermal diffusivity and conductivity of the material were multiplied fivefold. The Dirichlet temperature boundary conditions were set outside the insulation at the ambient air temperature (30 °C) in order to simulate heat loss through the sides of the container. The temperature field in the insulation was solved in the same manner as that inside the aluminum solid. The final details of the container are available in Table 3.

The flux of energy into the core was based on the use of a 1.5 m^2 mirror in June in the location corresponding to New Delhi, India [77]. A 30% energy loss was assumed. This number takes into account loss through light scatter, wind-based convection, radiative losses from the LHTSD surface, and flaws in the focusing mirror. While the assumed 30%

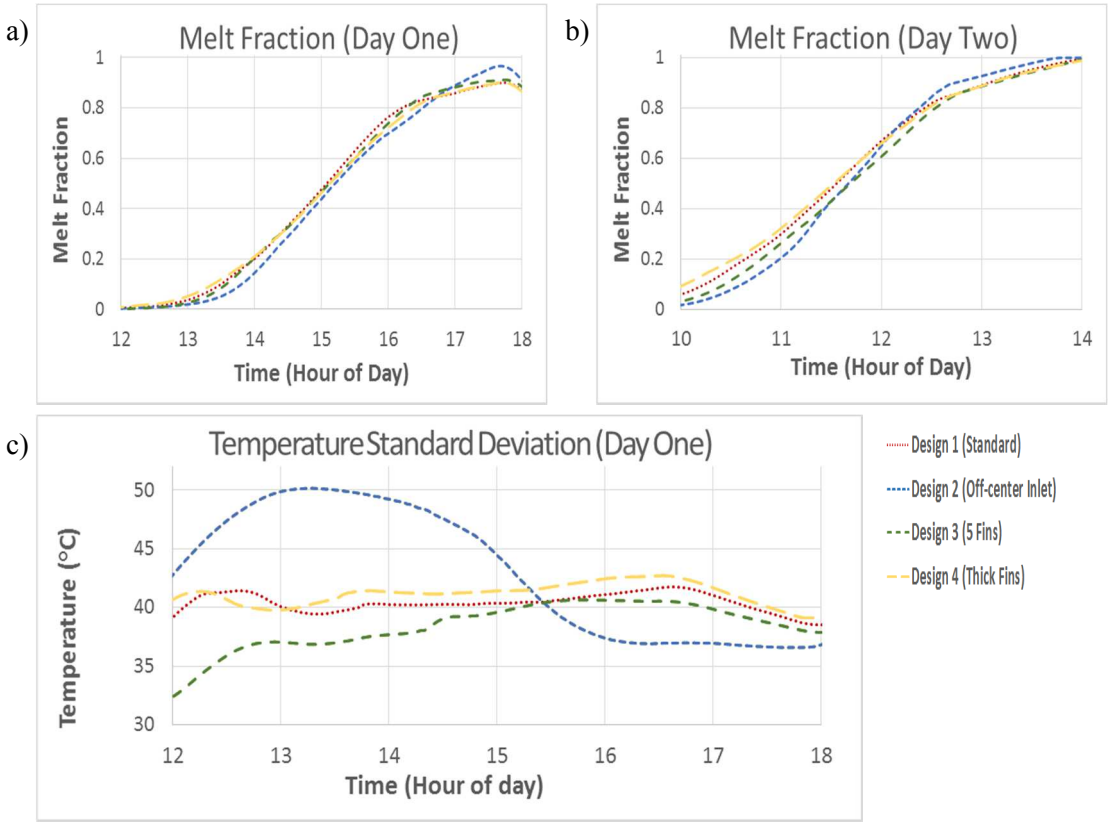

Figure 15. Change of melt fraction during charging process on day one (a) and day two (b). On both days, design 2 lags behind the other three designs in melt fraction. (c) Standard deviation (σ_T) within device during charging on the first day. Design 2 fails to spread its energy as quickly through the device as the other designs.

loss is somewhat arbitrary, it balances two key factors. On the one hand, experimental evaluations of solar cookers have found losses as high as 80% when including thermal loss [78]; on the other, since thermal losses are accounted for in the simulation as loss through the insulation, it would be expected that the unaccounted for losses would be considerably smaller than total loss estimations. The pattern of influxes is identical for both days.

The flux of heat out of the LHTSD for cooking was simulated in two different ways. In the evening, a Neumann (heat flux) boundary condition was set at the location of the

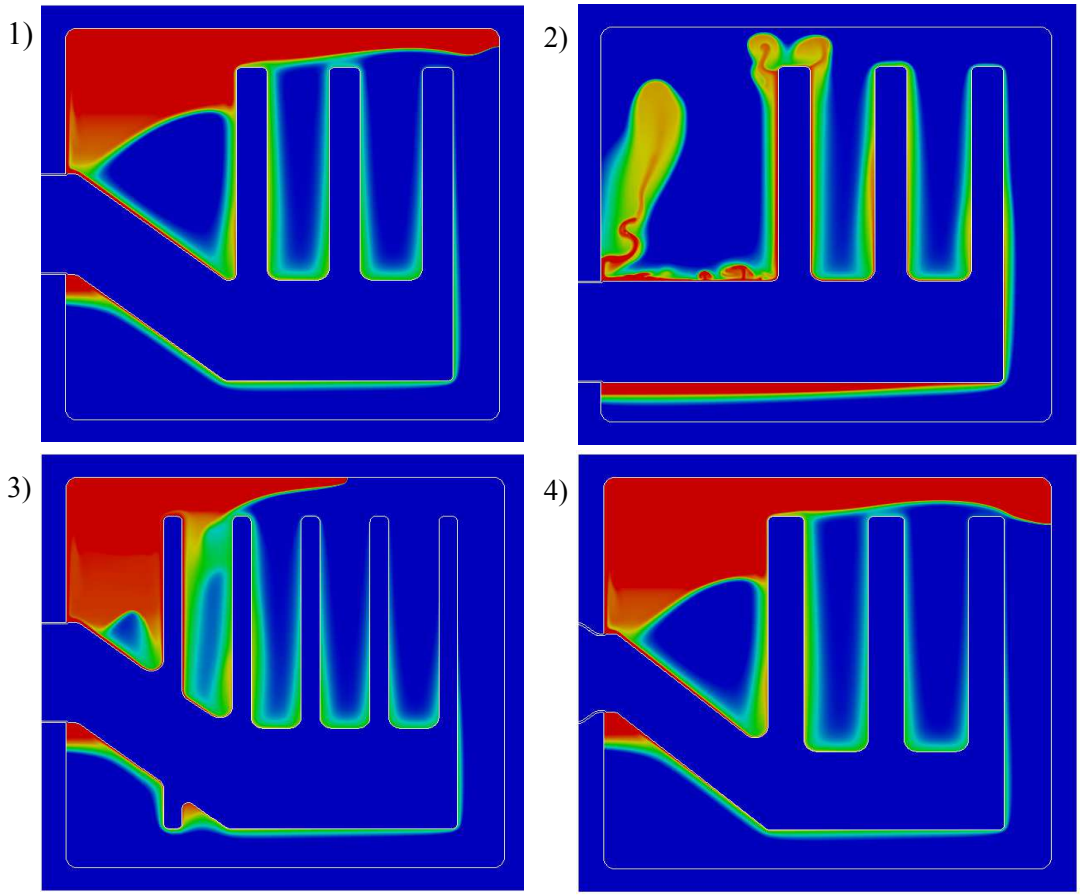

Figure 16. Liquid fraction of designs 1-4 early in second day of heating (11:00). Designs 1 and 3 are nearly identical: a strong convection current carries energy up the side and across the top of the device. Design 3 shows this same pattern, but the first fin is hot enough to create a significant flow. Design 2 is the outlier: the lack of a slanted surface means it is slower to create strong convection currents.

receiver plate, which is the exposed surface of the Al core, to simulate the energy needed to cook a meal. In order to produce 6120 kJ over the course of two hours, an average flux of 850 W was set over two hours. In the morning, it was assumed that the LHTSD would be used to boil water for an hour and ten minutes. Assuming that the bottom internal surface of the pot would have a constant temperature of about 100 °C, and estimating that the temperature difference between the exposed receiver plate and that bottom surface would be 30 °C, a Dirichlet boundary condition of 130 °C was set for that 70 minutes. The 24 hour pattern of fluxes, in both supply and withdrawal modes, can be seen in Figure 14.

2.3 Results

2.3.1 Charging Effectiveness

The evaluation of the heat storage process is based upon two assumptions about optimal LHTSD behavior. First, the salts should be melted as soon as possible: a greater percentage of energy stored as latent heat ensures an even cooking temperature and reduces energy loss by keeping the overall temperature of the device as low as possible. Second, the device should absorb heat as evenly as possible. Hot spots near the inlet both inhibit further absorption of heat and encourage excess loss of heat through the sides of the container.

Although the fours designs performed similarly in the heat supply phase, there were important differences. In terms of melting efficiency, for instance, design 2 was the clear outlier. Most importantly, in the early stages of the charging process this design lagged behind the other three in melting the salts (Figure 16). The reason for this difference lies in the way that convection currents developed in the three different models. Designs 1, 2, and 3 all have a slanted core surface near the receiving plate. When the core near the receiving plate reached melting temperatures, a small layer of melted salts quickly

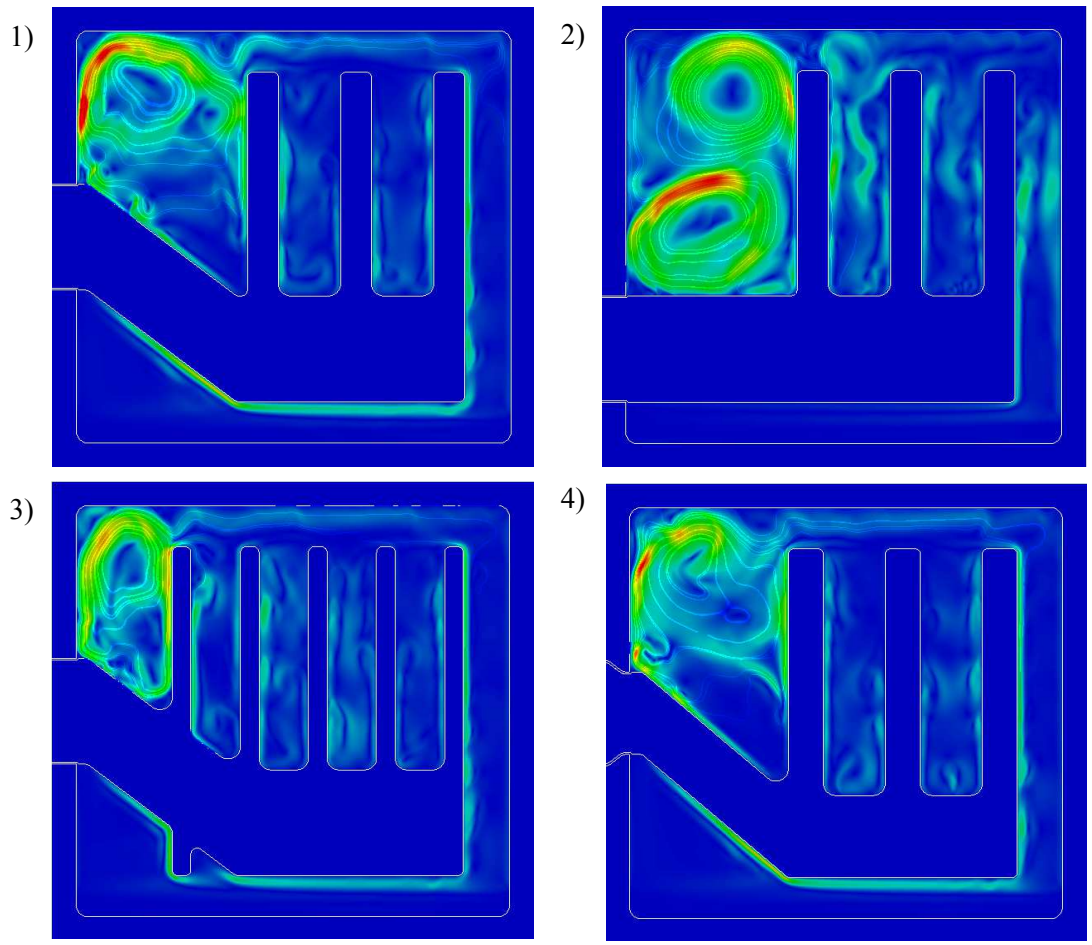

Figure 17. Velocity magnitude and streamlines in designs 1-4 at the height of the charging on the second day (2:00 pm). In designs 1 and 4 the pattern is dominated by the flow coming up from the hottest part of the core, near the inlet. In designs 2 and 3, though, this flow is more in balance with the flow coming on the side of the first fin.

established itself near that surface. The buoyancy-induced flow within this layer, along with the very high temperatures of the core near the left wall, created a strong flow up the side of the device. This flow spread heat quickly into the upper region and right-side of these devices. But convection flow developed differently in Design 2. This design does not have a slanted surface, and so the upward flow near the inlet was slower to gain strength, and the smaller plumes along the top of the core were repressed by the frozen salts. This weaker flow pattern reduced the ability of design 2 to spread heat into the

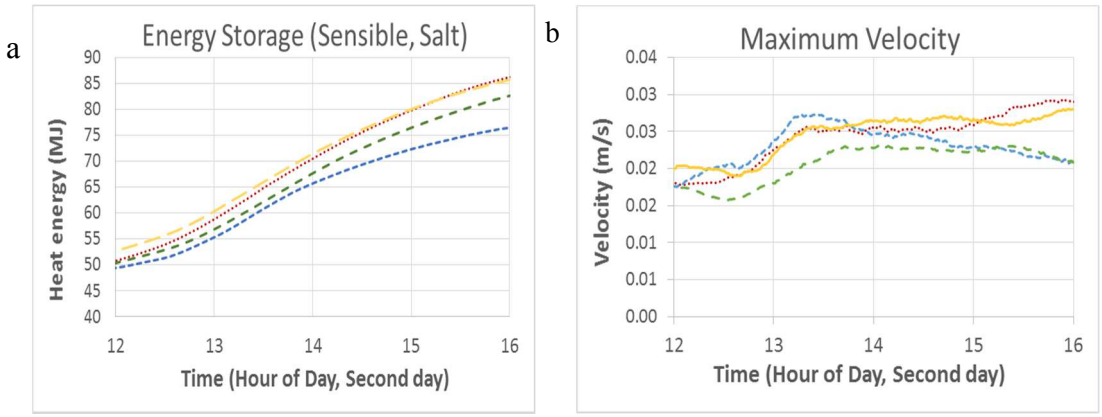

Figure 18. (a) Sensible energy storage in the salts during second day charging. (b) Maximum velocity within salts during second day charging. The stronger convection currents of designs 1 and 4, evident in their higher maximum velocities, led to a higher storage of energy within the salts during this charging period.

interior the device: Figure 16 shows that the development of the melted region in design 2 significantly lags that in the other designs at 11:00 on the second day.

There are some advantages to design 2 with respect to the melting process. Late in the charging period of both days, for instance, the melt fraction of design 2 surpasses that of the other three designs (Figure 15). The primary reason for this is that there is less salt below the aluminum in this design; as all of the designs approach full melt, design 2 is the only design that does not have a pocket of frozen salts in the lower left corner of the device. In addition, the flow patterns that develop in design 2 keeps the hottest salts away from the left wall, which leads to smaller heat losses through the insulation. Ultimately, however, these advantages are less significant than its disadvantages: the slow developing convection currents in the first part of the melt means that this design is less able to bring heat into the device quickly. Note that in the present simulations the heat flux is set to be constant during the supply phase, which is a simplification of the way in which heat is conveyed into the

interior in a physical system. In a physical situation, designs 1, 3, and 4 would allow more energy to enter the system and would decrease the charging time by moving heat quickly away from the inlet with convection currents.

This analysis of the melting patterns in the four designs points to the importance of convection patterns and hence the fin geometry in creating a uniform spread of temperature in the device. Salt has a thermal conductivity only one order of magnitude higher than the insulation (0.46 vs. 0.052 W/mK): as a result, diffusion is not an effective way to spread heat within the salts. But in practice designing for convection is a tricky process. Figure 17 shows the velocity field of the four designs during the charging period on the second day. Early in the charging process, the dominant flow pattern is the buoyancy-driven upwelling flow from the core near the inlet (see Figure 16). This continues to be the case later in the period for designs 1 and 4, and this is an effective process: the flow moves heat away from the core inlet across the top and over to the right side of the device. There is some inefficiency in storing the hottest liquid near the top of the container, but the resulting flow pattern also works to heat the fins as the hot liquid comes in contact with them.

The particular geometries of designs 2 and 3, however, create different flow patterns that are less effective at spreading heat through the system. As noted above, in designs 1 and 4, the high temperature of the core near the inlet creates a strong clockwise flow that carries heat into the upper right region of the device. But in designs 2 and 3, this clockwise flow is inhibited by the counterclockwise flow created by the high temperature of the first fin (Figure 19). In the case of design 3, this occurs because the first fin is closer to the inlet and so it heats up more effectively than in the other designs. In design 2, this counterclockwise flow results from the relative weakness of the flow coming from near the core inlet. In both cases, however, this unexpected competition between the two flows leads to a less effective charging process. In design 3, the flow is partly blocked by the counterclockwise fin flow, but is also confined by the smaller space in the upper left hand corner of the container. In design 2, the opposing flow is so strong that it creates a

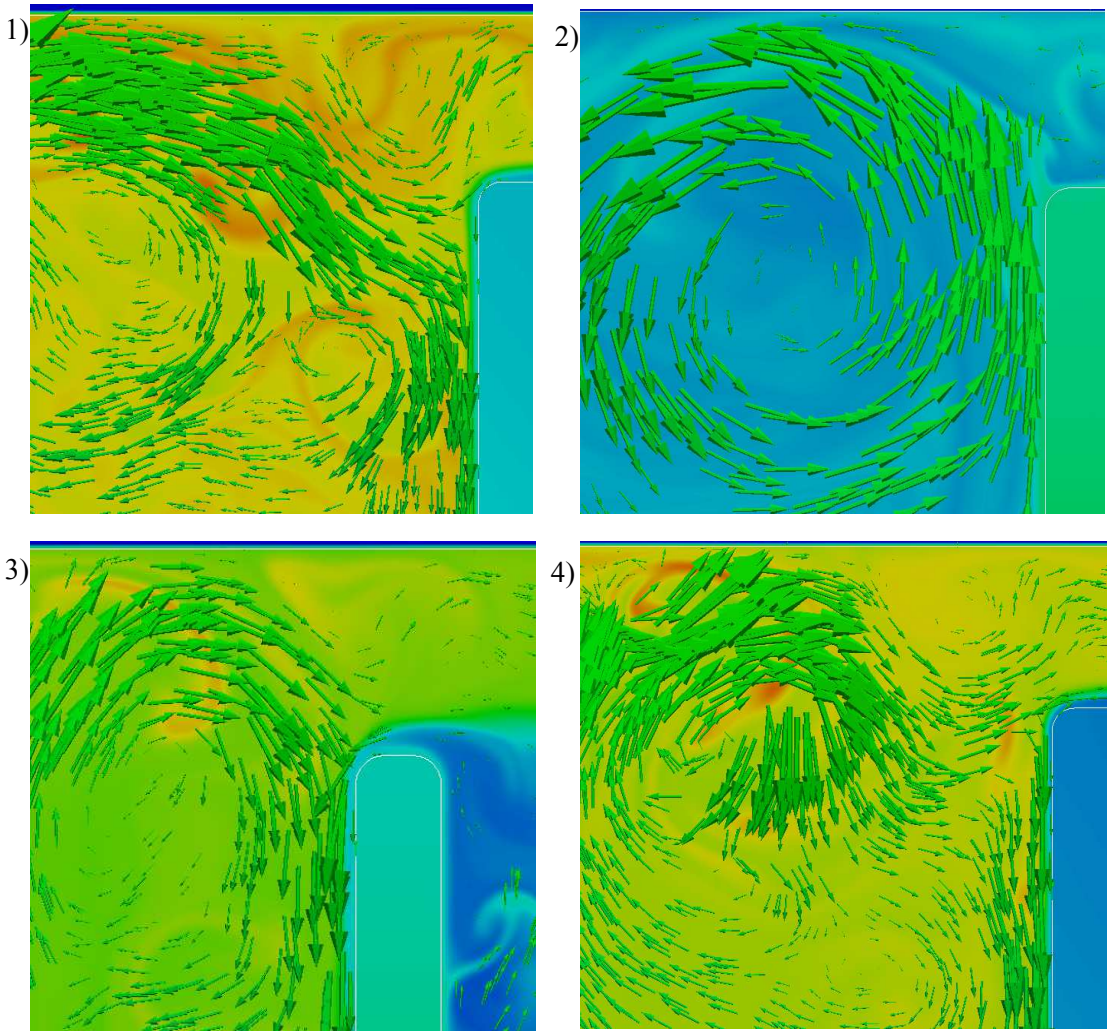

Figure 19. Temperature field with velocity arrows for designs 1-4 at 2:00 on the second day in the upper left corner near the first fin. Designs 1 and 4 have similar flow patterns: the clockwise rotation causes a portion of this high heat flow to move right past the top of the first fin. Design 3 also has a clockwise advection, but the it is more confined, weaker, and less apt to push heat over the top of the first fin. The first fin of Design 2 is hotter than the salts, which leads to a counterclockwise flow that nearly eliminates the convection of heat over the top of the first fin.

multicellular flow pattern in the upper left hand corner of the device, effectively arresting the advection of heat energy from the hotter left side to the cooler right side. In both cases, the competing flows reduce convective velocities and block heat from spreading as effectively as it does in designs 1 and 4 (See Figure 18 and Figure 19).

The two designs that are most effective in the charging process are designs 1 and 4, as they are able to begin the melting process more quickly and spread heat more efficiently through convection than the other two. Design 3 performed nearly as well, particularly in spreading heat throughout the device with its five-finned aluminum core, but the fact that the first fin is closer to the core inlet limited the effectiveness of the convective flow created near the core inlet. And although design 2 was able to achieve full melt first, it struggled to melt the salts early in the process and had a less effective flow pattern, both tendencies that limited its ability to spread heat through the entire container.

2.3.2 Efficacy of Heat Withdrawal

The ideal LHTSD behavior during the heat withdrawal phase for cooking applications would be to maintain as small temperature gradients as possible within the device. This is particularly true within the aluminum, since the receiver plate that serves as the heat outlet provides the heat for cooking. Evaluating this response requires a different set of criteria for the different types of outflux in the simulations. There are two distinct types of boundary conditions imposed to simulate heat withdrawal. In the evening (hours 5:30-8:00) a constant Neumann flux equivalent to 850 W is applied. In the morning (6:20-7:30) a constant Dirichlet boundary condition of 130 °C is applied.

For the Neumann boundaries, the effectiveness of the cooking process can be measured by recording the temperature near the outlet plate. A strong design would maintain a high temperature, indicating that as heat leaves the outlet the aluminum fins are pulling sufficient heat out of the center of the LHTSD to maintain a steady temperature near the outlet. In other words, a good design should maintain a high outlet temperature even in the midst of a high outflux of heat.

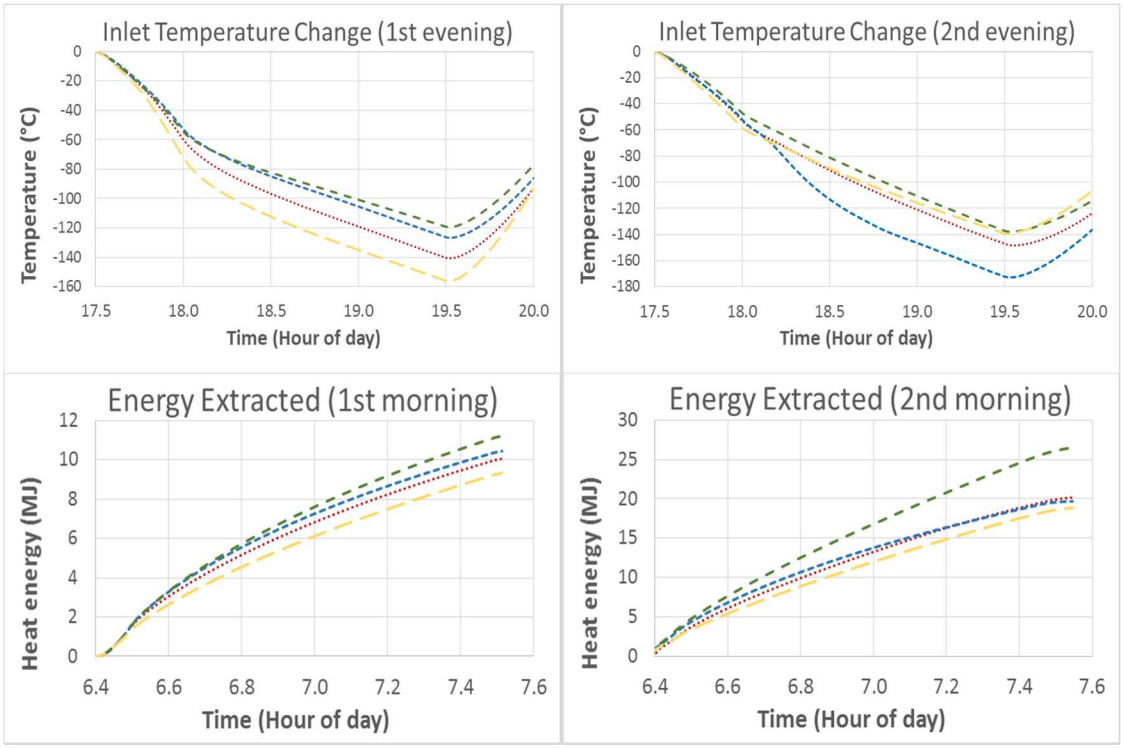

Figure 20. Reaction of the designs to an outflow of energy. The top two graphs show the response of the temperature just inside the inlet boundary to a Neumann boundary condition (-850 W, with a ramp up and down on each side). The bottom two show the energy pulled from each device during the mornings, when a Dirichlet boundary condition (130 °C) is set at the inlet.

For the Dirichlet boundary, the heat withdrawal effectiveness of a design can be indicated by the temperature gradient at the boundary—that is, by the outflux of energy. As with the Neumann boundary condition, an ideal design would maintain high temperatures in the region near the outlet even as significant heat is leaving the device. In the case of the Dirichlet boundary condition, this would mean higher temperature gradients at the boundary, since the boundary temperature is constant; this higher gradient near the

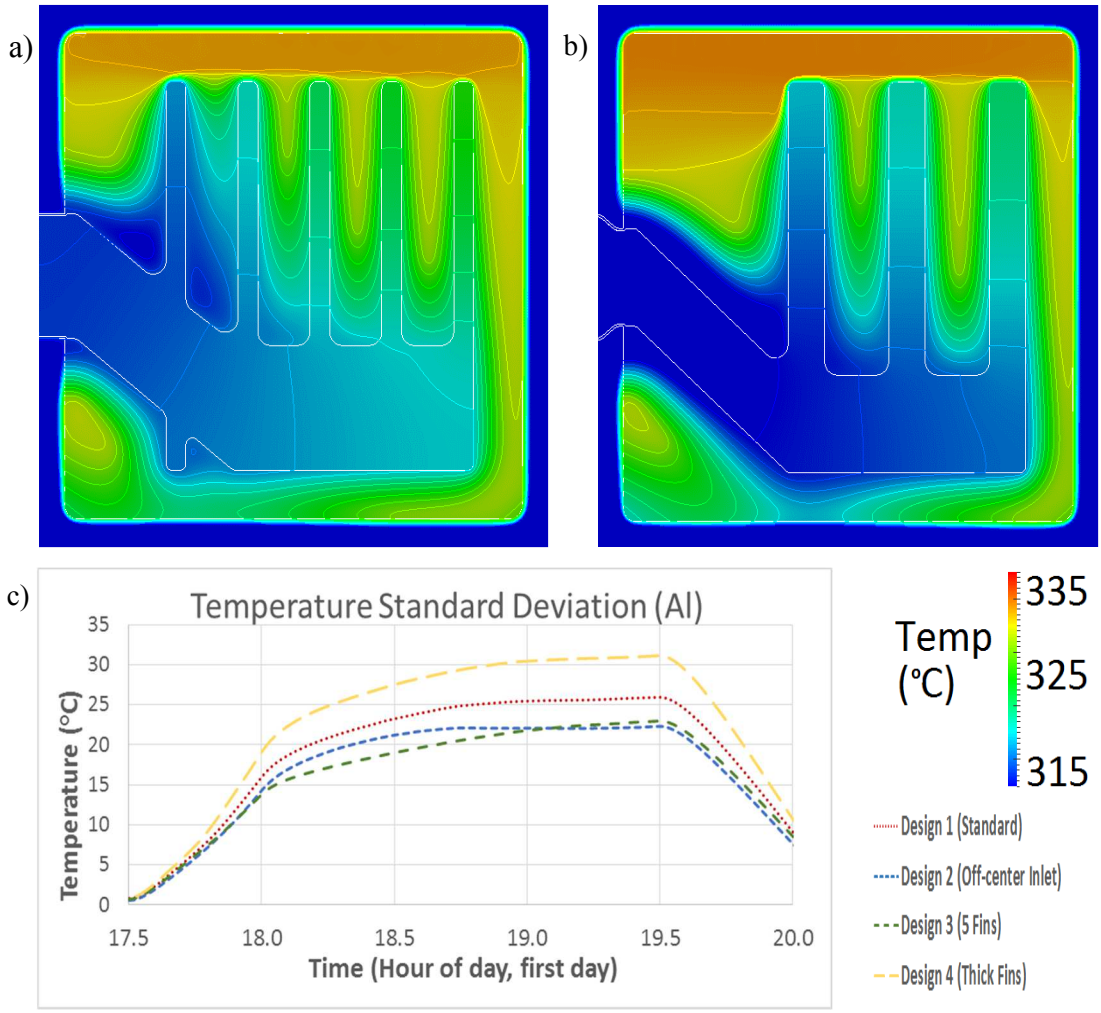

Figure 21. Temperature contours of designs 3 (a) and 4 (b) near the end of the Neumann outflux on the first evening (8:00). The superiority of design 3 is visible in the higher temperatures near the outlet as well as near the ends of the fins. (c) Standard deviation (σ_T) during outflux: designs 2 and 3 maintain even temperatures within the aluminum.

outlet would translate into a higher heat outflux. In physical terms, an ideal design would provide a higher outflux of energy in the presence of a defined temperature at the outlet: i.e. the better design would be capable of sustaining a boil on a larger quantity of water than a less effective design.

Over the four outflux periods, a clear hierarchy among the four designs is observed from the computed results (see Figure 20). Design 3 performs the most effectively, followed by 2, 1, and 4. This is apparent in each of the four cooking periods, and is reinforced by standard deviation (σ_T) measures within the aluminum, which show that design 3 is able to maintain the most even temperature field during the outflux periods (see Figure 21).

The reasons for the different effectiveness of the designs have to do with their design characteristics. Design 4, which is characterized by its more slender core and thicker fins, is unable to move enough energy through its core fast enough to replenish the outflux through the boundary: this flaw is apparent as well in the charging process, where σ_T within the aluminum in this design is considerably higher than the other designs. For design 4, there is not enough aluminum in the core to carry the heat energy to and from the surfaces of the fins.

Design 3, on the other hand, is highly effective in the cooking process because of its large aluminum surface area (see Table 4). Figure 21 shows that in the midst of the outflux period, the fins far from the outlet in design 3 maintain a much higher temperature than those in design 4, despite the similar overall temperature levels near the top of the two devices. Because the fins in design 3 are thinner, the salts are able to replace the heat leaving the fins more evenly, and so the fins maintain a temperature that is closer to the temperature of the salts surrounding them. These warmer fins are then able to move energy back into the aluminum core as the core is cooled by the outflux of heat. Certainly if the design was altered to make the fins thinner and thinner, there would be a point at which the fins would become too thin to carry heat effectively to the core. But design 3 has not reached that point, and the high surface area of its fins allows its aluminum core to stay significantly hotter than the core of design 4.

The above simulations point to some clear design guidelines to improve the efficiency of the thermal storage device during both the heat input and heat withdrawal

phases. First, they confirm the effectiveness of a high surface area for the aluminum fins in the heat withdrawal process, while suggesting that the thickness of the fins is of lesser importance. Second, they demonstrate that core thickness does matter: the thinner core of design 4, for instance, led to lower heat withdrawal effectiveness. Third, the relative weakness of the convective flows in design 2 and 3 suggest that is important to consider the ways that a geometric feature might affect the development of melting flow patterns: for instance, the simulations show that a horizontal core rather than a slanted core, as in design 2, or smaller salt-filled spaces, as in design 3, can stifle the convective flows that are the chief means of spreading heat in the charging process.

2.4 Conclusion

Four designs for an LHTSD were simulated over a 48 hour period in order to evaluate design features for their ability to absorb heat and release heat effectively while maintaining desired temperature distributions in the unit. The input and withdrawal of heat do not require the same characteristics, and so effectiveness in absorbing energy does not imply good performance in releasing energy. The design that performed the best across both processes was design 3, a design which featured a higher number of thinner fins than the standard design 1. While its tighter spacing between fins limited the effectiveness of the convective spread of heat, this was balanced by the increased effectiveness allowed by its larger surface area to remove heat from the melted and solidified salts. Design 2, which was distinguished from design 1 by its off-center receiving plate, was the least effective option. It was better than average at heat withdrawal, but was slow to spread heat in the charging process.

It is important to note that the wide range of possible configurations and the computational expense of the simulations makes it challenging to thoroughly test all, or even a wide range of design possibilities. Instead, these four tests aim to demonstrate the

viability of long term simulations of complex phase change and conjugate heat transfer phenomena, and to provide a rough basis with which to understand the performance characteristics of various design options. Future work will develop ways to use surrogate modeling [79] so that a limited number of simulations can be used to identify an optimal design.

The results of this chapter carry important implications for LHTSD design in general. It is clearly crucial to develop a strong convective pattern in order to melt and heat an LHTSD evenly and effectively. But as this work demonstrates, these patterns, because they depend on the interaction of complex geometry, the temperature field, and material properties, are difficult to predict: it would be difficult to intuit that a particular design (design 2 in the present case for instance) would produce a particular (e.g. unicellular as opposed to multicellular) flow pattern while the other designs would not. And yet it would be difficult—and expensive—to determine from physical experiments what was limiting the effectiveness of such a design (e.g. design 2). The type of long-term simulations performed in this work provides a way to understand the complex patterns that develop over long periods of time. In addition, a small number of these long simulations, by giving us a better sense of these patterns, can inform the way to best set up shorter-term simulations. By combining judiciously chosen short-term simulations and using an optimization approach, such as surrogate modeling, chapter four will demonstrate that this numerical scheme can be an effective design tool to configure LHTSDs for solar applications.

CHAPTER THREE
INVESTIGATION OF SOLAR SALTS USING 3-D SIMULATIONS AND EXPERIMENTS

Solar salts, a mixture of KNO_3 and $NaNO_3$, are commonly used phase change materials (PCM) for latent heat thermal storage devices (TSD). The melting behavior of the salts is important to the performance of those LHTSDs which routinely move between a solid and a liquid state. In such cases, convective flow and melt behavior can significantly impact the transfer of heat through the low thermal-conductivity PCM. While the material characteristics of solar salts have been studied extensively, significant uncertainty remains concerning their thermal behavior in practical situations, and little work has been done to describe the melt development of the salts within 3-dimensional complex geometries.

To obtain a fuller picture of latent heat thermal storage using solar salts, this chapter describes experiments and three-dimensional computational simulations of melting solar salts in an aluminum container. A heating element is placed under a closed aluminum container filled with solar salts, both with and without aluminum fins. Accurate simulations are performed by first identifying thermal properties that lead to the accurate reproduction of experimental results. The numerical results are then used to describe the dynamics of the solid-liquid front and flow patterns within the container. The combined experimental and computational results provide insight into the thermal, flow, and melt behavior of solar salts. The experimentally validated simulation capability can be used for the design of efficient thermal storage devices using solar salts.

3.1 Introduction

An improved ability to store solar energy is expected to play a key role in the reduction of global fossil fuel use. While electric batteries receive the bulk of attention in

this regard, an important complementary strategy is thermal storage: waste heat or solar energy captured and stored within a bulk material that can be withdrawn later in a usable form. Perhaps the most promising approach for heat storage involves the use of phase change materials (PCM) as a medium in thermal storage systems [17-19]. Latent heat storage systems have the advantage of higher rates of energy storage per unit volume and consequently a narrower operating temperature range than sensible heat storage devices. Because the solidification process occurs over a significant time duration at a known heat of solidification, they also offer the possibility of a long-lasting, steady-temperature heat source [8, 20-22].

The use of a PCM-based storage system requires two key decisions: the material used to store the energy and how best to transfer heat into and out of that material. The material choice depends on melting temperature, stability, energy density, and cost, among other things. One of the most common PCMs is a near-eutectic mixture of $NaNO_3$ and KNO_3, with a 60/40% ratio by weight; this mixture is commonly called "solar salt" [23]. Solar salts have moderately high solidus temperature (219-222 °C), are stable under temperatures below 550 °C, have a high specific heat and latent heat of fusion, and are relatively inexpensive [23]. The second key decision concerns the mechanisms for transferring energy into and out of the LHTSD. The chief engineering challenge in building an effective LHTSD is finding a way to complement the storage capabilities provided by the PCM, which typically has a low thermal conductivity, with an enhanced heat transfer strategy. There are multiple approaches to enhance heat transfer. These include enhancement of the thermal conductivity of the PCM itself as well as the inclusion of additional high-conductivity pathways within the PCM [27, 32, 80-82]. The former strategy [83] includes doping the PCM with highly conductive nanoparticles [84], impregnation of porous materials such as expanded graphite or metal foam into the PCM [29, 85-87], and the inclusion of low-density materials like carbon fibers within the PCM [88]. The latter approach includes the encapsulation of the PCM in a protective polymer

coating [28, 89, 90] and the use of heat pipes to carry thermal energy between a heat transfer fluid and the PCM [91, 92]. However, the most common (and cost-effective) strategy to enhance heat transfer into and out of a PCM thermal storage unit is the use of high conductivity fins [17, 32, 93]. Previous computational and experimental work on finned heat spreaders demonstrates that they consistently enhance heat transfer within a variety of types of LHTSDs [94], including containers with flat plate fins [95, 96], axial fins [97, 98], and circular fins [99-101].

The thermal characteristics of solar salts have received significant attention, in their solid form [4, 102, 103], their molten form [1, 104-107], and during phase change [3, 108-111]. However, little experimental work has been done to describe the melting and solidification behavior of solar salts, particularly within a complex, finned geometry. Such experiments are important, for two reasons. First, thermal storage devices used in real scale applications often do not match performance predictions based on thermal characteristics measured in idealized situations [112]; a more accurate knowledge of material behavior within complex conditions would improve the design of practical LHTSDs. Second, much of the work on improving the heat transfer capabilities of finned devices has found that the geometry of the fins and the overall geometry of the LHTSD is a crucial variable in increasing effectiveness. However, these studies often conclude that it is difficult to develop general design guidelines across a wide range of materials, operating conditions, and uses [33-35, 38-41, 113, 114]. Given the strong dependence of effective heat transfer enhancement on a particular design or arrangement of fins, enhanced general understanding of the behavior of solar salts will lead to better initial designs for LHTSDs. This is particularly applicable to cases where the PCM cycles between a solid and a liquid state; knowledge of the convective flow patterns, melt front development, and thermal characteristics of solar salts can help improve the LHTSD design.

The lack of experimental studies of the flow and melt behavior of solar salts is partly due to the difficulty in observing this behavior visually. Physical experiments

without visual access to the interior of the domain can provide hard data on temperature changes within the LHTSD, but they do not provide information on phase change and flow patterns. Numerical simulations, on the other hand, provide detailed pictures of the flow development, but must be validated against experimental data. To address these complementary needs, the present work synthesizes experimental and numerical work. However, the experimental results are not simply used to validate the solver; such validation work was completed in an earlier study [115]. Instead, the simulations are used to better understand the detailed thermocouple (TC) data from the experimental work. The physical experiment involves a closed aluminum container filled with solar salts and heated from below, both with and without aluminum fins. TC readings provide a map of the transient temperature field within the interior of the LHTSD. Three-dimensional computational simulations are designed to match this TC data: this matching process produces not only images of the flow and melt boundary within the container but also information about the thermal properties of the solar salts within a practical LHTSD. This combination of numerical and experimental results provides insight into the practical behavior of the solar salts before, during, and after phase change. In doing so, it advances the capabilities for designing efficient thermal storage devices.

3.2 Methods

3.2.1 Experimental Method

The project consists of two sets of physical experiments. The first set melts and solidifies solar salts in an empty chamber made from Al-6061, insulated at the sides by 7.6 cm thick fiberglass insulation (Figure 22(a)). The second uses the same chamber but includes an aluminum core with three vertical fins placed around the core (Figure 22(b)). Table 6 details the masses of the components of the experimental container. In both cases, the room temperature chamber is heated from its base until an average salt temperature of

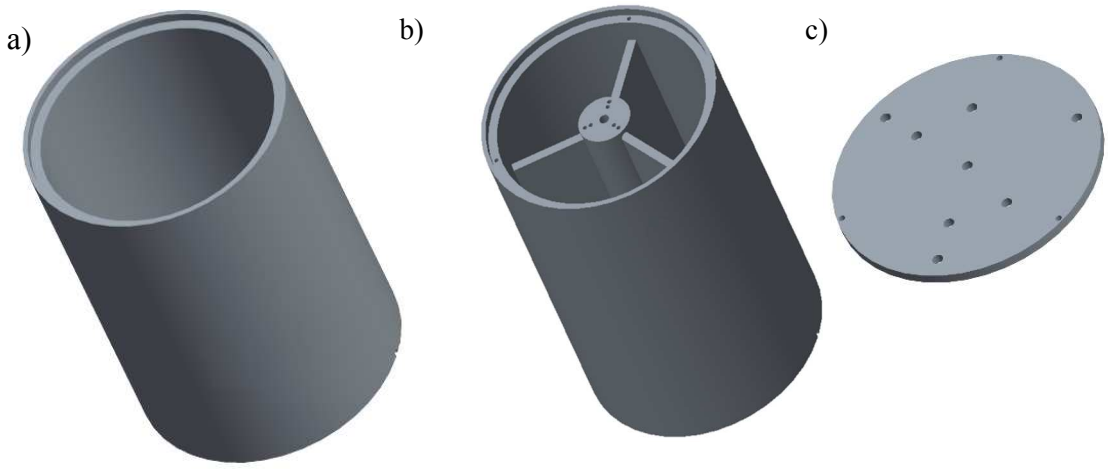

Figure 22. Test chamber for (a) no-fin and (b) finned experiments. The lid (c) is used in both sets of experiments.

Table 6: Mass of Experimental Chamber

Item	Mass (g)	Item	Mass (g)
Chamber	506.0	No-fin device, total aluminum	551.7
Core	61.4	Finned device, total aluminum	697.8
Fin (each)	28.4	Solar Salts	650.0
Lid	45.2		

approximately 310 °C is reached, at which point the heat flux stops. The chambers are then allowed to cool to room temperature. For each geometry, the experiment is run a total of fifteen times: five with the TCs at a position near the top of the salt in the chamber, five with the TCs at a middle position, and five with the TCs near the bottom of the chamber. The eight TCs were set at four symmetrically distinct positions at each of the three levels. Figure 23 shows the dimensions for the aluminum chamber and details the positions of the TCs for both sets of experiments.

The finned core combines an aluminum rod with 3 radially symmetric fins, spaced equally about the cylinder axis. The core was bored with an 8.9 cm deep blind hole through

the axis to allow for the insertion of a thermocouple. The 0.159 cm diameter (1/16") TC was inserted in the 0.345 cm diameter hole, which results in a clearance fit of 0.093 cm on each side; to ensure contact between the TC and the aluminum, the tip of the TC is bent. The core is attached to the chamber with a 10-24x0.75" 316 stainless steel (SS) cup-point set screw at the base of the core; using a set screw allowed the core to be securely attached to the base without necessitating a large diameter through-hole through the core. A SS super heli-coil fastener was set flush to the inside surface of the enclosure so the 10-24 SS set screw could mate securely with the aluminum, as previous testing showed that the different rates of thermal expansion between the aluminum enclosure and SS fastener would cause the threads to shear away from the container. For both sets of experiments, the chamber is fitted with an aluminum lid that allows for a tight clearance fit of the temperature probes and aids in their positioning (see Figure 22(c)). The lid is fixed to the

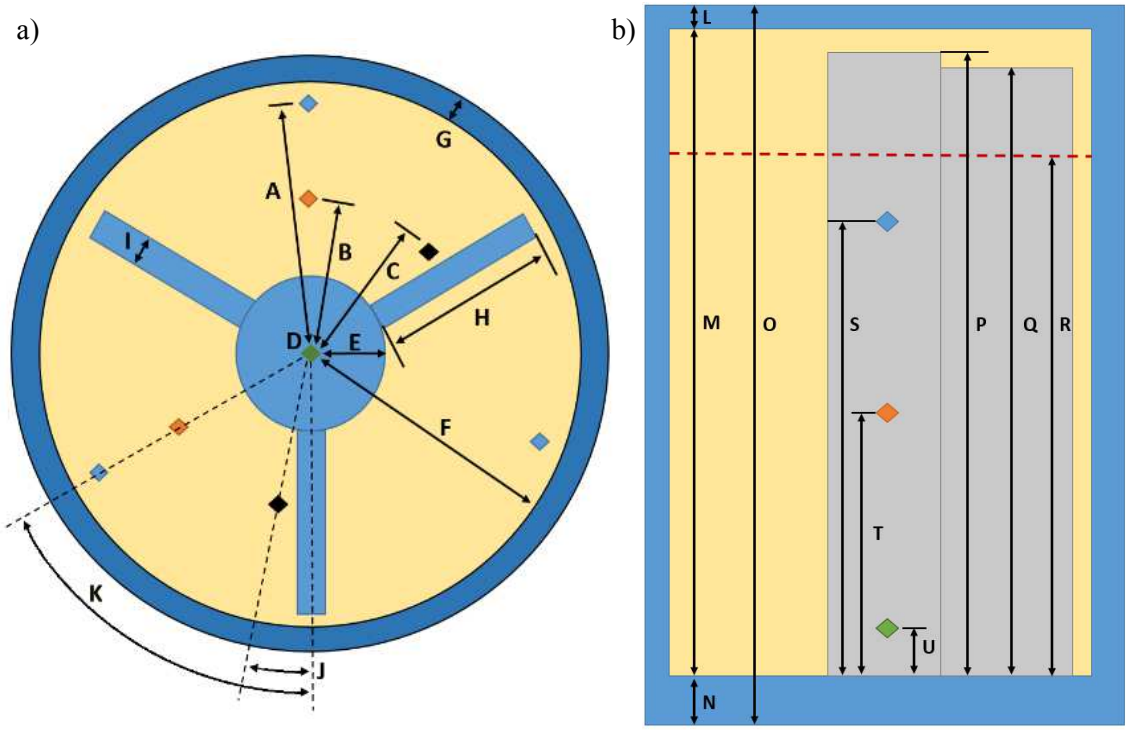

A	Distance to outer TC (blue)	3.51 cm	L	Lid thickness	0.32 cm	
B	Distance to inner TC (orange)	2.16 cm	M	Chamber interior height	10.80 cm	
C	Distance to fin TC (black)	2.16 cm	N	Bottom thickness	0.95 cm	
D	Center TC (green)		O	Chamber exterior height	12.07 cm	
E	Core radius	0.95 cm	P	Core height	10.48 cm	
F	Chamber radius	3.81 cm	Q	Fin height	10.16 cm	
G	Chamber thickness	0.49 cm			*No-fin*	*Finned*
H	Fin width	2.63 cm	R	Approximate liquid salt height	7.18 cm	8.41 cm
I	Fin thickness	0.32 cm	S	Top thermocouple height	6.23 cm	7.17 cm
J	Angle between fin TC and fin	11.4°	T	Middle thermocouple height	3.59 cm	4.22 cm
K	Angle between other TCs and fin	60.0°	U	Bottom thermocouple height	0.64 cm	0.64 cm

Figure 23. Dimensions for experimental chamber, including thermocouple (TC) positions.

enclosure via 3 1-72x .25" SS UNC hex screws. High temperature fiberglass insulation (7.6 cm) is applied to the enclosure's external wall. The salt samples are prepared by weighing the constituent components at 40%wt KNO3 and 60%wt NaNO. After grinding each sample once in a mill grinder, the salts are mixed and ground a second time. The sample is then dried for 8 hours at 100 °C to remove moisture. The sample is poured into the enclosure, brought to 350 °C for 4 hours, and then allowed to solidify. For each TC

position, the system is brought to a liquid state and the TCs are traversed to the correct position. The system returns to the ambient temperature before trials are conducted.

During the heating phase of the experiments, the chamber is heated using a Fisher electronics hot plate. The heat rate is set to 456 watts for all experimental runs. The power input is controlled, monitored and logged using a variable autotransformer and a Watt's Up watt meter. Thermal phenomena are observed using an array of 1/8" stainless steel, grounded, OMEGA TJ-36x type-K TCs. The TCs, which are calibrated using an omega dry block, and fastened to the thermocouple holding plate using 1/8" NPT Yor-Loks with SS ferrules. The calibration uncertainty of the TCs is 1.55 °C. The radial and vertical positions of the TCs are shown in Figure 23. The TCs are positioned at the different vertical locations using a Hayden Kirk stepper motor-driven linear traverse controlled by a ST-5 stepper drive, with step and direction inputs generated by digital I/O lines on a National Instruments data acquisition board and LVIEW VI. The thermocouple carriage was traversed at 25,000 step/rev with a supplied frequency of 10,000hz; the systematic uncertainty of the vertical position is 0.01 cm. During all experiments, temperature readings were sampled at 1Hz using a NI 6320 PCIe and 9212 DAQ card.

3.2.2 Numerical Methods

Governing Equations

The governing equations for the simulations are the three-dimensional Navier-Stokes equations and the energy equation. An abbreviated explanation of the governing equations and the core discretization process are provided here; a more detailed explanation is available in chapter one. The mass balance equation is:

$$\frac{\partial u}{\partial x}+\frac{\partial v}{\partial y}+\frac{\partial w}{\partial z}=0 \tag{32}$$

where u, v, and w are the dimensional velocities. The momentum balance and energy equations are:

$$\frac{\partial u}{\partial t}+\frac{\partial(uu)}{\partial x}+\frac{\partial(uv)}{\partial y}+\frac{\partial(uw)}{\partial z}=-\frac{1}{\rho}\frac{\partial p}{\partial x}+\quad \nu\left(\frac{\partial^2 u}{\partial x^2}+\frac{\partial^2 u}{\partial y^2}+\frac{\partial^2 u}{\partial z^2}\right)+Au \tag{33}$$

$$\frac{\partial v}{\partial t}+\frac{\partial(vu)}{\partial x}+\frac{\partial(vv)}{\partial y}+\frac{\partial(vw)}{\partial z}=-\frac{1}{\rho}\frac{\partial p}{\partial y}+\quad \nu\left(\frac{\partial^2 v}{\partial x^2}+\frac{\partial^2 v}{\partial y^2}+\frac{\partial^2 v}{\partial z^2}\right)+Av \tag{34}$$

$$\frac{\partial w}{\partial t}+\frac{\partial(wu)}{\partial x}+\frac{\partial(wv)}{\partial y}+\frac{\partial(ww)}{\partial z} =-\frac{1}{\rho}\frac{\partial p}{\partial z}+\quad \nu\left(\frac{\partial^2 w}{\partial x^2}+\frac{\partial^2 w}{\partial y^2}+\frac{\partial^2 w}{\partial z^2}\right)+Aw+\ g\beta(T-T_{char}) \tag{35}$$

$$\frac{\partial T}{\partial t}+\ u\frac{\partial T}{\partial x}+v\frac{\partial T}{\partial y}+w\frac{\partial T}{\partial z} =\alpha\left(\frac{\partial^2 T}{\partial x^2}+\frac{\partial^2 T}{\partial y^2}+\frac{\partial^2 T}{\partial z^2}\right)+\frac{LS_{trans}}{C_p}\left(\frac{\partial F_{LS}}{\partial t}\right)+\frac{SS_{trans}}{C_p}\left(\frac{\partial F_{SS}}{\partial t}\right) \tag{36}$$

In the above, ν is the kinematic viscosity, ρ is the density, T is the temperature, T_{char} is a characteristic temperature (whose value is discussed below), and β is the coefficient of expansion. In the energy equation, $\alpha = \frac{k}{\rho C_p}$ is the thermal diffusivity, where k is the thermal conductivity and C_p is the heat capacity. The Boussinesq approximation is a valid assumption for these simulations: $\frac{\Delta\rho}{\rho_0}$ is equal to approximately 0.025 for temperature range of these experiments [72], which is well below the 0.1 limit often cited as the upper limit for the validity of the Boussinesq approximation [116].

Unlike earlier chapters, the simulations here take into account two phase changes: a solid-solid transformation and a solid-liquid transformation [4]. SS_{trans} is the energy required for the solid-solid transformation, while LS_{trans} is the latent heat of fusion for the solid-liquid transformation (both in units of $energy/mass$). Both these phase transformations occur over a temperature range [52, 109, 110]; as a result, a cell whose temperature falls within this temperature range will be in a partially transformed state: F_{SS}

is the fraction of solid-solid transformation for a given cell, while F_{SL} is the liquid fraction. Both F_{SS} and F_{LS} have values ranging from 0 to 1. While F_{SS} has no effect on velocity, F_{LS} affects velocity through the coefficient A. The value of A, the non-dimensional permeability term, is defined using a Carmen-Kozeny term, which both matches the physical behavior of a porous medium and eases numerical stiffness at the solid-liquid boundary [52]:

$$A = \frac{C(1 - F_{LS})^3}{(F_{LS}^3) + B} \tag{37}$$

C (units of time^{-1}) and B (unitless) are constants chosen based upon a particular simulation. On the one hand, C/B must be large enough to suppress velocity in cells where $F_{LS} = 0$. On the other, C must be small enough to allow some velocity in cells with fractional value of F_{LS}, thus enabling a gradual transition within the mushy region from zero velocity to unhindered velocity. In the present simulations, B is set to a standard value of .001 [52, 117, 118]. The value of C is discussed below.

Discretization Scheme

As in earlier chapters, the three-dimensional momentum equations are discretized using an implicit second-order central difference scheme, in which continuity is enforced using a pressure-based velocity correction algorithm.

Both phase-change boundaries are determined using the enthalpy-porosity method [51, 52, 62, 119]. After the velocity and pressure fields are finalized, enthalpy is calculated for each cell and used to find F_{LS} or F_{SS} for the cell. This process defines a "mushy" region of extent 2ε, where ε represents half of the phase change temperature range: when the temperature of a cell is between T_{change} - ε and T_{change} + ε, the cell undergoes phase change. The enthalpy H at each cell *i* is calculated using the liquid fraction value from the previous

iteration, or in the case of the first iteration, from a time-extrapolated value based on the previous time steps:

$$H = (F_i * S_{trans}) + C_p(T_i) \tag{38}$$

where F_i is F_{SS} or F_{LS} at cell i, S_{trans} is SS_{trans} or LS_{trans}, and T_i is the temperature at the cell i. The enthalpy H and the definition of the mushy region are used to define F at the new time step:

$$F = \begin{cases} 0, & if\ H < H_{low} \\ \dfrac{H - H_{low}}{H_{high} - H_{low}}, & if\ H_{low} < H < H_{high} \\ 1, & if\ H > H_{high} \end{cases} \tag{39}$$

where

$$H_{low} = C_p(T_{change} - \varepsilon) \tag{40}$$

$$H_{high} = S_{trans} + C_p(T_{change} + \varepsilon) \tag{41}$$

In the case of the liquid-solid phase change, the liquid fraction affects the velocity of the flow: velocity is set to zero if F_{LS} is 0, is partially suppressed in the mushy region between 0 and 1, and is unhindered when $F_{LS} = 1$.

Two numerical parameters have a significant impact on the flow. The values of these discretization parameters are set to duplicate the experimental TC results in the simulations. One of these is C in equation (37). As other researchers have noted, the choice of C can have significant effect on flow patterns and melt boundaries [118, 120]. While the most common values of C range from 10^5-10^6, the accuracy of the choice depends on the nature of the PCM, the solver used, and the scale of the simulation. The present work confirms that different values of C make large differences in the shape of the flow. Values of C ranging from 10^2-10^6 were tested. The most accurate results are found when $C = 5.0 * 10^3$. Although this value is relatively low, it severely restricts the flow in the mushy zone; higher values of C do not change the flow significantly, but do lead to a stiffer solution matrix and higher computational expense.

Similarly, the value of T_{char} in equation (35) changes the flow behavior significantly. T_{char} determines the contribution of buoyancy to the initial velocity. Ideally, the value of T_{char} should not affect the corrected velocity: the pressure correction process should produce the same velocity results irrespective of the relative size of the initial contributions. However, high temperature gradients, high velocity gradients, and the complicated shape of the melted region (especially early in the melting process) can lead to strong numerical stiffness that makes it difficult for the velocity correction scheme to enforce the continuity equation. To ease this problem, T_{char} is defined as:

$$T_{char} = (T_{change} - \varepsilon) + G * (T_{max,\ salt} - (T_{change} - \varepsilon)) \quad (42)$$

where $T_{max,\ salt}$ is the maximum temperature within the salts, $T_{change} - \varepsilon$ is solidus temperature, and G is a fraction from 0 to 1. The effect of this dynamic parameter is to define T_{char} as a value in between the solidus temperature and the maximum salt temperature; in doing so, it controls how much of the initial uncorrected buoyancy velocity is upward or downward in relation to gravity. At regular intervals, T_{max} is recalculated, and a new T_{char} is defined. Values of G ranging from 0.0 to 0.9 were tested. A low value of G produces a strongly upward flow that melts the salts in the top of the container before those in the bottom; a high value of G restricts that upward flow and leads to a horizontal melt boundary that moves slowly up through the chamber. A value of $G = 0.725$ generates accurate flow behavior.

Non-conservative Convection Scheme for Highly Oscillatory Simulations

As noted in chapter one, a number of factors make the simulations in this thesis susceptible to osciallations in the temperature field: the large difference in thermal diffusivity across the aluminum-salt interface, the narrow melted region that occurs early in simulations, and the fact that the highest velocity and temperature gradients, particularly with vertical geometries, occur next to the solid interface. These problems are amplified when the source of heat is at the bottom of the LHTSD, as it is in this chapter and in chapter

four. As a result, it is necessary to include additional schematic devices to reduce the resulting temperature oscillations without losing accuracy.

The additional tool used to control oscillations in the simulations in these last two chapters is a non-conservative form of convection terms in the governing energy equation. The convection terms in the momentum equation, for comparison, are based on the conservative form of the governing equation and are discretized using a finite volume-type approach; this approach conserves momentum by ensuring that the convected momentum leaving one cell is the same amount of momentum that is entering its neighbor cell along a given cell boundary. The convection for a cell i using this conservative approach is calculated as:

$$\frac{\partial(uu)}{\partial x} + \frac{\partial(uv)}{\partial y} = \frac{u_{i+\frac{1}{2}}u_{i+\frac{1}{2}} - u_{i-\frac{1}{2}}u_{i-\frac{1}{2}}}{\Delta x} + \frac{u_{j+\frac{1}{2}}v_{j+\frac{1}{2}} - u_{j-\frac{1}{2}}v_{j-\frac{1}{2}}}{\Delta y} \tag{43}$$

where $i + 1/2$ represents the cell boundary between i and $i + 1$ while $i - 1/2$ represents the cell boundary between i and $i - 1$ (and likewise for j indices). This conservative approach has the advantage of being more accurate, but when used for the temperature field, can lead to numerical oscillations in areas of high temperature and velocity gradients. The non-conservative form of the convection terms, however, is inherently diffusive: its use adds artificial dissipation that smooths out dispersive effects. The discretization of this non-conservative convection scheme is as follows:

$$u\frac{\partial T}{\partial x} + v\frac{\partial T}{\partial y} = u_i\left(\frac{T_{i+1} - T_{i-1}}{2\Delta x}\right) + v_i\left(\frac{T_{j+1} - T_{j-1}}{2\Delta y}\right) \tag{44}$$

In this form, the amount of convected energy leaving one cell boundary might not be exactly the same as the amount entering its neighbor through the same boundary: in other words, the scheme is not conservative in energy.

This scheme does help to eliminate unphysical oscillations in the temperature field in these very stiff simulations. However, they create a new problem: energy is not fully conserved. This is particularly a problem where the designs are being evaluated for how

well they facilitate the spread of heat through the vessel: a significant surplus or deficit of energy related to numerical error could fully invalidate the results of the simulations.

This problem is solved here by adjusting the convection term additions so that the sum of the additions across the entire domain is near zero. With a conservative finite volume-type scheme, the overall convection addition is automatically zero, since any addition to a call at a given cell boundary is balanced by an identical subtraction from the neighboring cell at the same boundary. As a result, no energy is created or destroyed by convection, as should be the case. With the non-conservative scheme, however, this balance is not ensured. In wall-heated natural convection schemes, for example, there is often one area with high velocities that is also an area with high temperature gradients. The large convection term additions and subtractions in this areas should, in theory, be balanced, but in practice often lead to significant errors.

The error in this balance is only recognizable at the domain (rather than the point) level. To recover a conservative convection term, the domain level error must be quantified and then corrected at the point level. The first step is to calculate the domain level error. This is done by summing in two separate numbers the positive and negative convection term additions at each point in the field (H_{pos} and H_{neg}, respectively). If $H_{pos} > H_{neg}$, it is necessary to reduce positive convection additions across the field until the two values are balanced (i.e. so that the total convection addition in the domain is zero). Therefore, the convection contributions at each cell are recalculated (these calculations are reversed if $H_{neg} > H_{pos}$):

$$H_{final} = \begin{cases} H_{init}, if\ H_{init} \leq 0 \\ H_{init} * R, if\ H_{init} > 0 \end{cases} \quad (45)$$

where H_{init} is the initial calculation of the convection contribution at a cell. R is a ratio ranging from 0 to 1 calculated as:

$$R = \frac{H_{neg}}{H_{pos}} \quad (46)$$

However, since it is assumed that the source of the error is in the areas with large convection terms, the convection additions of either sign below a certain absolute value need not be changed; this level L can be calculated as a percentage (usually in the range from 0.1 to 0.25) of the average absolute convection addition across the domain. Equations (45) and (46) become:

$$H_{final} = \begin{cases} H_{init}, if\ H_{init} \leq L \\ H_{init} * R, if\ H_{init} > L \end{cases} \quad (47)$$

$$R = 1 - \frac{H_{pos} + H_{neg}}{H_{pos,above\ L}} \quad (48)$$

$H_{pos,above\ L}$ is the sum of convection additions across the field above the level L. In essence, this routine removes the total conservation error ($H_{pos} + H_{neg}$) only from cells with large positive convection terms rather than from all the cells with positive convection terms. In either case, the result is that the total domain convection contribution is zero: the process is therefore conservative of energy on a domain level, although not necessarily on a cell level. The value of $R_{pos,\,i}$ and $R_{neg,\,i}$ in these simulations generally ranges from 0.8 to 1.2, where 1.0 represents a simulation with no conservation error.

3.2.3 Simulation Setup

Simulation Domain

The simulation setup, shown in Figure 24, aims to duplicate the experimental setup. However, some adaptations are necessary to facilitate numerical calculations and save computational expense. For instance, small fillets are added at the intersection of aluminum parts (i.e. where the fins meet the bottom of the chamber). More significantly, the size of the simulation domain is reduced in two ways to save computational expense. First, the domain is limited to the volume below the liquid salt level only. This simplification reduces the size of the numerical domain while keeping the mass of salt in

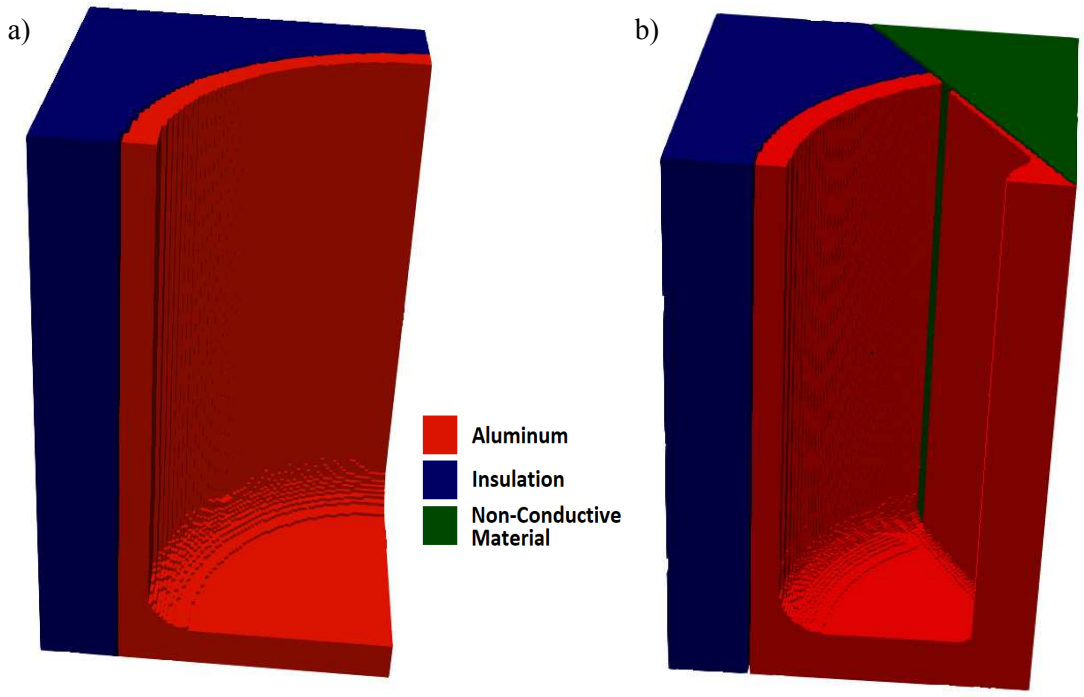

Figure 24. Simulation domain for the (a) no-fin and (b) finned cases.

the domain equal to that within the experimental chamber. The shortening of the domain in this manner depends on several assumptions. The first assumption is that the air above the salts would not significantly impact the flow of salts at their interface: the velocity boundary condition (BC) at this surface is a symmetric BC, which amounts to a shear-free surface of the salts along this boundary. The second assumption is that the changes in volume of the salts due to temperature and phase change are not significant. In the liquid phase, this assumption is reasonable, as the density changes within the temperature range of these experiments are under 3% [72]. The resulting expansion and contraction of the overall volume of the salts within the chamber is unlikely to affect the transfer of heat through conduction or convection.

However, the difference between the density of the solid and liquid salts is about 10% [71, 72]. This is potentially more problematic, both because it could affect thermal

diffusivity of the salts, and because the current simulations do not account for the possibility that solid salts might become detached from the side of the LHTSD and sink within the liquid. These potential problems, however, are of limited concern. First, the effects on thermal diffusivity are tempered by the fact that while density increases by approximately 10% in the solid phase, specific heat decreases by about the same ratio [103, 110]. As a result, the dependency of $1/(\rho C_p)$ on the phase of the solar salts is relatively low (approximately 2% difference between 50 °C and 250 °C). Since specific heat is also held constant in these simulations, thermal diffusivity $\alpha = k/(\rho C_p)$ varies predominately with thermal conductivity k (which is variable in the simulations) in both the physical experiments and the simulations. Second, while recent work that has shown that so-called close contact melting created by sinking solids within a PCM can lead to increases in melting rates [100, 121-123], the effects of close-contact melting are likely to be limited in this work. This is because the experiments depend on the use of 7-8 TCs within the salts, and these TCs would severely restrict the movement of a free-floating solid. This is an unavoidable limitation of the experimental setup, but to duplicate the experimental results, it is necessary to reproduce this condition in the simulations. In any case, there is some evidence that even without the TCs, the effect of close-contact melting would be small. The experimental trials with TCs in the top position, where they do less to constrain the movement of a floating solid, do not reach full melt any faster than the other trials. This suggests that the effects of close-contact melting in this instance, even ignoring the influence of the TCs themselves, are not large. For these reasons, the shortening of the computational domain and its consequent assumption of constant salt density is a reasonable simplification of the experimental conditions.

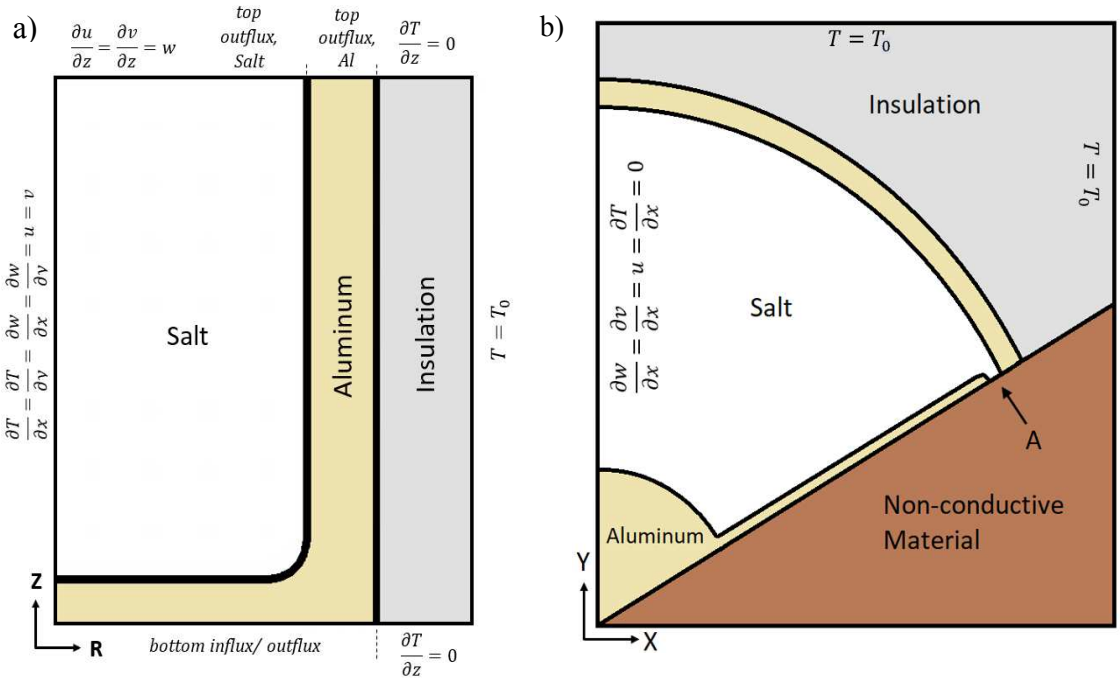

Figure 25. Domain setup and boundary conditions. (a) Axial cross section of the no-fin domain. Because of the rectangular volume of the domain, the insulation thickness is variable in different radial directions; however, the thermal conductivity of the insulation is adjusted to make the thermal resistance in all radial directions equivalent to 7.6 cm of insulation. (b) Radial cross section of the finned domain. The effects of the non-physical no-slip condition at the point marked "A" are assumed to be negligible.

The second modification undertaken in the interest of computational expense is that only a slice of the domain is simulated in both cases. For the no-fin case, the simulation domain contains one quarter of the chamber, while the finned domain contains one sixth of the domain, as shown in Figure 4(b). This reduction of the domain depends on the assumption that the flow is axially symmetric within the no-fin chamber and is symmetric within the subdivisions created by the fins in the finned case. In order to perform the reduced-domain simulation of a three-finned object in a rectangular Cartesian domain, a

Table 7: Material Properties for Simulations			
High temperature insulation		**Aluminum 6061**	
Thermal diffusivity (α)	3.32 x 10^{-7} m^2/s	Thermal diffusivity (α)	7.82 x 10^{-5} m^2/s
Specific heat (C_p)	2767.0 J/(kg K)	Specific heat (C_p)	896 J/(kg K)
Density (ρ)	125.0 kg/ m^3	Density (ρ)	2712 kg/m^3
Thermal conductivity (k)	0.115 W/(m K)	Thermal conductivity (k)	190 W/(m K)
Solar salts (60% $NaNO_3$: 40% KNO_3)			
Kinematic viscosity (*v*)	3.60 x 10^{-6} m^2/s	Coef. of expansion (β)	3.748 x 10^{-4} $°C^{-1}$
Density (ρ)	1925 kg/m^3		

wedge of non-conductive material is introduced into the domain. Figure 25(b) shows that this inclusion depends upon the assumption that the effects of the non-physical no-slip condition at the intersection of the salts and this non-conductive material is not a significant factor in the flow. This assumption presumes that any flow within the volume between the end of the fin and the outside aluminum surface would be severely restricted by the presence of these two solid surfaces. Figure 25 illustrates the simulation domain in elevation and plan views.

Note that the height of the domain for the no-fin simulation (8.13 cm) is shorter than that for the finned simulation (9.36 cm). While the mass of salt is equal in each case, the inclusion of the core and fins within the chamber increases the volume of material in the chamber. As a result, the interior height of the salts (and therefore the height of the domain) is higher in the finned case (see Figure 23).

Material Properties

The material properties of the aluminum and insulation, as well as some reliable properties of solar salts, are listed in Table 7. The thermal properties of the solar salts—

particularly thermal conductivity, specific heat, the solidus and liquidus temperatures, and the latent heat of fusion—are uncertain. These properties are estimated using experimental results. The process used to determine these values and the results of this process are discussed in the Results section below.

Boundary Conditions

Figure 25 also shows the boundary conditions (BC) for the simulations. Since the

Table 8: Simulation Details

Geometry	Simulation Type	Length (m)	Initial Condition (°C)	Neumann BCs in Established Simulation (in Total Flux)		Dirichlet BCs (°C)
				Bottom (W) ($T_{ave,\ Al}$ *in °C)*	*Top (W)* (*t in min.,* $T_{ave,\ Al}$ *in °C)*	*Insulation*
No-fin	*Charge*	70	22.5	138	27.30 + ((t-20)*0.004)	22.5
	Discharge	500	275	< 100 min: 0.141* ($T_{ave,\ Al}$ -22.5) > 100 min: 0.130* ($T_{ave,\ Al}$ -22.5) *Flux is evenly split between top and bottom*		22.5
Finned	*Charge*	80	30	138	21.95 + ((t-35)*0.0011)$^{1.2}$	30
	Discharge	500	275	< 100 min: 0.131* ($T_{ave,\ Al}$ -30) > 100 min: 0.112* ($T_{ave,\ Al}$ -30) *Flux is evenly split between top and bottom*		30

simulation domain is a sector of the experimental apparatus, it is necessary to have both external boundaries (where the insulation borders the outside environment), and internal boundaries (along the slices through the experimental chamber). In both the finned and no-fin case, the two external vertical sides are Dirichlet boundaries, with the temperature set at the T_0, where T_0 is dependent upon the experimental conditions. For the no-fin case, both internal vertical sides are symmetry boundaries (i.e. slip boundaries for velocity and no-flux boundaries for energy). Likewise, the finned case has a symmetry boundary on the

internal vertical side. However, the second internal vertical "boundary" in the finned case is at the interface between the LHTSD and the non-conductive material. This interface acts as an adiabatic boundary, since no heat is conducted through the interface. It also acts as a Dirichlet (solid wall) velocity boundary, where $u = v = w = 0$. As noted in the previous section, this presents a problem only at the narrow strip where the salt meets the non-conductive material. The top and bottom boundaries for the insulation have a no-flux boundary condition, based on the assumption that conduction of heat in a non-radial direction through the insulation is negligible. As discussed above, the velocity boundary condition at the top is a free surface, i.e. zero shear stress boundary.

The dynamic top and bottom energy BCs for the aluminum and salt are determined using the experimental results. The flux of energy into the heating element is known (456 W), but test experiments show that only a portion (approximately 30%) of this flux is conducted into the chamber (contact resistance between the plate and the chamber and heat losses from the plate itself are presumed to be the primary sources of the loss). For this reason, the experimental TC results are used to estimate both the bottom and top fluxes for the simulation. To simplify this process, each experiment is divided into two separate simulations, one for charging and the other for discharging. This eliminates the need to evaluate the BCs in the period immediately after the heat plate is switched off, during which the behavior of the fully melted salts is of limited interest. Initial estimates of the BCs are made by estimating the average sensible and latent heat in the chamber over time using the experimental TC data. It is also assumed that the bottom influx in the charging period is constant (after the initial ramp-up period) and that the change in heat losses at all other flux boundaries occurs smoothly with time. These initial estimates are refined through trial-and-error iterations of the simulations. Figure 26 demonstrates the tools used in this process. An estimate of the average salt temperature, $\bar{T}$, is calculated using a weighted average of TC readings. The weighting procedure is based upon a calculation of the estimated volume of salts represented by each TC: for the no-fin case,

$$\bar{T} = \frac{(4 * \sum_{n=1}^{3} T_{outer}) + (4 * \sum_{n=1}^{3} T_{inner}) + \sum_{n=1}^{3} T_{center}}{27} \quad (49)$$

where T_{outer}, T_{inner}, and T_{center} are the temperatures at the outer, inner and center positions.

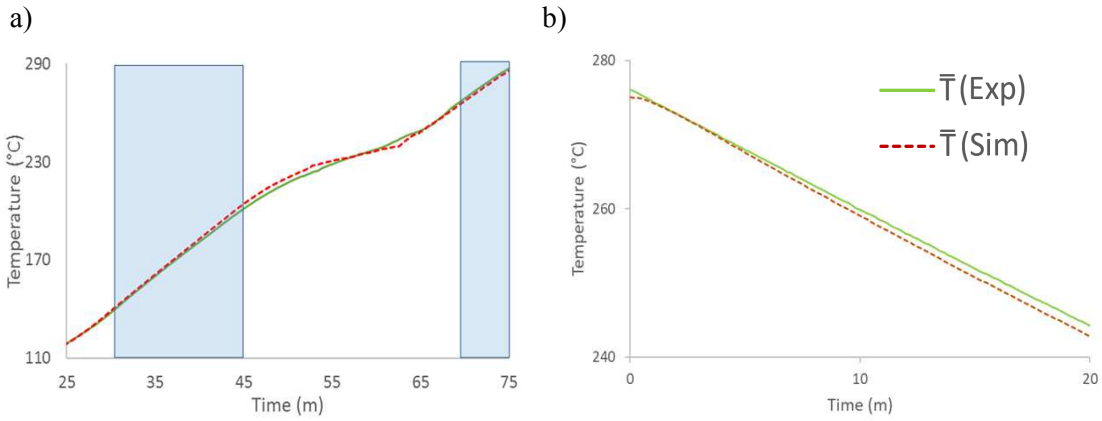

Figure 26. Process used to define flux boundaries. (a) In the charging simulation, the periods both before and after active melting (the blue rectangles) have no change in latent energy. This image from a trial finned simulation shows that the overall flux between 30-45 minutes, represented by the slope of $\bar{T}$, is slightly too high, but that the overall flux after 70 minutes is accurate. (b) In the discharging simulation, the slopes can be compared early in the simulation as well as after solidification has occurred. This plot from a no-fin trial simulation suggests that the outflux during no-fin discharge simulation is too high.

The sum from 1 to 3 adds the top, middle, and bottom TC positions. For the finned case,

$$\bar{T} = \frac{(2 * \sum_{n=1}^{3} T_{outer}) + \sum_{n=1}^{3} T_{inner} + \sum_{n=1}^{3} T_{fin}}{12} \quad (50)$$

where T_{fin} is the temperature at the fin TC. It is assumed that during periods when there is no change in the latent heat within the chamber, the slope of this average salt temperature over time provides a valid estimate of overall change in stored energy for the chamber. In trial simulations, the slope of the simulation average is compared to that of the experimental

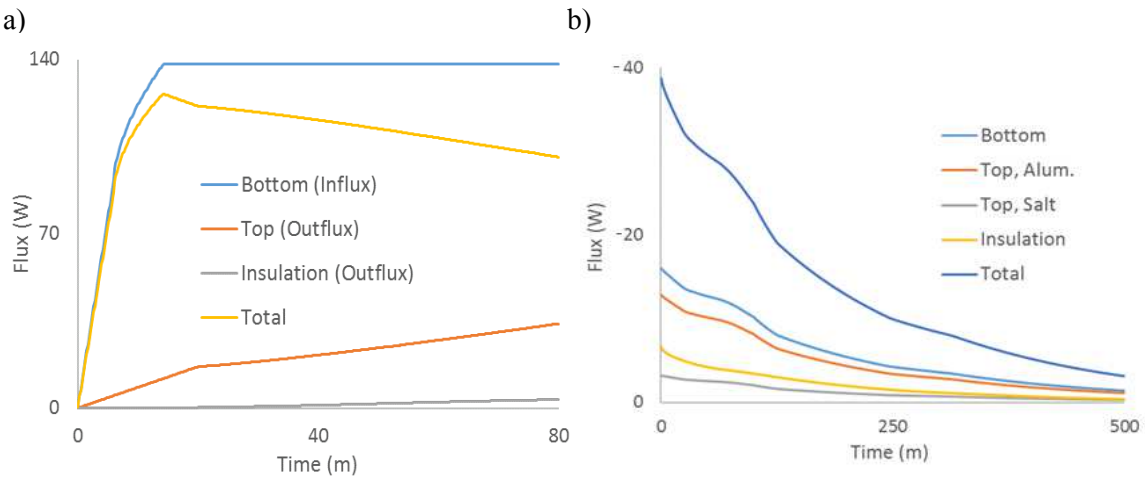

Figure 27. Instantaneous flux at the top, bottom, and through the insulation for (a) the finned charging and (b) finned discharging simulations (all outflux). The flux for the no-fin simulations is similar.

average. The simulation flux is then adjusted as necessary to improve the match between the simulation and the experimental averages.

As shown in Table 8, the finalized flux BCs for the discharging simulations are dependent on the spatially averaged temperature within the aluminum ($T_{ave,\ Al}$): the outflux through the top and bottom BCs is a linear function of ($T_{ave,\ Al} - T_0$). This setup produces accurate results because the outflux in the discharging process is purely a function of passive energy loss through the boundaries of the domain; since the time scale of the simulations makes the aluminum nearly isothermal, these passive losses are consistently a function of $T_{ave,\ Al}$. These conditions, however, do not hold for the charging simulations. For the charging simulations, therefore, it is necessary to define a heat flux as a function of time. Note that the flux in each of the charging BCs ramps up over time in accordance with experimental conditions. 80% of the total flux through the top BC is conducted through the aluminum; the remaining 20% exits through the upper salt surface. Figure 27

illustrates the flux over time for the finned charging and discharging simulations; the flux BCs in the no-fin cases are similar.

3.3 Results

A total of thirty iterations of the melting/solidification process were run: for both the no-fin and finned cases, five experiments were run at each of the three vertical TC positions (top, middle, and bottom). Each experimental run produces data for eight TCs: one at the center of the chamber, two at the fin position, two at the inner radius, and three at the outer radius (see Figure 23(a)). For the purposes of analysis, the TC data has been averaged over those TCs that are placed at the same axial and radial distance. This simplification is justified as the results show only minimal differences amongst the axially symmetric TCs: the standard deviations of the temperature readings at symmetrically identical TCs are typically under 2 °C. The only exception is the top and middle positions during melt in the no-fin case: the asymmetry of the melt boundary in this situation is discussed below in Section 3.3.2. For the no-fin case, this averaging results in three distinct TC positions (outer, inner, and center) at the three vertical stops, for a total of 9 data points. For the finned case, there are four (outer, inner, fin, and core) distinct positions at each vertical stop, resulting in 12 data points. Four simulations were run to reproduce the conditions of the two experimental sets: charging and discharging simulations each for the no-fin and a finned case.

3.3.1 Thermal Properties of Solar Salts

Reliable thermal properties of solar salts, as with other PCMs, are difficult to obtain from the literature. Therefore, before performing the four simulations, it is necessary to settle on the thermal properties of the solar salts, particularly latent heat of fusion, thermal conductivity, specific heat, and solidus/liquids temperatures. Table 9 shows that estimates

of these thermal properties in the literature on solar salts differ as much as +/- 15% from an average value [1]. There are multiple reasons for this uncertainty in solar salt and PCM properties. It is partly due to hysteresis, i.e. the thermal behavior of a material is affected by its previous states; this can lead to different thermal characteristics based upon the rate

Table 9: Solar Salt Thermal Properties

Solar Salt Property	Range of Value within literature	Approximate uncertainty within literature	Final Simulation values
Specific heat (J/(kgK))	1475-1570 (at 300 °C) [1]	+/- 5% [1]	1520
Thermal conductivity	0.41-0.53 (at 300 °C) [1]	+/- 15% [1]	1.65-0.5 (from 20-239 °C) 0.5 (above 239 °C)
Latent heat, liquid-solid (J/g)	102-144 [2]	+/- 16%	85
Solidus temperature (°C)	220-227 [2]	N/A	219
Liquidus temperature (°C)	231-248 [3]	N/A	249 (charging) 239 (discharging)
Latent heat, solid-solid (J/g)	9.5-41 [4] (differences largely due to hysteresis)	N/A	18.87
Solid-solid transition range	106-118 [2, 4]	N/A	104-112 (charging) 82-97 (discharging)

of heating or cooling or the direction of a temperature change. But even controlled experimental attempts to identify stable PCM thermal characteristics can lead to inconsistent results if different sample sizes are used or the tests are performed at different points in a sample history [112, 124]. Solar salts, as a non-eutectic, mixed material, are

particularly susceptible to such uncertainty in material properties: it is affected by

Table 10: Refinement of Thermal Properties

Properties are listed roughly in the order in which they were refined. "Periods of stability" refer to times during the simulation when the latent heat storage (solid-solid and liquid-solid) of the salts is not changing.

Property or Parameter	**Symbol**	**Primary accuracy indicators**	**Related Figure(s)**
Specific Heat	C_p	Value is assumed (1520 J/kgK).	
Top/bottom Flux BCs		Slopes of average salt temperature plots during periods of stability	Figure 26
Thermal Conductivity	k	Temperature differences between internal TCs and TCs near aluminum before melt	Figure 28
Latent heat of transformation	SS_{trans}, LS_{trans}	Time location of periods of stability in relation to each other: if flux is accurate, how long does phase change last?	Figure 29
Solidus/ Liquidus Temperatures	$T_{change} - \varepsilon$, $T_{change} + \varepsilon$	Time-derivative of temperature plots, particularly of TCs undergoing melt/ solidification before other TCs.	Figure 31, Figure 30

hysteresis [4], is subject to material evolution and degradation over time [105, 125], and tends to have sodium-rich and potassium-rich areas in its solid composition [102].

In addition to creating significant problems for engineers designing real-scale projects [112], these uncertainties increase the difficulty of generating accurate numerical simulations. In the present project, initial trial simulations were run using property values recommended in the literature for solar salts [1-4, 72, 102-106, 108-111, 125, 126]. These initial values were then refined through comparison with experimental results. The process used to refine these values is detailed in Table 10. The first step was to assume a specific

heat value for the solar salts. This was necessary because the flux into the system, the specific heat, and the latent heat of transformation are all interdependent. Latent heat, as shown below, can be separated out because it affects only a portion of the simulation, but either the flux or the specific heat would need to be assumed. Specific heat was chosen because uncertainty surrounding this property is relatively low. While Bauer et al. find that there is a +/-5% uncertainty within the literature, this number includes one outlying

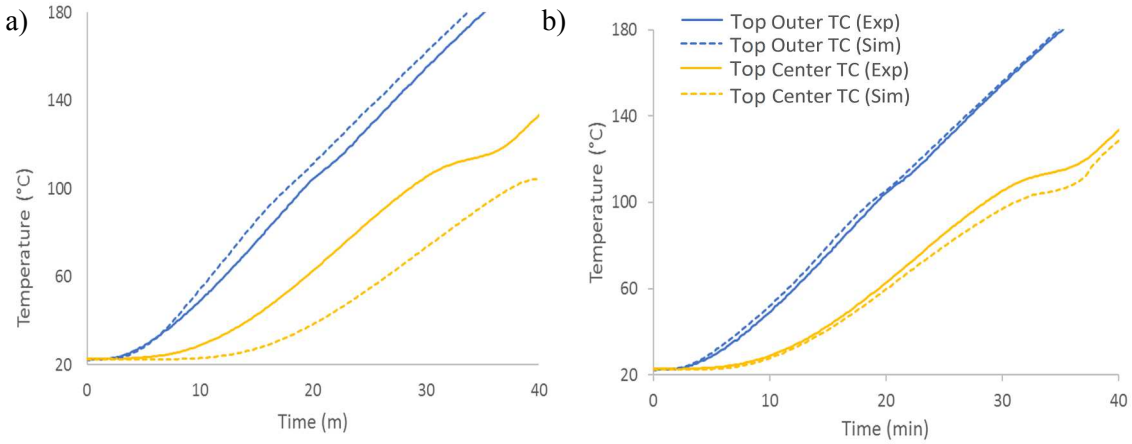

Figure 28. Comparison of outer and inner TCs provides information about thermal conductivity. (a) A trial no-fin charging simulation with the thermal conductivity of the solid salts set to 0.7 W/(mK). (b) The finalized no-fin charging simulation with thermal conductivity ranging from 1.65-0.5 between 20-239 °C. In (a), the internal TC heats up too slowly, prompting an increase in later simulations.

study from 1968 [1]; most recent work suggests a value between 1475 and 1550 J/(kgK) [1, 72, 106, 111], which amounts to an uncertainty closer to +/- 2.5%. The assumed value of 1520 J/(kgK) lies between the range suggested for the relevant temperatures by two recent review papers: 1484-1494 J/(kgK) in Serrano et al. [106] and 1547-1549 J/(kgK) in Bauer et al. [1].

The remaining thermal properties were determined through a structured trial-and-error process. The first step, described above, is to define the flux at the top and bottom boundaries. This step is performed first because the slopes of the temperature data in periods of stability (i.e. when there is no change in latent heat storage and heat input is constant) tend to be consistent across all TCs even when thermal conductivity is inaccurate; since determining the flux depends on these slopes, this consistency allows for the refinement of flux even when thermal conductivity and phase change properties are uncertain. Next, the thermal conductivity of the salts, particularly in the solid phase, is resolved. Figure 28 shows how comparisons between the temperature data at internal and near-aluminum TCs during periods of stability provide evidence of solid-state thermal conductivity. The thermal conductivity of the liquid salts, however, is difficult to determine from the simulations, since its effects are obscured by convective flows and the phase change process. However, most sources suggest a value for the relevant temperature

range between 0.45-0.52 W/mK [1, 72, 106, 111]; the value assumed in these simulations is 0.5 W/mK. Third, the latent heats of transformation are determined by comparing the length of time required to complete the transformation (either solid-solid or liquid-liquid) when the overall flux into the container is accurate (see Figure 29). Finally, Figure 31 and Figure 30 demonstrate how the time-derivative of temperature plots are used to estimate

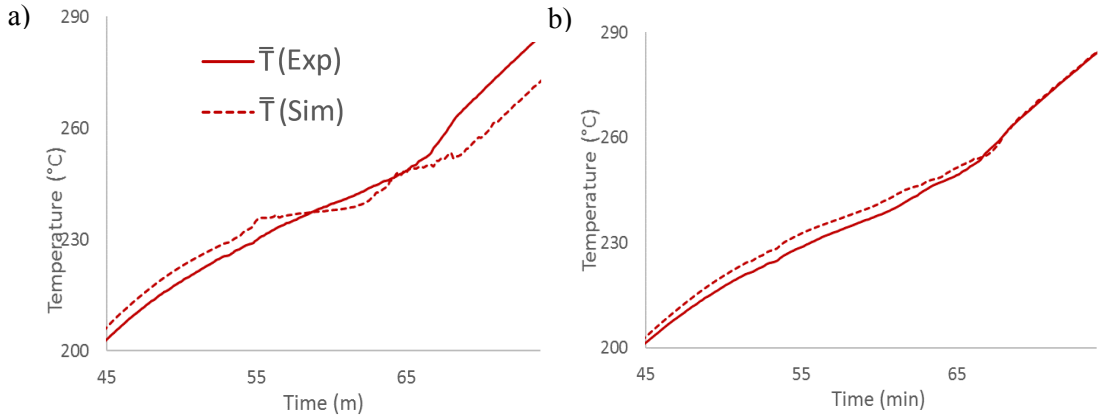

Figure 29. If the slopes of temperature change before and after melt indicate that the overall energy flux is accurate, the time length of the melting process provides information about the latent heat of transformation. (a) Trial finned charging simulation with LS_{trans}= 118 kJ/kg. (b) Final finned charging simulation (LS_{trans} = 85 kJ/kg). The long melting period in (a) suggests that the latent heat value is too high.

the solidus and liquidus temperatures: in these cases, changes in the derivative indicate shifts within the phase change process. It should be noted that this process is iterative: the steps outlined here are presented roughly in the order in which they are performed, but the interaction between these properties requires revisiting earlier steps in the process to ensure the overall accuracy of the simulations.

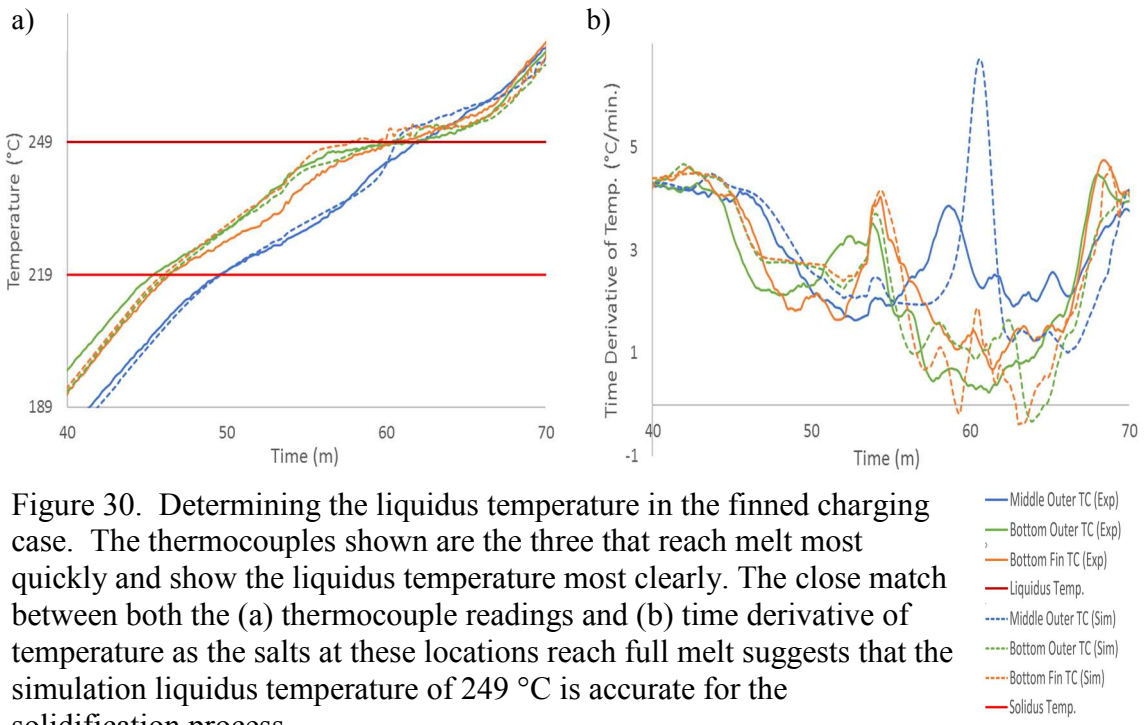

Figure 30. Determining the liquidus temperature in the finned charging case. The thermocouples shown are the three that reach melt most quickly and show the liquidus temperature most clearly. The close match between both the (a) thermocouple readings and (b) time derivative of temperature as the salts at these locations reach full melt suggests that the simulation liquidus temperature of 249 °C is accurate for the solidification process.

The refinement process produces several results that are relevant to researchers interested in using solar salts and other PCMs in latent heat storage devises. First, the latent heat of solidification used in the final simulations is considerably lower than those found in the literature: the value of 85 kJ/kg is about 17% lower than the lowest value in the literature [2]. Second, the thermal conductivity of the salts in their solid phase, which is not investigated significantly in the literature [1], is significantly higher than values that have been reported. Bauer et al. claim that $NaNO_3$ has a thermal conductivity of 1.0 W/(mK) at 100° C [126], but a connected group of researchers later suggest that a eutectic mixture of KNO_3 and $NaNO_3$ (54%/46% by weight) has a solid conductivity value of approximately 0.38 W/(mK) [2]. Iverson et al. suggest that the thermal conductivity of solid solar salt is about 0.76 W/(mK). The present work, however, finds that simulations are most accurate when thermal conductivity values range linearly from 1.65-0.58 W/(mK)

between 20-200 °C and from 0.58-0.50 W/(mK) between the solidus and liquidus temperatures.

Finally, the phase change temperature boundaries used in the final simulations vary from previously reported values. While the solidus value of 219 °C matches the literature and is consistent in both melting and solidification, liquidus temperature results show clear signs of hysteresis. Figure 31 demonstrates that in discharging simulations, 239 °C leads to accurate simulation results; this is consistent with results found in the literature [3]. However, Figure 30 shows that in charging simulations, a value of 249 °C is necessary to produce accurate simulations. The authors know of no previous research that finds these values to be different for melting and solidification. Similar results pertain in the solid-solid transformation: there is nearly a 20 °C difference between the transformation temperature range for charging versus discharging. Ibrahim ElSaeedy et al. [4] do report the effects of hysteresis in their investigation of the solid-solid transformation, but only with regard to different heating rates rather than in the difference between heating and cooling; in addition, the hysteric effects on the temperature range of transformation which

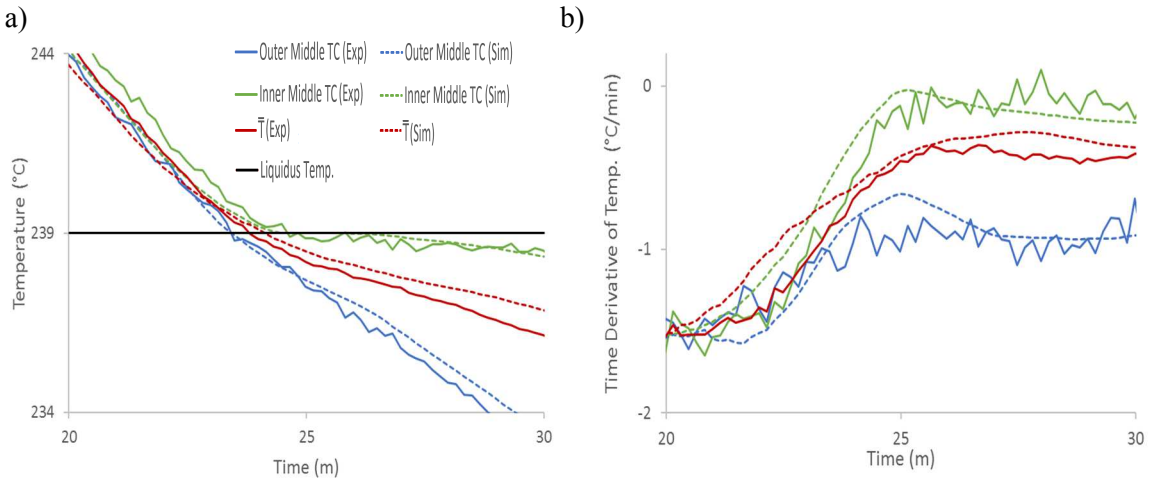

Figure 31. Melting temperature analysis in final discharging no-fin simulation. The close match between both the (a) thermocouple readings and (b) time derivative of temperature at the start of solidification suggests that the simulation liquidus temperature of 239 °C is accurate for the solidification process.

they report are much smaller than those shown here. The final thermal properties used in the simulations are shown in Table 9.

The material parameter values specified above produce the best agreement between experiments and simulations. However, a limitation in the current method is the use of a constant specific heat and constant density, despite evidence of significant differences in these characteristics between the solid and liquid phases [2, 71, 103]; the phase dependencies of these properties are neglected in this work. As noted above, this weakness is tempered by the relative small phase dependency of $\frac{1}{\rho C_p}$, but these and other computational simplifications mean that these thermal property assessments must be seen only as estimates that apply to the specific sample of solar salts that were used in the current experiments. However, the significant differences between the findings here and the properties as reported in the literature are worthy of notice, for researchers interested in both solar salts and PCMs more generally. On the one hand, the low latent heat of transformation found in the current effort to match experiments is a significant concern for the design of LHTSDs using solar salts, and the hysteresis in the liquidus temperature could have a noticeable effect on design optimization of such LHTSDs. More broadly, the current findings suggest that the design of LHTSD systems, particularly when guided by numerical simulations, must take into account the variability of PCM thermal properties, whether caused by natural sample-to-sample variability, degradation, hysteresis, or other factors [112].

3.3.2 Validation of the Simulations

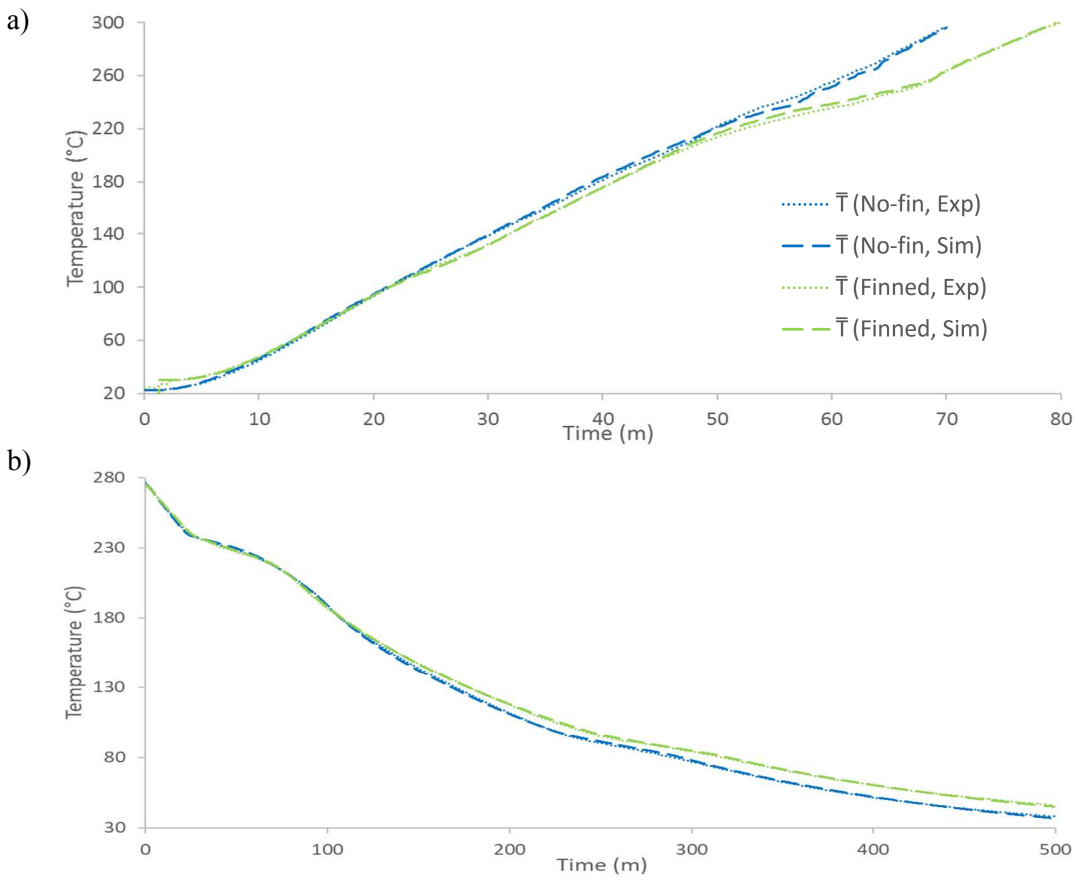

Figure 32. $\bar{T}$ during (a) charging and (b) discharging. $\bar{T}$ is used to compare the estimated overall energy within the salts for the experimental and numerical results. Note that for the finned case, the domain is larger and T_0 is higher than in the no-fin case: the finned and no-fin cases are not directly comparable in this plot.

Calculation of $\bar{T}$ enables a comparison of the average temperature within the salts for the experimental and numerical results. This quantity is used to test the accuracy of calculations of the overall energy transport within the chambers over the course of the simulations. Figure 32 shows that the four simulations accurately reproduce the experimental results.

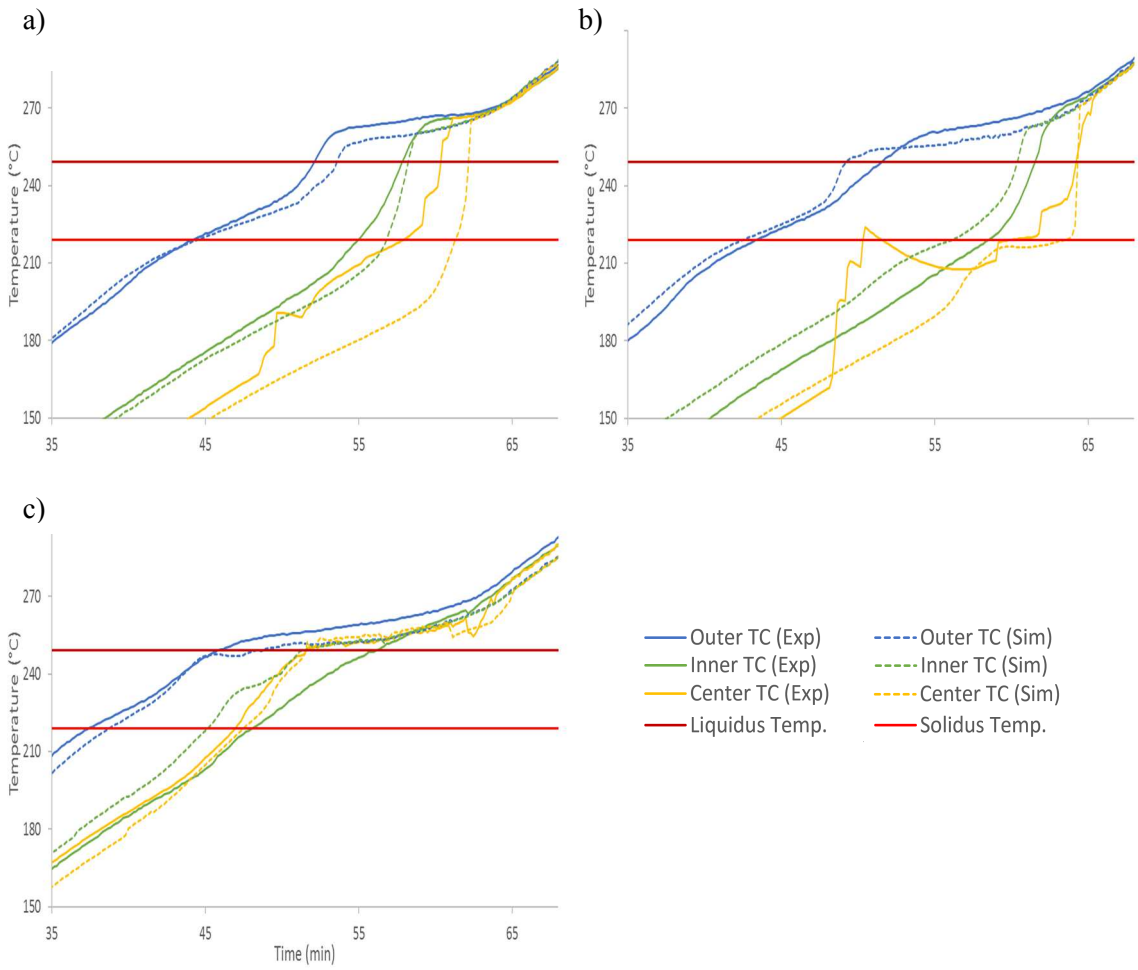

Figure 33. TC readings in the no-fin case during charging. (a) Top vertical position. (b) Middle vertical position. (c) Bottom vertical position.

The individual TC readings shown in Figure 33, Figure 34 and Figure 35 that the temperature fields in the simulations accurately reproduce those in the experiments. There are some small but notable differences between the experimental and simulation results. First, Figure 34 shows that the aluminum core temperatures in the finned charging simulation are higher (5-15 °C) than those in the experiment. Unlike the salt TCs, which

are directly submerged in the salt, the experimental TCs within the aluminum are in a narrow hollow cylinder within the core. Therefore, since the salt temperature readings are generally accurate, it seems likely that the experimental thermocouple readings could be artificially low. The presence of air below the TC and possible imperfect contact between the TC and the aluminum could lead to temperature readings that are below the actual aluminum temperature in the core.

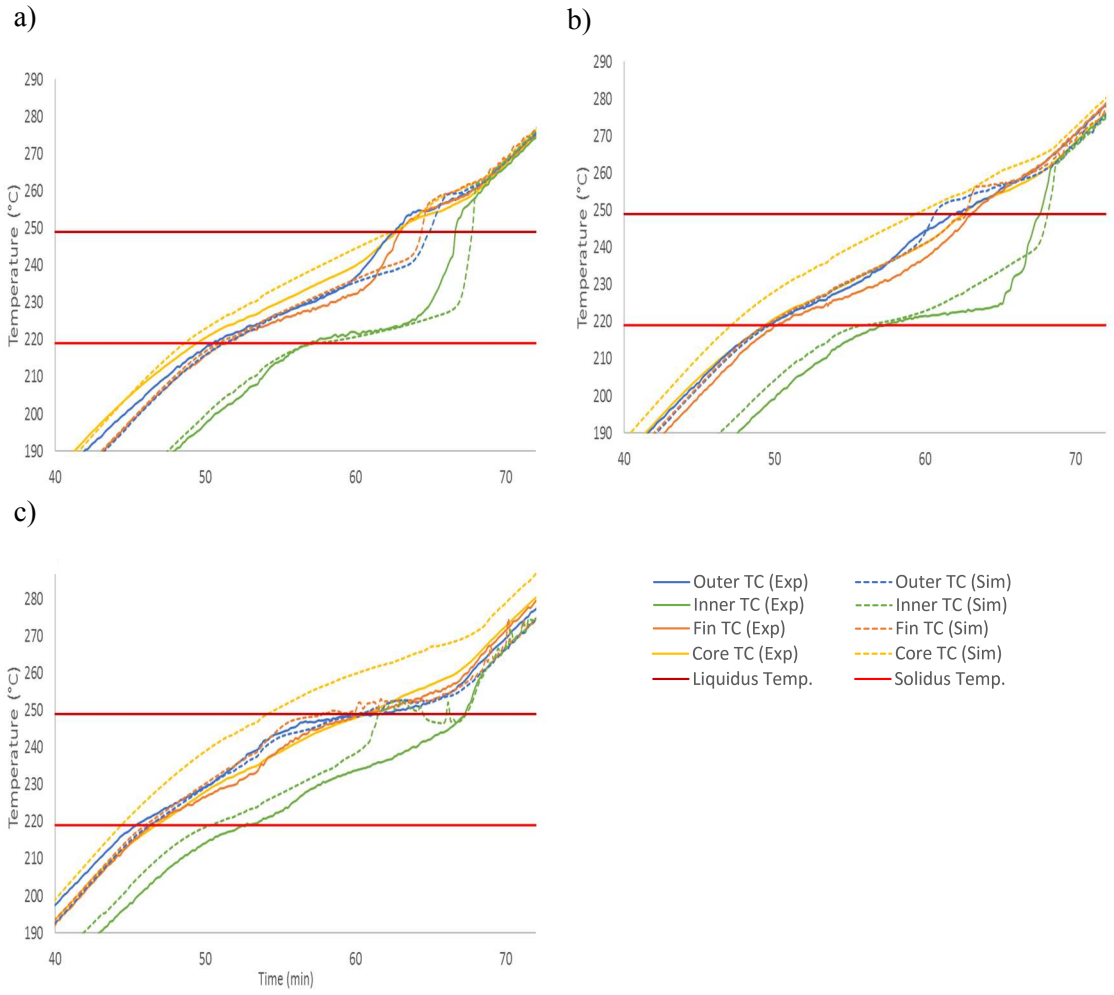

Figure 34. TC readings in the finned case during charging. (a) Top vertical position. (b) Middle vertical position. (c) Bottom vertical position.

The second difference between experimental and simulation TC readings results from the fact that the temperature field in the charging cases can be influenced by the intermittent formation of plumes from the heated bottom of the chamber. These plumes can lead to significant differences between the experimental and simulation results. This is most obvious in the no-fin case. In the most dramatic example, Figure 33(b) shows a sudden rise in temperature of the center TC at the middle position in the experiment at approximately the 48-minute mark. The simulation TC shows a smaller but similar rise at the 57-minute mark. These sudden rises in temperature of unmelted salts are evidence of the formation of a plume directly below the TC: as the melt boundary approaches the TC,

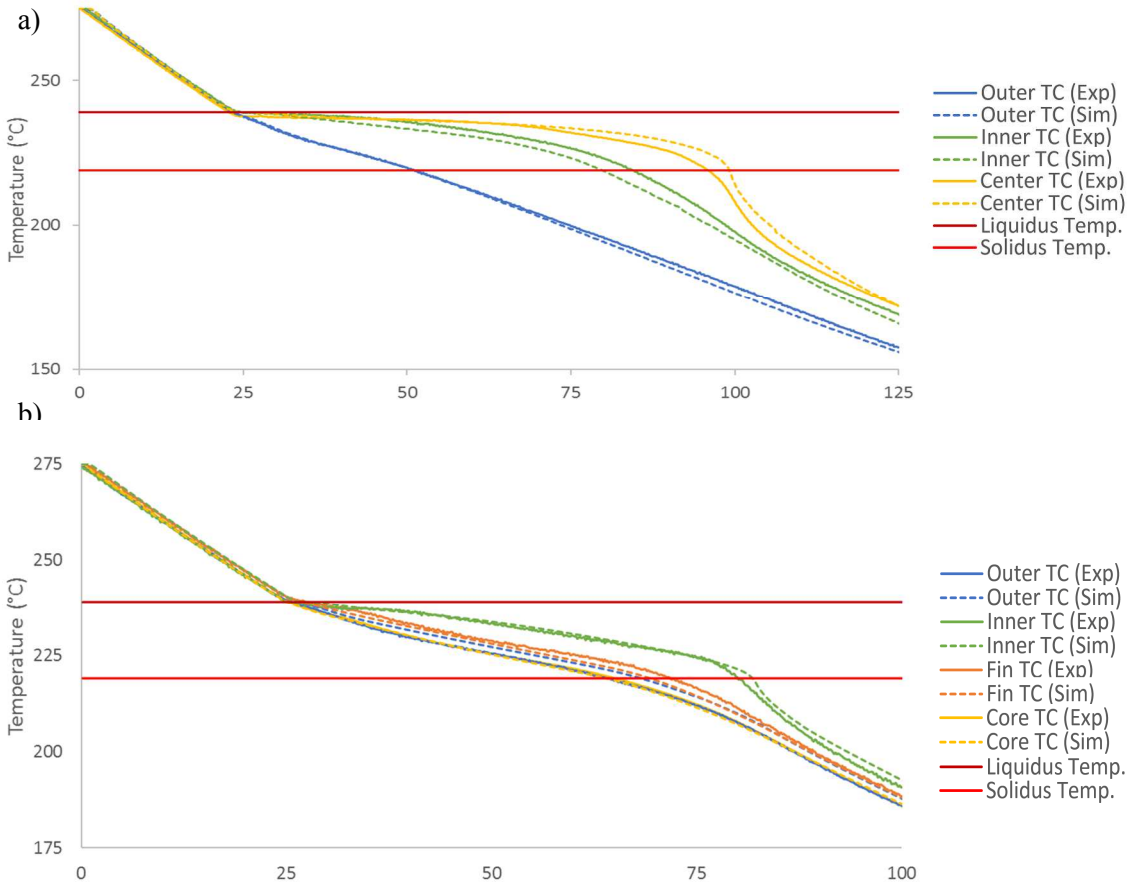

Figure 35. TC readings from the middle position during discharging in the (a) no-fin and (b) finned cases. Results at the top and bottom positions are similar.

its temperature rises quickly. Figure 38(d)- Figure 38(f) illustrate why these rises are difficult to predict: at this point in the melt development, plumes forming on the bottom surface create a significantly asymmetric melt boundary. Therefore, the axial position of the TC is important in determining whether and when a sudden rise occurs. As a result, a simulation TC is unlikely to capture the same sudden rise that the experimental TC does. However, the general melt pattern created by these plumes is duplicated in the simulations, and as Figure 33(b) illustrates, the final rise of the center TC to full melt temperatures occurs at nearly the same time. It is worth noting that these plumes have a less significant effect in the finned case: as will be discussed below, the smaller chambers within the finned case lead to less dramatic plumes (see Figure 37) and no significant sudden rises in the temperature of TCs occur within the unmelted salts (see Figure 34).

Despite these small differences between the experimental and simulation TC readings, Figure 33 through Figure 35 show that the simulations provide an accurate representation of the temperature, melt, and flow patterns within the experimental chambers.

3.3.3 Analysis of Melt and Flow Behavior during Charging

The development of the melt boundary during charging is illustrated in Figure 37 (for the no-fin case) and Figure 38 (for the finned case). Analysis of these figures suggests that there are four stages to the melting process, each influenced by the geometry of the chamber (i.e. with and without fins):

1) Thin layer melting. During this stage, conductive heating melts a thin layer of salts next to the aluminum; convective heating is minimal, as the flow is restricted by the still solid salts as well as the narrow melted volumes. It is interesting to note that this stage lasts significantly longer in the finned case than in the no-fin case. From the point of initial melting, it takes approximately 8 minutes before any significant plumes develop on the bottom surface for the finned case; for the no-fin

case, plumes form in less than 5 minutes. Figure 37(b) shows that in the finned case, salts are melted almost three-quarters of the way up the outer wall before any plumes form at the base of the chamber. In contrast, Figure 38(a) illustrates that developed plumes in the no-fin case are visible even before the salts are melted one-third of the way up the outer wall. In short, the higher mass of aluminum in the finned case more effectively spreads heat energy to salt throughout the chamber, while the concentration of heat in the bottom of the no-fin case leads to an earlier development of convective flow.

2) Bottom-dominated melting. This stage features the formation of plumes in the bottom of the chamber and marks the beginning of the dominance of convective heat transfer in the salts. This stage is more important in the no-fin case than the finned case. In the no-fin case, the bottom plate is open enough that regularly spaced plumes, reminiscent of Rayleigh-Bénard convection cells, develop across the bottom surface. These distinct cells survive for nearly nine minutes, as shown in Figure 38(a)-(e), before the cells begin to lose their symmetry and merge together. In the finned case, this stage is much less recognizable: Figure 37(b) shows the incipient formation of several distinct cells, but within two minutes (Figure 37(c)) these have been fused into several asymmetric plumes. The tighter space at the base of the finned case does not allow a regular pattern of plumes.

3) Side-dominated melting. During this stage, the convective flows developed in the previous stage strengthen and begin to move up the sides of the chamber. Because the finned chamber has already melted a significant volume of salts along its vertical sides in the first two stages, this stage occurs very quickly in the finned case. Figure 37(c)-(e) show the formation of thick plumes along these vertical sides: the conductive heating of the first stage has primed the chamber for the strong

vertical flows visible here, and the cooling downward flows prevent further melting in the center of the bottom section of the container. In contrast, the bottom and sides of the no-fin case grow simultaneously, as shown in Figure 38(d)-(g). The result of this difference is that while convective flows are slower to start in the finned case, the finned case develops stronger vertical convection patterns than the no-fin case.

4) Top-dominated melting. This stage results from the maturation of the convection patterns that originate at the side-walls: the strong flow of hot salts along the vertical surfaces of the containers leads to significant heat transport into the top section of the container. As a result, the final core of unmelted salts melts from the top down, despite the heat flux from the bottom of the container. In fact, in both cases there is a cooling of the lower section of the chamber due to the downward flow of salts along the (relatively cool) melt boundary: this is visible in the movement from Figure 37(f) to (g) and from Figure 38(g) to (h). Though counter-intuitive, this cooling is also visible in the experimental data: Figure 33(c), for example, shows the significant dips in the experimental and simulation temperature at the bottom center TC of the no-fin case at approximately the 62-minute mark, and Figure 34(c) demonstrates that this phenomenon occurs at the inner TC of the finned case at about the 65-minute mark as well. Unlike earlier stages, both the finned and no-fin case move through this stage in a similar manner. As Figure 37(g) and Figure 38(h) and (i) show, once the side-dominated stage has matured in each case, the melt boundary begins to move down into the remaining unmelted core. In both cases, the last remaining unmelted salt is about one-third of the way up from the bottom of the container.

Although both cases move through these four stages, it is difficult to directly compare the effectiveness of the two designs: the finned and no-fin domains contain the same mass of solar salts, but the finned chamber contains more aluminum and so has a taller computational domain. Still, the finned design clearly leads to more effective melting: despite the higher mass of aluminum in the finned domain and the same influx of heat from the bottom, the time from the first melted salts to full melt is five minutes shorter in the finned case (23 minutes) than in the no-fin case (28 minutes). The key difference is that the finned design moves quickly through the second stage (bottom-dominated) into the third stage (side-dominated). The most powerful mechanisms for heat transport are the strong vertical convection cells that develop once the layer of melted salts along the vertical surfaces is thick enough to develop significant flow. This is an important point for latent heat LHTSD design optimization: the optimal fin design is the one that can encourage the formation of the strong convection flow of the side-dominated stage as quickly as possible. As noted above, once the side-dominated heat transport is fully established, the design of the fins seems to have a less significant effect on flow and melt development.

3.3.4 Analysis of Melt and Flow Behavior during Discharging

The development of the melt boundary during discharging is illustrated in Figure 39 (for the no-fin case) and Figure 40 (for the finned case). In general, the discharging process is less complex than the charging process. Even before the salts begin the solidify, the maximum velocity magnitudes in discharging are an order of magnitude lower than those in the charging simulations; as a result, conduction dominates the heat transfer during discharging, especially after a layer of solidified salts has formed on the internal aluminum surfaces. Figure 39 and Figure 40 show that the phase boundary develops in similar ways in both the finned and no-fin cases. Figure 39(b) and Figure 40(b) show that as heat is transferred both out of the top and through the bottom of the domain, the aluminum cools and begins to solidify the salts in its vicinity. Buoyancy leads to small convection flows

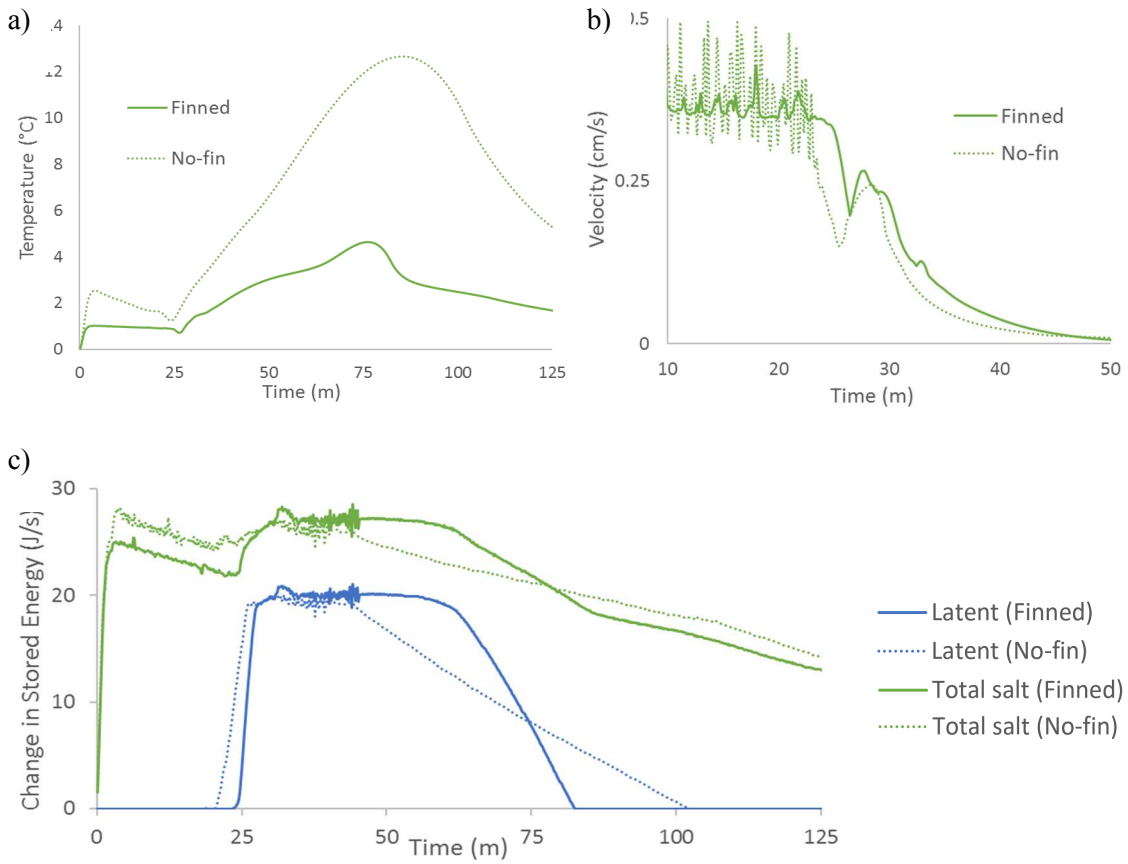

Figure 36. (a) Standard deviation of temperature inside the salts during discharging. (b) Maximum velocity magnitude within salts during discharging. (c) Change of stored latent and total (latent and sensible) in the salts during solidification. This plot shows the capability of the designs to transfer energy out of the salts during the discharging process.

that move warmer fluid into the top section of the chamber: this produces an oblong unmelted core in both simulations (Figure 39(d) and Figure 40(d)). Relatedly, Figure 39(f) and Figure 40(e) illustrate that the last remaining unmelted section in both cases is in the center of salt chamber about two-thirds of the way up the domain.

The different configurations in the two chambers makes a direct comparison of the effectiveness of the designs challenging. But as in the case of charging, the finned geometry is significantly more efficient in the discharging phase as well. As in charging, the length of time required to complete the phase change is much shorter in the finned case;

the no-fin simulation requires 71 minutes to move from initial solidification of salts (1% solidified) to full solidification (99% solidified), while the finned case needs only 51 minutes. In addition, as Figure 36(a) demonstrates, the spread of temperatures within the finned simulation is smaller than within the no-fin simulation: because the maximum distance between an aluminum surface and any particle of salt is much smaller in the finned container, the conduction-dominated heat transfer more effectively lowers the temperature of the salts throughout the chamber. Finally, Figure 36(c) shows that the finned case is more efficient at moving both latent and sensible energy out of the salts. This is particularly true after velocities within the salts are nearly zero (after the 45-minute mark in both cases, as shown in Figure 36(b)): while flux out of the salts declines precipitously for the no-fin simulation at this point, the flux in the finned case does not drop significantly for another 15 minutes. As conductive heat transfer becomes dominant, the performance of the finned case is clearly superior.

These results are not surprising. But they do highlight a chief difficulty of the heat extraction process for a LHTSD. Figure 36(c) demonstrates that early in the solidification process (i.e. before approximately the 40-minute mark), the finned and no-fin cases are similarly efficient at transferring heat out of the salts. But as Figure 39(b) and Figure 40(b) show, early in the solidification process a layer of solidified salt forms on the inner surface of the aluminum. As this layer thickens, it acts as an insulating layer, keeping the internal salts melted and restricting the transfer of heat from the salts into the aluminum. Convection becomes weak and the spread of temperatures within the salts grows higher in both cases (see Figure 36(a)). For the no-fin case, this leads to a sudden drop in the rate of energy transfer from the salts. But the smaller salt sub-volumes of the finned case reduce the insulative effects of the layer of solid salts: because no particle of salt is far removed from an aluminum surface, the maximum thickness of the layer between an aluminum surface and any particle of liquid salts is thinner than in the no-fin case. The importance

of fins in enhancing heat transfer is most significant when conduction becomes the dominant mode of heat transfer.

This work agrees with earlier work [17, 32, 93-101] in concluding that fins are an effective strategy for the enhancement of heat transfer within LHTSDs. However, it qualifies that conclusion by noting that the flow and melt boundary develop in similar ways in both cases despite the significant differences in geometry. This qualification means that the effectiveness of fins is more noticeable in conduction-dominated situations, and suggests that the flow and melt development during discharge described in this section is consistent across a wide range of LHTSD geometries.

3.4 Conclusion

This chapter investigates the melting and solidification of a LHTSD using solar salts as the PCM and aluminum fins as the heat transfer enhancement mechanism. A series of physical experiments are performed to determine the temperature field as the container is heated from T_0 to approximately 300 °C and then allowed to cool again. Temperature measurements are taken at 24 locations, including 9 symmetrically distinct positions for the no-fin case and 12 symmetrically distinct locations for the finned case. The numerical simulations are designed to mimic the experiments, in part by identifying through trial-and-error the material thermal properties that lead to the most accurate simulations. The accuracy of the final simulations, which include a charging and discharging simulation for the no-fin and finned case, are assessed by comparing the experimental TC measurements to the computed temperature field. Once this accuracy is established, the detailed simulation information and images are analyzed to describe the flow and melt behavior of solar salts within the no-fin and finned LHTSDs. The final simulations provide an accurate and reliable representation of the transfer of energy throughout the container during

melting and solidification. This accuracy allows us to use the simulations to provide three main insights into the behavior of the salts.

The first of these concerns the thermal properties of solar salt. The current experimental literature on the thermal characteristics of solar salts indicates significant uncertainty about the thermal conductivity, liquidus temperature, and latent heat of transformation. This uncertainty—which is not atypical of mixed material PCMs—has multiple causes, including hysteresis, material degradation, and uneven mixtures in resolidified salts. The results in these simulations are notable because they confirm that the thermal properties of solar salts in practical situations can be difficult to predict. For instance, the latent heat of transformation value used here is over 15% lower than the lowest value in the current literature. The thermal properties used here are clearly not established systematically enough to replace current material assumptions about solar salts. However, the present work suggests that researchers interested in mixed material PCMs, especially solar salts, need to carefully consider the values of mixture thermal properties.

The remaining insights concern the flow and melt behavior of the solar salts. First, comparing the two simulations during melting illustrates the flow development moving through four stages: thin layer melting, bottom-dominated melting, side-dominated melting, and top-dominated melting. Both the no-fin and finned simulations progress through these four stages. The superior melting efficiency of the finned case, however, can be explained by the differences in transition between stages. The thin layer melting stage for the finned case lasts significantly longer: the fins transfer energy to the aluminum surface areas throughout the domain, while in the no-fin case, this energy remains concentrated in the bottom of the chamber. As a result, the finned simulation moves quickly through the second stage (bottom-dominated) into the third stage (side-dominated), which is the most effective mechanism for melting large quantities of salt rapidly. These results suggest that in designing a LHTSD, a chief concern should be finding means to encourage the strong vertical circulation patterns typical of the side-dominated stage.

Finally, the present experiments and simulations show that the melt and flow behavior during discharge are quite similar in both the no-fin and finned case: in each, modest circulation velocities and temperature gradients lead to an oblong melted section at the center of salt chambers. However, once heat transfer within the LHTSDs becomes dominated by conduction, the finned container becomes much more effective at quickly transferring energy out of the salts. The expected superiority of the finned geometry lies not in its ability to create a more effective convective flow, but in its capacity to continue to transfer heat energy out of the salts even once a layer of solidified salts has covered the interior aluminum surfaces. The smaller distance between the remaining liquid salts and the aluminum surfaces in the finned case means that the insulating effects of the solidified salts do less to slow the transfer of heat from the salts to the aluminum.

This work provides a better understanding of the role of thermal properties, flow patterns, and melting behavior of solar salts during both charging and discharging phases of a LHTSD. In ongoing work, the 3-dimensional computational tool and the insights developed are being used in the design of efficient thermal storage devices using PCMs.

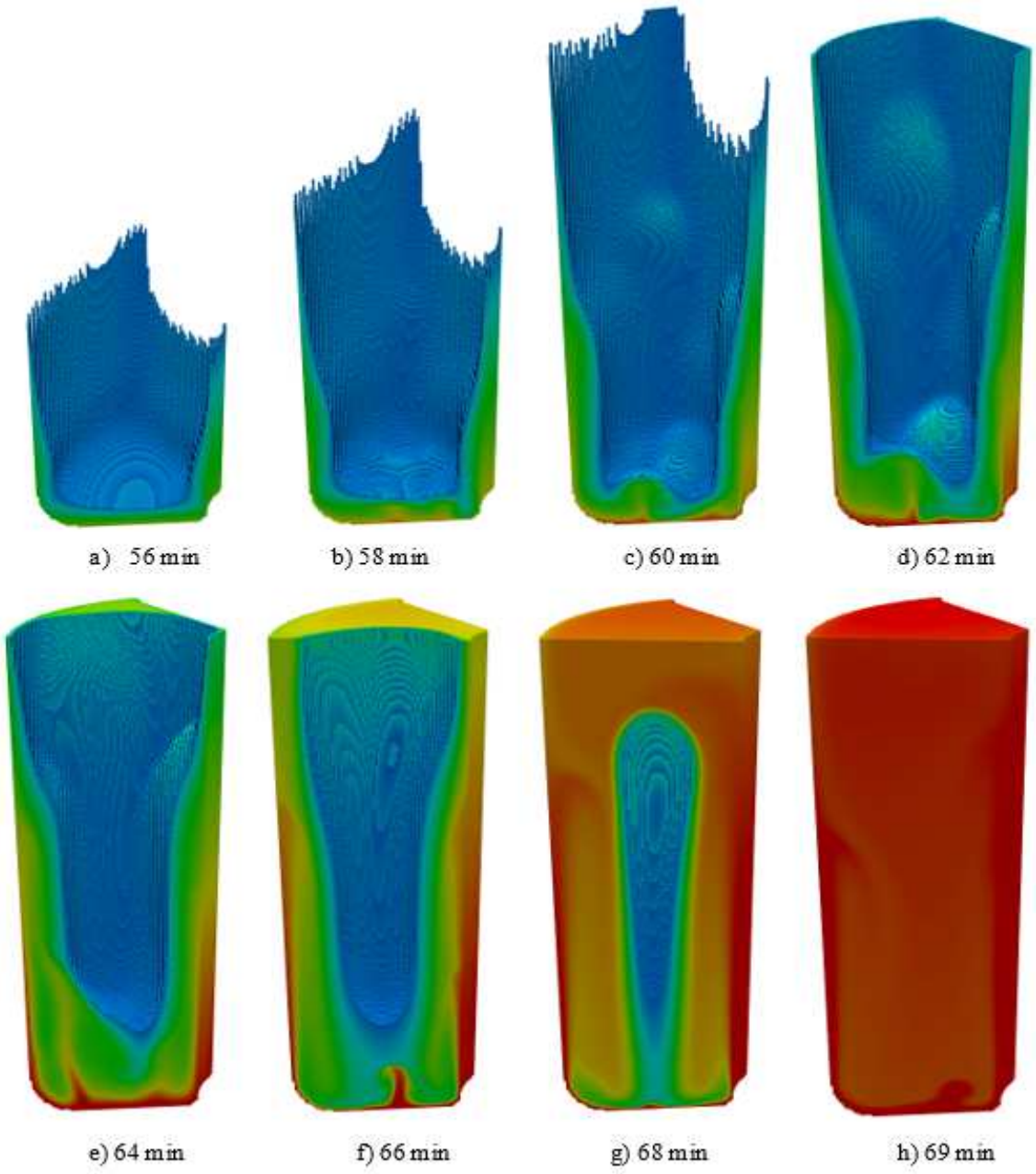

Figure 37. Development of the melt in the finned chamber from 56-69 minutes. The solid image shown is the liquid portion of the salts ($0.8 \leq F_{LS} \leq 1.0$).

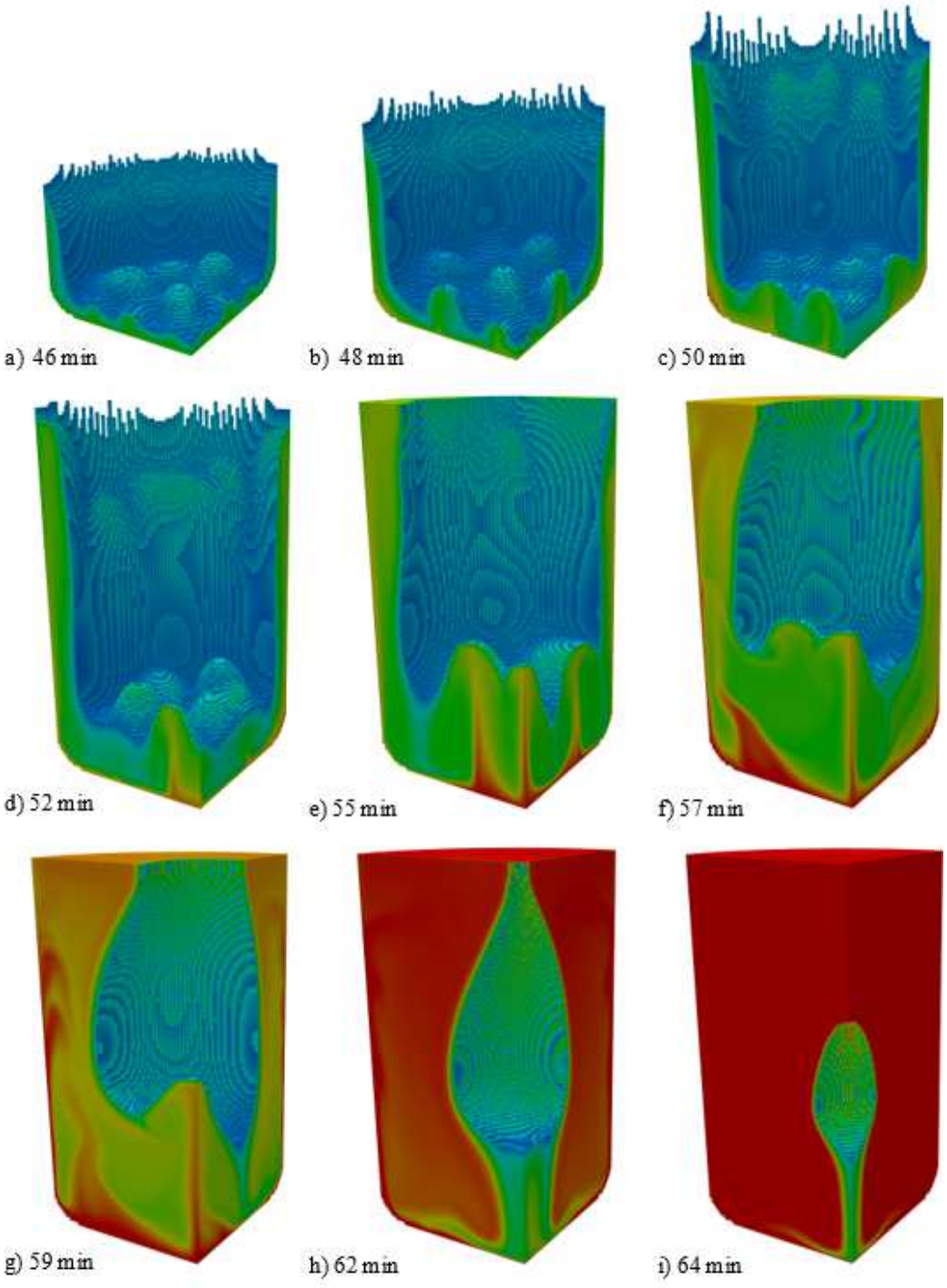

Figure 38. Development of the melt in the no-fin chamber from 53-71 minutes. The solid image shown is the liquid portion of the salts ($0.8 \leq F_{LS} \leq 1.0$). Notice that the domain is shorter in the no-fin case: the volume of salt is consistent between the two cases, but the lack of core and fins leads to a shorter domain space.

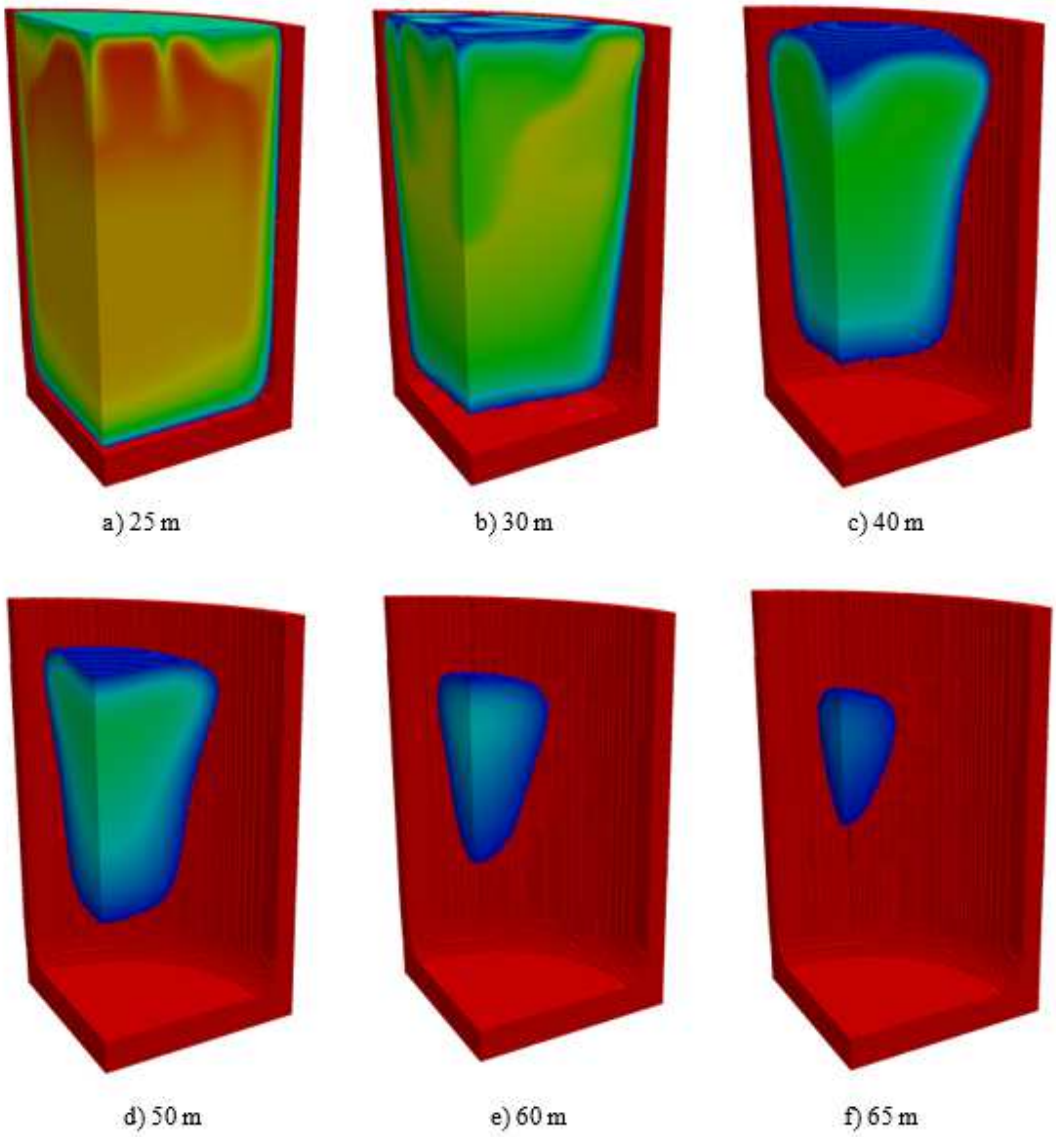

Figure 39. Solidification in the no-fin chamber from 25-65 minutes. The solid image shown is the liquid portion of the salts ($0.8 \leq F_{LS} \leq 1.0$) surrounding the aluminum container (in red).

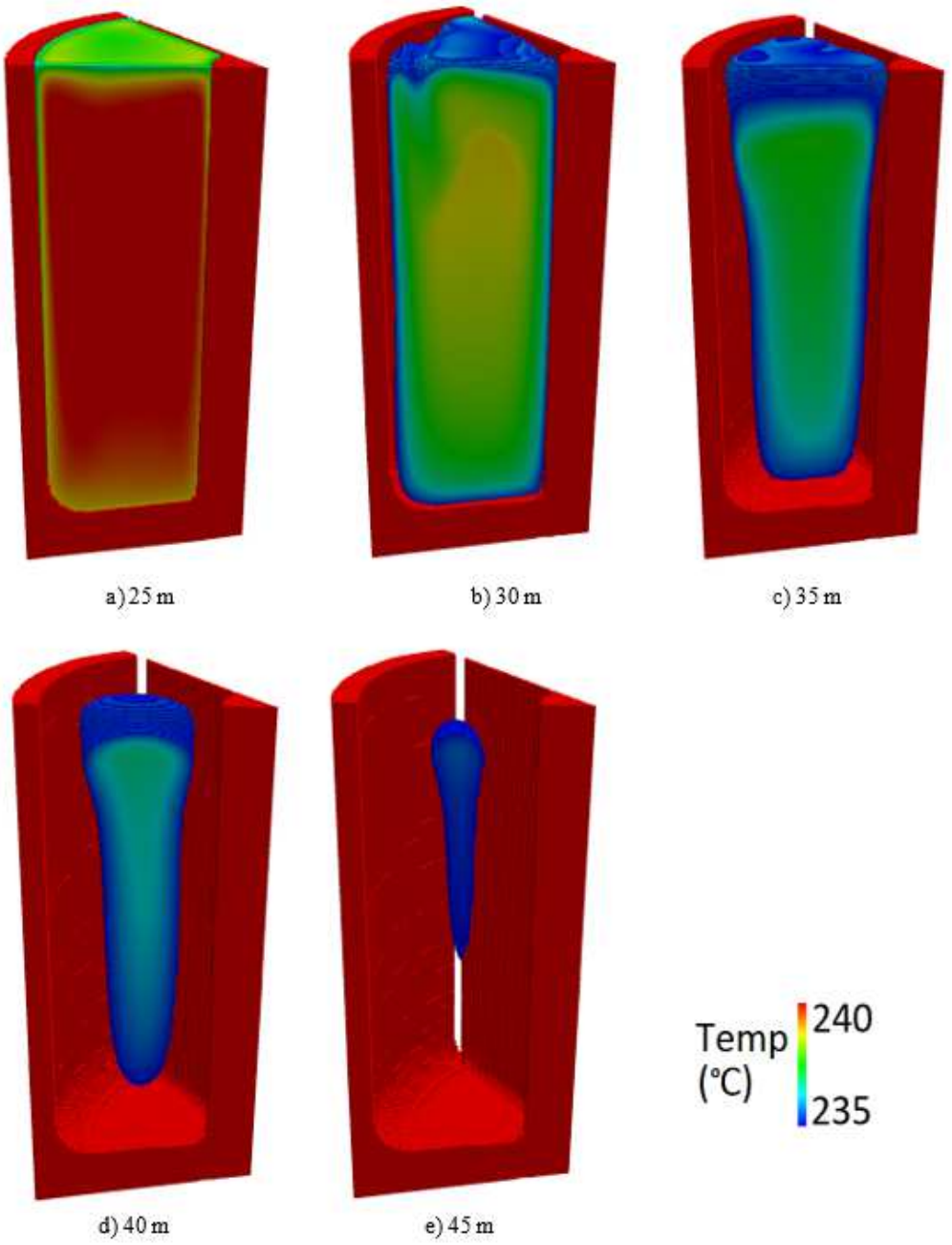

Figure 40. Solidification in the finned chamber from 25-45 minutes. The solid image shown is the liquid portion of the salts ($0.8 \leq F_{LS} \leq 1.0$) surrounding by the aluminum container, core, and fin (in red).

CHAPTER FOUR
OPTIMIZATION OF SMALL-SCALE FINNED LHTSD

As noted above, a key challenge in the development of a practical thermal storage device (TSD) is the low thermal conductivity of common phase change materials (PCM). This low conductivity impedes both heat input and extraction. The most common solution is to use conductive metal fins to spread heat through the device. However, optimizing the effectiveness of the container and the fin arrangement is difficult due to the large number of potential design parameters. This paper develops a strategy to make simulation-based optimization process affordable and accurate. First, numerical techniques are designed to accurately and efficiently compute heat and mass transport in a variety of geometries without generating grids to conform to each geometry. This facilitates rapid prototyping and mitigates the expense of individual simulations. Second, a pre-screening process identifies the independent variables with the largest and most nonlinear effect on the objective function in the optimization process, thus narrowing the parameter space. Finally, a dynamic Kriging-based optimization approach constructs a multidimensional response surface using sparse input datasets; a machine-learning process determines the the infill points necessary to achieve maximum accuracy with the fewest number of simulations. The response surface is then used to identify an optimal design. The combination of the above three strategies is shown to result in an approach that can aid in the design of optimal thermal storage devices that rely on a mixture of PCM and metal fins.

4.1 Introduction

This chapter aims to use numerical simulation to optimize the design for a bottom-heated LHTSD that uses a metal fin arrangement to spread heat to a low

conductivity PCM. Previous computational and experimental work on finned heat spreaders demonstrates that they consistently enhance heat transfer within a variety of types of LHTSDs [94]. However, identifying the optimal design for these devices is complicated. The main challenge is the vast number of potential designs for such a device: even the simplest designs have multiple independent parameters, such as the number of fins, fin thickness, fin height, distance between fins and the angle between fins. Each independent variable exponentially increases the number of design points needed to cover the parameter space. On the one hand, in the past decade, some researchers have developed correlation equations using non-dimensional parameters to predict the behavior of LHTSDs at design points other than the tested design points [35, 127]. But for the most part, much of the work done with thermal storage devices has been restricted to the study of the effect of one or two fin parameters on the efficiency of heat storage or discharge [128-131].

In recent years, however, researchers using numerical simulations have employed more sophisticated optimization tools to explore larger parameter spaces for devices that rely on enhanced heat transfer using fins. Sciacovelli et al. [132] optimized tree-shaped fins for a double pipe heat exchanger by using numerical simulations to create a response surface in a 4-dimensional parameter space. Pizzolato et al. [133] identified an optimal fin design for an annular heat exchanger with a topological optimization approach. More recently, Alayil et al. [134] used an artificial neural network to find an optimal melting solution for a finned rectangular LHTSD with four independent parameters. All of these studies employ state-of-the-art optimization tools and a moderate number (30-100) of simulations in order to estimate the effectiveness of heat transfer at untested design points; in doing so, they are able to pinpoint an optimal design over a much wider parameter space than would be possible without such tools.

The present work develops a novel approach to optimization in order to contribute to this emerging work on optimization of finned LHTSDs. To increase the efficiency of the

optimization procedure, we streamline three different parts of the optimization procedure as follows:

1. First, the expense of individual simulations is minimized. The design investigated is a LHTSD which is heated from the bottom and releases its energy through a top outlet plate. It uses a finned aluminum heat spreader to transfer heat into and out of solar salts, a non-eutectic mixture (70%/30%) of $NaNO_3$ and KNO_3 [110]. The complicated geometry of the flow domain, phase changes of solar salts, contact conditions between the salts and Al surfaces, high temperature gradients, and rapid transients make the simulations within this space numerically challenging and computationally expensive. Several tools are used to reduce this cost. First, the flow solver [54, 114, 115] uses a strongly coupled implicit scheme for conjugate heat transfer and a sharp interface method to define the boundary between different materials: this combination of techniques produces a robust and accurate simulation of the phase change and heat transfer phenomena. Second, the combination of a Cartesian grid-based immersed boundary approach [135] and solution-adaptive locally refined meshes [45] eliminates the need to manually generate a mesh for each geometry. This allows for the resolution of fine flow features and interfacial transport while removing a time-consuming and user-intensive intermediate step in conducting flow simulations. When a simulation begins, the algorithm automatically creates a non-boundary conforming mesh based on the geometry input. A more refined Cartesian grid is established near boundaries between materials, while a coarse grid is used in areas removed from boundaries. As the flow develops, the flow solver measures the first and second derivatives of the temperature and velocity fields and refines/coarsens the mesh as necessary [45]; no computational expense is wasted on areas of weak transport, which is especially important in phase change simulations where large portions of the domain can be quiescent.

2. The second measure that increases the efficiency of the optimization process is the use of an elementary effect-based variable screening procedures [136]. Each design of the LHTSD is defined by several (say *d*) independent design variables. For large *d*, the so-called "curse of dimensionality" makes the creation of a *d*-dimensional response surface prohibitively expensive [137]. The present work employs an elementary effect-based screening strategy that identifies independent variables that have a negligible effect on the objective function. In this approach, a small number of simulations are used to determine both the average magnitude and the standard deviation of the elementary effect of each variable; that is, the change in the objective function created by small perturbations in the variable. The variable screening leads to a reduction of the number of independent design parameters while facilitating the identification of the optimal design.
3. The third strategy used to improve the efficiency of the optimization procedure is to create a response surface using a dynamic Kriging (DKG) method [138, 139]. Response surface construction, also called surrogate modeling or metamodeling [140], uses the results of simulations from a finite number of design points to create a response surface that represents the objective function in the spaces between the known (input) design points. The advantage of this approach is that it limits the number of simulations that must be run in order to find the optimal design. Most approaches to response surface optimization, however, require *a priori* assumptions about the nature of the function: the order of the polynomial basis functions, for instance, must be decided upon before the creation of the response surface [137]. The dynamic Kriging (DKG) approach uses machine-learning techniques to improve upon these methods; likelihood estimates test the accuracy of a range of polynomial radial basis functions, so that the final response surface can be built from basis functions that are most appropriate to a given set of data [138, 139]. In addition, it uses estimates of uncertainty to determine the

design points for supplementary infill simulations; this technique maximizes the improvement of the response surface for each additional simulation. The result is a surrogate modeling process that is both efficient and accurate [141].

The chief aim of this chapter is to optimize the design of a practical LHTSD. The numerical and optimization methodology presented in this paper are designed to achieve this efficiently and accurately in order to guide the design of LHTSDs that combine PCMs for latent storage and metal fin structures for heat spreading. Section 2 presents an introduction to the optimization problem, and explains the setup of the simulations. Section 3 provides the governing equations solved and a brief discussion of the computational methods used. Section 4 explains the variable screening process and its results. Finally, Section 5 covers the design process and the results of the optimization procedure, including an analysis of the response surface behavior.

4.2 Simulation Setup

4.2.1 Defining a Practical LHTSD

This paper aims to use numerical simulation to optimize the design for a practical thermal storage device. As noted, the main challenge in this process is the vast number of potential designs for such a LHTSD: it is crucial to reduce the number of possible designs in a simulation based design framework. The first step in limiting the design space involves defining the desired outcome: we must determine, in other words, the characteristics of a practical LHTSD. Identifying these characteristics demarcates the general shape of the parameter space. Only once this space is defined can we begin the process of winnowing it down to an optimal design.

To imagine a truly practical solar cooker, it is necessary to recognize the limitations of currently available options. At first glance, solar cookers seem to offer an ideal solution

to a range of problems in the developing world: deforestation through overharvesting of wood, health problems related to indoor fires, and loss of time in gathering ever scarcer firewood [5-7]. And engineers have done impressive technical work developing a range of efficient and workable solar cookers [8-10]. Unfortunately, these factors have not led to the widespread adoption of solar cooking [11]. The chief cause of this failure is that the existing cookers have required that their users adapt their cooking habits to the needs of the cooker. Cooking methods, available food, and traditional foods in developing areas are often quite particular to that community: many solar cooker designs do not take these particularities into account, and so people have been reluctant to adopt them. In response to this problem, there has been a push to consider a "holistic framework" or "end-user" approach in designing a cooker and evaluating its success [6, 7, 12, 13]. This has led some solar cooker researchers, for instance, to test the effectiveness of their cookers in the context of local food cultures [14, 15].

The aim, therefore, is not just to build a cooker that can cook food effectively, but to build a cooker that can cook food in the ways that people actually cook. To create a cooker that people will use, it is necessary that it adapt readily to established cooking traditions. What does that mean exactly? In broad terms (setting aside inevitable regional variations), an adaptable cooker is one that is usable indoors, that doesn't require constant supervision (adjusting lenses, etc…), that can be used in the evening, that is economical, that can produce high heat, and that can be used in small spaces.

A key necessity for this vision, of course, is a practical and effective thermal storage device. It is not surprising that most people, especially those in areas that might benefit most from solar cooking, traditionally prepare meals indoors and when the sun is not at its peak. Many solar cookers, though, require that cooking take place during the day and in the outdoors. The development of an effective means to store solar heat, even if only through the evening hours, would be a step towards the creation of an attractive, end-user adapted cooker [16].

But the vision also points toward other key design decisions. First, the large reflecting or focusing lenses commonly used for solar cookers are large, unwieldy, and difficult to incorporate into indoor cooking. As a result, the design here utilizes resistance heating using electricity from photovoltaic panels, whose cost has gone down significantly in recent decades [142]. Importantly, this change also allows for the possibility of a bottom heated LHTSD, a design possibility that promises to increase the melting efficiency of the device.

Second, the vision determines how the LHTSD will heat the cooking pot. Some latent-heat solar cookers incorporate the cooking pot into a deep well in center of the thermal storage container. This is an effective design because the closed-in cooking pot collects heat from the melted PCM from the sides of the pot as well as from its bottom [143]. However, the design also severely limits the type of cooking that can be done because of the deep narrow shape of the pot: while such a design is effective for simmering or boiling, it makes frying or sautéing quite difficult. Since the latter high heat methods are crucial for much traditional cooking (which is often done over an open flame), the design used here draws heat out of the device to a plate on top: it cooks by creating a circular "burner" on the top of the LHTSD. This is less efficient than a pot-style LHTSD, but provides far greater cooking flexibility and ease of use.

Finally, while many cooking storage devices designs use PCMs with melting temperatures ranging from 90° to 150° C [70], here we use a non-eutectic combination of 70% $NaNO_3$ and 30% KNO_3 that has a melting range from 223° to 262° C [110]. As the cooker refreezes while it is cooking, the body of the device remains at the melting temperature. If this temperature is too low, the cooker will not be able to perform crucial tasks such as heating oil for frying or even boiling water [143]. The higher melting range of this solar salt mixture means that if the heat is moving efficiently from the salts to the burner, it is not unreasonable to expect a burner temperature at or above 200° C, which would make possible a wide range of cooking.

There are some limitations to this design. First, the use of photovoltaic cells would likely increase the price of the cooker (although a good reflector or lens is not inexpensive either). Just as importantly, the "burner" design must overcome the challenge of pulling heat out of the LHTSD even as the salts begin to freeze on the surface of the aluminum. Both of these limitations suggest that creating a solar cooker large enough for everyday family cooking would be difficult.

These physical limitation lead to a contraction of the goal for the final product. Rather than seeing the cooker as a main source of cooking energy for a household, we imagine it as a supplementary cooking resource (the undependability of solar energy makes this inevitable, in any case). Furthermore, the aim is not to produce a cooker that can be used by the very poor; instead, the purpose is to create a cooker that is convenient and powerful enough to be appealing to the broad middle/ working class population in the developing world. Ultimately, if a solar cooker could achieve a significant level of adoption by this class—and provide them some relief from the stresses created by the cost and undependability of wood, cooking fuels, and electricity—it would be a notable success. In such a case, the hope is that the designs would soon become available to the rural poor, who are most desperately in need of safe, economic cooking energy in the developing world.

4.2.2 LHTSD Geometry and Materials

The basic design for the LHTSD, shown in Figure 41, is a PCM-filled chamber with metal core, fins, and container surrounded by a layer of insulation. The materials used in the container are aluminum, rice husks (as insulation), and a non-eutectic mixture of solar salts ($NaNO_3$ (70%) and KNO_3 (30%)). Non-eutectic solar salts were chosen as the PCM because they are readily available, inexpensive, and have a large melting range (see Table 11), which allows for a long period of relatively stable temperatures during charging and discharging [110]. Aluminum is chosen because of its low cost, high thermal

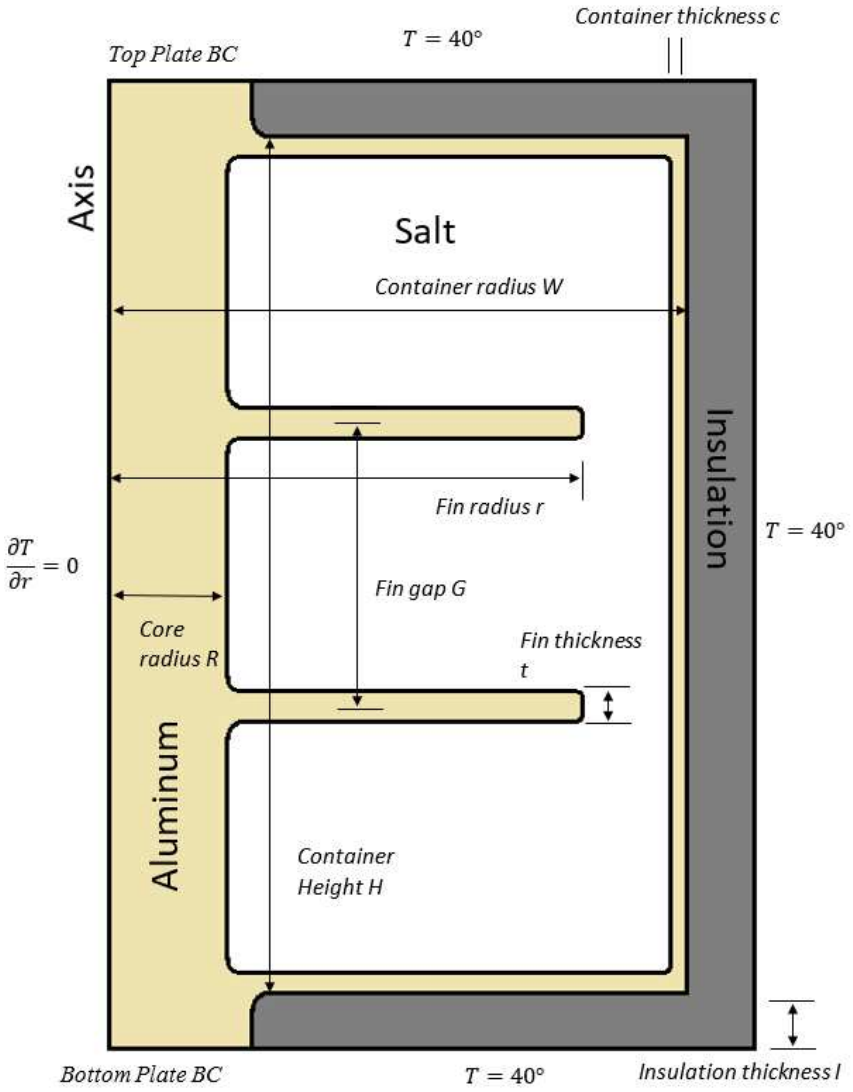

Figure 41. Basic cylindrical (two dimensional axisymmetric) geometry with boundary conditions for LHTSD.

conductivity and heat capacity, and relatively low density leading to a lighter LHTSD. Rice husks have impressive insulating qualities and are inexpensive, particularly in developing countries [75, 76]. The material parameters are listed in Table 11.

The LHTSD is heated from the bottom by concentrating solar energy in the normal diurnal cycle; the stored thermal energy is then retrieved at a discharge plate connected to the top part of the Al core, as shown in Figure 2. One intended use for the device is as a

heat storage device for solar cooking, for which the top plate would serve as a cooking surface, although its basic structure is adaptable to other uses. The shape of both the container and the aluminum core is cylindrical: a rectangular enclosure would create unnecessary asymmetries within the container and problematic corner areas within the salts. One key design decision is whether to include vertical or horizontal fins off the central core. It is not immediately obvious which would be more effective for the charging or discharging process; horizontal fins are used here to allow for two-dimensional axisymmetric simulations. Finally, it is assumed that the fins are all the same size and situated at regular intervals along the core. The resulting basic shape, presented in

Table 11: Material Properties and Simulation Parameters

Solar salts (70% $NaNO_3$: 30% KNO_3)	
Kinematic viscosity (ν)	3.60×10^{-6} m^2/s
Thermal diffusivity (α)	1.68×10^{-7} m^2/s
Latent heat	118.0 kJ/kg
T_{melt}	242.5 °C
ε (melt range)	+/- 19.5 °C
Specific heat (C_p)	1550 J/(kg K)
Density (ρ)	1925 kg/m^3
Thermal conductivity (k)	0.50 W/(m K)
Thermal expansion (β)	0.000325 $°C^{-1}$
Simulation parameters	
$T_{initial}$ (charging)	180.0 °C
$T_{initial}$ (discharging)	320.0 °C

Aluminum	
Thermal diffusivity (α)	6.90×10^{-5} m^2/s
Specific heat (C_p)	893 J/(kg K)
Density (ρ)	2712 kg/m^3
Thermal conductivity (k)	167 W/(m K)
Ground rice husk insulation	
Thermal diffusivity (α)	2.51×10^{-7} m^2/s
Specific heat (C_p)	1682.0 J/(kg K)
Density (ρ)	123.6 kg/m^3
Thermal conductivity (k)	0.0593 W/(m K)

axisymmetric two-dimensional form in Figure 41, depends on eight independent

Table 12: Independent Variables for Container Geometry

ID	Independent Variable	Definition	Dependent Variables Defined	Range of Independent Variable	Base Design Value
SP	Salt Percentage (by Volume)	$\frac{Volume_{salt}}{Volume_{salt+Al}}$	Volume of salt and aluminum	0.5-0.75	0.65
AR	Aspect ratio	$\frac{H}{W}$	Height H and radius W of container	0.5-3.0	2.0
CP	Percentage of Aluminum in Core	$\frac{Volume_{Al\ in\ core}}{Volume_{Al\ in\ container}}$	Volume of aluminum in core and in fins	0.4-0.8	0.6
NF	Number of fins n	n	Volume of aluminum in each fin, fin gap G	3-7	5
FR	Fin radius percentage	$\frac{(r-R)}{(W-R-c)}$	Fin radius r and fin thickness t	0.5-0.9	0.75

parameters: the container height (H) and radius (W), the thickness (t) and radius (r) of the fins, the thickness of the outside container (c), the thickness of the insulation (I), the core radius (R), and the number of fins, which determines the gap (G) between fins.

It is prohibitively expensive to optimize the design in a parameter space spanned by the above eight variables. To restrict the parameter space, three variables are maintained constant before the screening process. Neither container thickness *t* nor insulation thickness *I* are expected to be critical to the fin design, Therefore these are set constant: the container thickness to 14-gauge aluminum sheet metal, and the insulation thickness to a moderate 8 cm thickness. It is also necessary to define the size of the container, so that the optimization process compares equivalent devices. Therefore, the volume of the container

is held constant (which makes *H* dependent on *W*, thus eliminating one more variable). The volume of the PCM is determined by the capacity of the LHTSD to store usable heat, as required by the designer. In the present case, the constant volume of 8165 cm^3 holds approximately 4 MJ of latent and sensible heat energy within 100 degrees of the low end of the melting range (223-323 °C). This temperature range represents the range at which heat could be usefully discharged during solar cooking, although of course this choice does not preclude the use of the LHTSD for other purposes. Following these design decision, five degrees of freedom remain for each individual design —the percentage of salt by volume (SP), the aspect ratio (AR), percentage of aluminum in the core (CP), the number of fins (NF), and a relationship between the fin radius and the container radius (FR). See Table 12 for the definition of each of these); Table 12 also lists the range of these independent variables.

4.2.3 Simulation Procedure, Boundary Conditions, and Objective Functions

For each design, two separate simulations are run. The first simulation tests the charging capability of the design, while the second measures its discharging effectiveness. The discharging simulation has two phases: the storage phase, which is designed to take into account the different heat losses incurred by different designs in the time between charging and discharging, and the active discharge phase.

BCs are defined with two goals in mind. First, they are intended to imitate but not replicate realistic physical conditions. In a physical experiment, the boundary temperature at the inlet or outlet would be a dynamic condition influenced by the type of heat generation, the internal conditions of the LHTSD, contact resistances, and the material being heated, among other factors. For these simulations, however, a complex boundary condition is unnecessary as long as they are generally realistic and allow a trouble-free comparison of different designs: the BCs instituted here aim to simulate a relatively stable

flux that ramps down slowly as the temperatures within the LHTSD go up (charging) or down (discharging).

Second, the BCs must be set up in a way that makes it possible to measure the overall effectiveness of each design. The main purpose of the LHTSD is to provide a significant discharge (i.e. greater than or equal to 500 W) of heat energy while maintaining an outlet temperature above approximately 125 °C, which represents the lowest outlet temperature that could reasonably be expected to boil water. The charging process

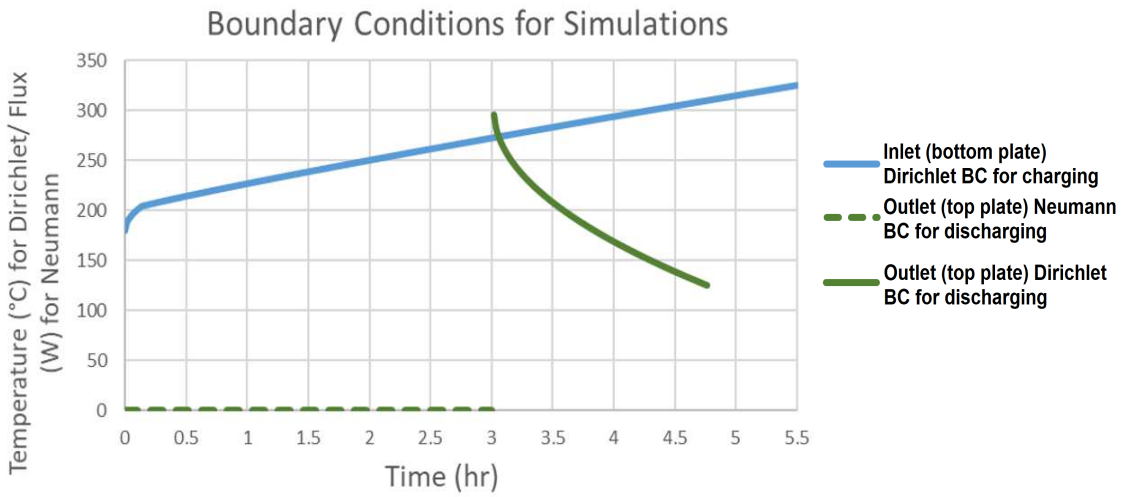

Figure 42. Boundary condition at outlet area for charging (bottom plate) and discharging (top plate) simulations.

complements this central purpose: maximizing heat transfer into the LHTSD during charging (either as latent or sensible heat) increases the ability of the LHTSD to maintain the desired conditions for longer during discharge. As a result, the aim of both charging and discharging simulations is to test the amount of heat energy that a particular design can transfer into and out of the LHTSD while sustaining these conditions. For this reason, a dynamic Dirichlet BC rather than a constant Neumann BC is instituted: this allows overall flux into and out of a design to become an indicator of design fitness. If a design does not

transfer heat effectively into the container during charging, for example, temperatures near the inlet will grow higher, temperature gradients near the boundary will become smaller, and the flux will decrease; similarly, if a design in a solidification simulation cannot transfer heat energy from the edges of the container into the area near the inlet, temperature gradients near the inlet will be small, outflux will be small, and the overall energy in the container will remain high. The boundary condition for the charging simulation begins at 180 °C and gradually ramps up to 325 °C. For discharging, the initial BC is T=300 °C and gradually reduces to 125 °C, at which point useful discharge becomes difficult. The BCs, initial conditions, and other details for both simulations are illustrated in Figure 42 and specified in Table 13. Example plots of the resulting instantaneous flux over time at the inlet and outlet can be seen in Figure 53(b) and Figure 54(a), respectively.

Table 13: Simulation Details

Simulation	Phase	Length (hr)	Initial Condition (°C)	Boundary Conditions (t= time in seconds)			Approximate Outlet/ Inlet Flux Range (W)
				Bottom plate	*Top plate*	*Insulation*	
Charging		5.5	180	$200 + 0.017t^{0.9}$ °C	No flux	40 °C	200-300
Discharging	*Storage*	3	320	No flux	No flux	40 °C	0
	Active Discharge	1.75	Temperature field at end of storage phase	No flux	$300 - 2.2t^{0.5}$ °C	40 °C	500-750

As noted above, using the same Dirichlet BC across all design points means that a calculation of the amount of energy that was moved into the chamber (during charging) and out of the chamber (during discharge) becomes a direct measure of the effectiveness of each design. For the charging simulations, the quantity of interest is the change in heat energy content of the salt and aluminum ($=E_{gained}$); this is equivalent to the heat gained

through the bottom inlet minus the heat absorbed by or lost through the insulation. For the discharging simulation, the quantity of interest is defined as the total amount of energy that leaves the chamber through the top plate outlet (=$E_{removed}$). These two values are used to develop the objective function for optimization. The normalized objective functions for charging and discharging are:

$$G_{charge}(\boldsymbol{x}) = \frac{E_{gained} - E_{gained,min}}{E_{gained,max} - E_{gained,min}} \tag{51}$$

$$G_{discharge}(\boldsymbol{x}) = \frac{E_{removed} - E_{removed,min}}{E_{removed,max} - E_{removed,min}} \tag{52}$$

The subscripts *Min* and *Max* refer respectively to the minimum and maximum E_{gained} and $E_{removed}$ among all simulated design points. Since these minimum and maximum values are not known *a priori*, estimated values are used in the initial stages of the optimization procedure. Upon completion of all the simulations, the estimated values are replaced by the actual minimum and maximum values, meaning that the final values G_{charge} and $G_{discharge}$ range from 0 to 1 for all design points. These two equations are combined into a single objective function:

$$G_{total}(\boldsymbol{x}) = \frac{G_{charge}(\boldsymbol{x}) + 2G_{discharge}(\boldsymbol{x})}{3} \tag{53}$$

The objective function above weighs the discharging result more heavily than the charging result. Earlier work [114] has demonstrated that the gap in performance between good and poor designs is larger for discharging than for charging. Since it is anticipated that the overall efficacy of a design depends more significantly on its discharging efficiency, the final form of the objection function gives more weight to $G_{discharge}$. Indeed, the results of the present work support this assumption: the difference between $E_{gained,\,max}$ and $E_{gained,\,min}$ is significantly lower than that between $E_{removed,\,max}$ and $E_{removed,\,min}$. Among the charging simulations at all design points, E_{gained} ranges from 3.819 to 4.428 MJ: the disparity between $E_{gained,\,min}$ and $E_{gained,\,max}$ amounts to 0.609 MJ, or 13.8% of $E_{gained,\,max}$. In the discharging simulations, $E_{removed}$ ranges from 3.024 to 4.386 MJ: this range is 1.362 MJ, or

31.1% of $E_{removed,\ max.}$ In practical terms, this suggests that while most of the designs in the parameter space would perform adequately in charging, wide variation in their discharging effectiveness could be expected.

4.3 Numerical Methods

4.3.1 Governing Equations and Discretization Scheme

The governing equations are the same as those used in earlier chapters, except that those used here are the dimensional, axisymmetric version of those equations. Because the LHTSD design is cylindrical, because all heat fluxes and boundary conditions are axially symmetric, and because the flow is laminar, two-dimensional axisymmetric flow is assumed, viz. $v_\theta = 0$ and $\partial/\partial\theta = 0$ for all variables. Under these assumptions, the mass balance equation is:

$$\frac{\partial v_r}{\partial r} + \frac{\partial v_z}{\partial z} = 0 \tag{54}$$

where *r* is the radial direction, *z* is the axial direction, v_r is the radial velocity, and v_z is the velocity in the axial direction. The momentum balance and energy equations are:

$$\frac{\partial v_r}{\partial t} + \frac{\partial (v_r v_r)}{\partial r} + \frac{\partial (v_r v_z)}{\partial z} = -\frac{1}{\rho}\frac{\partial p}{\partial r} + \nu\left(\frac{\partial^2 v_r}{\partial r^2} + \frac{1}{r}\frac{\partial v_r}{\partial r} + \frac{\partial^2 v_r}{\partial z^2}\right) + A v_r \tag{55}$$

$$\frac{\partial v_z}{\partial t} + \frac{\partial (v_r v_z)}{\partial r} + \frac{\partial (v_z v_z)}{\partial z} = -\frac{1}{\rho}\frac{\partial p}{\partial r} + \nu\left(\frac{\partial^2 v_z}{\partial r^2} + \frac{1}{r}\frac{\partial v_z}{\partial r} + \frac{\partial^2 v_z}{\partial z^2}\right) + A v_z + g\beta(T - T_{char}) \tag{56}$$

$$\frac{\partial T}{\partial t} + v_r\frac{\partial T}{\partial r} + v_z\frac{\partial T}{\partial z} = \alpha\left(\frac{\partial^2 T}{\partial r^2} + \frac{1}{r}\frac{\partial T}{\partial r} + \frac{\partial^2 T}{\partial z^2}\right) + \frac{LS_{trans}}{C_p}\left(\frac{\partial F_{LS}}{\partial t}\right) \tag{57}$$

In the above, ν is the kinematic viscosity, ρ is the density, T is the temperature, T_{char} is a characteristic temperature, and β is the coefficient of expansion. In the energy equation, $\alpha = k/\rho C_p$ is the thermal diffusivity, where k is the thermal conductivity and C_p is the heat capacity.

The choice of C and B can have significant effect on the flow patterns [118, 120]. Although researchers have reported using a range of values from 10^3-10^{10} for C (0.001 is the standard value for B), the most common values for C are 10^5-10^6 [52, 117, 118]. However, the accuracy of these choices depends on the nature of the PCM, the solver used, and the scale of the simulation. Furthermore, the effect of changes to the parameters diminishes as $\frac{C}{B}$ grows larger [118, 120]. In the present work, C is set to a relatively low value of 10^4 s^{-1}, while B is equal to 0.001. These values were chosen based on previous validation work using this solver [115], as well as the observation that values of C larger than this have only a very small impact on the flow of melted salts for these simulations.

As with all numerical simulations, the assumptions made here lead to limitations in the accuracy of the model. Perhaps primarily, the simulation does not fully account for changes in density within the salts. On the one hand, the Boussinesq approximation is a valid assumption for these simulations: $\Delta\rho/\rho_o$ is equal to approximately 0.025 for temperature range of these experiments [72], which is well below the 0.1 limit often cited as the upper limit for the validity of the Boussinesq approximation [116]. However, the difference between the density of the solid salts and the liquid salts, which is about 10% [71, 72], is not fully accounted for in these simulations. This might affect the physical results both in the expansion and contraction of the overall volume of the salts within the chamber and also in the possibility that solid salts might become unattached to the side of the LHTSD and sink within the liquid. The latter concern is particularly notable considering recent work that has shown that so-called close contact melting created by sinking solids within a PCM can lead to large increases in melting rates [100, 121-123].

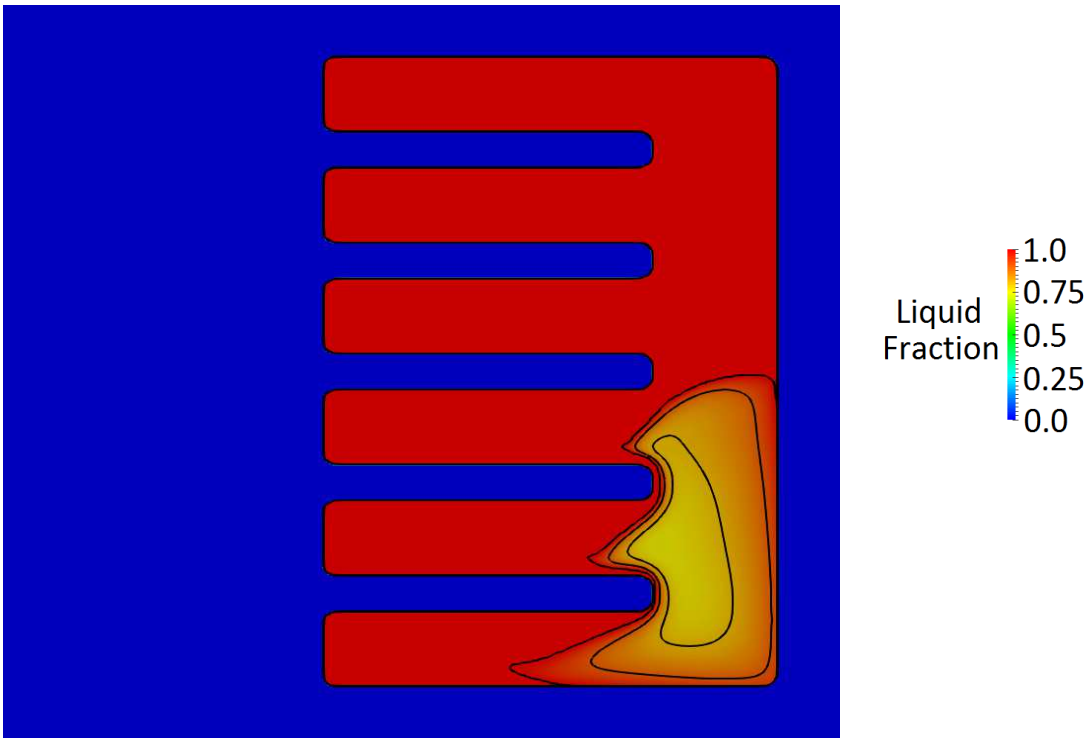

Figure 43. Discharge simulation during the end of the melting process (230 minutes). The contour lines represent a liquid fraction of 1.0, 0.9, and 0.8. Even at this late stage in melting, close contact melting would not be increased significantly by a free floating solid.

For the simulations in this work, however, there are reasons to believe that the effects of solid-liquid volume change and close contact melting would be limited. First, the expansion and contraction of the volume of the salts would likely not change the melting or solidification process significantly. The solid-liquid volume change would necessitate the existence of air voids within the LHTSD, particularly when all or part of the PCM was in a solid state. During the energy discharge process, the salts would likely first solidify around the cooling fins, and this would lead to voids near the top of the chamber but fully within the salts. Since it is unlikely that a void would be directly touching the metal fins, these voids would have a relatively small effect on the charging process, where heat is concentrated in the fins and near the bottom of the chamber. In the discharging process, on the other hand, the voids would grow large only near the tail end

of the discharge, when the outflux is lowest, and thus would have a small effect on overall results. More importantly, close contact melting would have a limited effect on these simulations because the fins would significantly restrict the movement of any free floating solids. Figure 43 shows that even late in the melting process, the complex shape of unmelted solids would keep them from freely sinking to bottom. Furthermore, because the flux of heat is concentrated near the axis and the unmelted solids would be near the outer radius of the LHTSD, solids that did contact the bottom of the chamber would not melt significantly faster because of that close contact. For these reasons, the assumption that changes in PCM density need only be considered with respect to natural convection (i.e. the Boussinesq approximation) is valid.

4.3.2 Pressure Stabilization Scheme for Segmented Domains

The previous section outlined strategies to control oscillations in the temperature field, a key difficulty for the simulations in this project. A second key numerical challenge for these simulations arises when the domain is segmented (i.e. by large fins) and most of the active flow is in one of these segments, as it is early in a melting simulation. In a pressure-Poisson algorithm such as this, the velocity algorithm first calculates an initial velocity u*; this initial velocity does not satisfy the continuity equation. The pressure poisson process then creates a pressure field which corrects this problem, ensuring that the final velocity obeys mass conservation. In a purely natural-convection simulation, the only force creating the initial velocity is buoyancy. The direction of this force is determined by the buoyancy term in equation (56):

$$g\beta(T - T_{char}) \tag{58}$$

If the characteristic temperature T_{char} is set at the melting temperature of the salts, as is most obvious choice, all of the buoyancy-created initial velocity is in the positive direction. In a non-segmented simulation of a closed container, the pressure poisson process has no problem turning this initial velocity away from solid walls and frozen material. High

pressure zones are formed where the flow impacts solids, low pressure zones develop where the fluid moves away from solid surfaces, and the appropriate circulation patterns grow within the container.

In a segmented domain, though, the induced pressure field leads to a problem: the strong local pressures necessary to turn the flow cannot be adequately balanced in order to meet the boundary conditions at all of the aluminum-salt interface. As Figure 44 shows, for example, early in a bottom-heated melting simulation, a strong low pressure area appears in the lower left corner of the PCM in order to slow the upward flow created by the heat entering on the bottom left. This is necessary to create the correct flow locally. But solving the pressure poisson equation over the whole field causes that strong low pressure to be balanced by a high pressure in the upper segments. As the channels on the right begin to melt, the pressure field pushes fluid down through the channel, creating a situation in which mass is clearly not conserved.

To solve this problem, it is necessary to create a pressure field in the lower segment that is bipolar: rather than having the velocity corrected in the melt area by a large low pressure area, there needs to be a dipole of high and low pressure. In order to achieve this, the buoyant forces that create the initial velocity u* must push in both directions, rather than just up. This can be done by changing the characteristic temperature in the buoyant force term (equation (56)). As noted above, if the characteristic temperature T_{char} is the melting temperature, then the buoyant forces all push upward (the final term is always positive). On the other hand, if T_{char} is the maximum fluid temperature, then the buoyant force term is always negative and the forces are all directed downward. But at some point in between the melting point and the maximum field temperature, there are some positive and some negative buoyant forces. In this middle ground, the pressure poisson process has less work to do create an appropriate circulation. Experience demonstrates that a correctly defined T_{char} creates a pressure dipole in the lower segment rather than a strong high or low

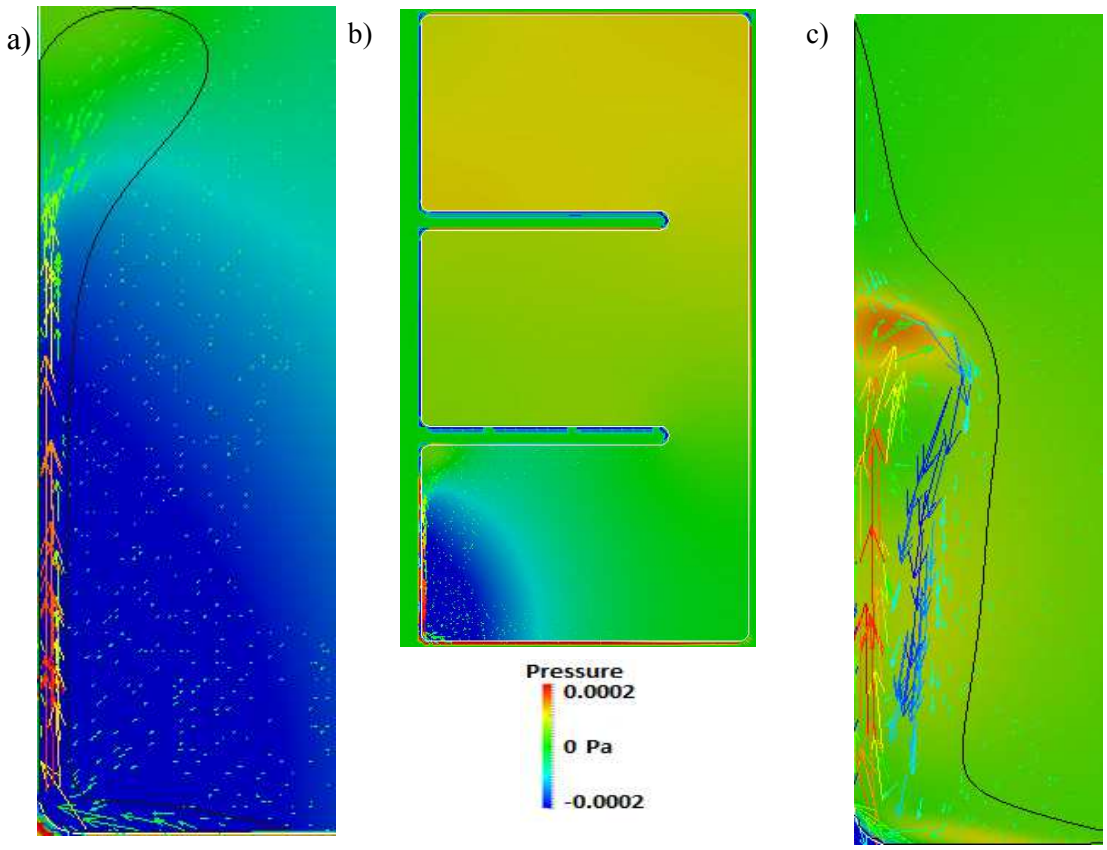

Figure 44. A bottom-heated simulation with a segmented domain early in the melting process. $F_{liquid} = .8$, an approximate indicator of the boundary between melted and frozen salts, is marked in black. (a) If T_{char} is set to T_{melt}, a strong low pressure is set up in the bottom corner of the domain in order to balance the strong upward buoyant forces. This leads to unnatural flows: notice the lack of circulation in the melted region), as well as (b) a segmented pressure domain (c) A dynamic T_{char} creates a pressure field in the flow area with high and low pressure areas. This produces a more natural bidirectional flow early in the simulation and eliminates the segmented pressure domain.

pressure zone, and this eliminates the push or pull of fluid into or out of the channel between domain segments.

How to find this ideal T_{char}? Not surprisingly, it changes as the flow develops. If the simulation is in balance, the average pressure in one segment should be approximately

equal to that in its neighboring segment. Unfortunately, this is difficult to quantify. However, a key indicator of the health of this balance is the amount of net flow between the segments: if there is significant net flow from one segment to another, the flow is not obeying mass conservation and needs to be corrected. We can use this fact to adjust T_{char} as the flow develops. If the net flow through the channels between segments is negative, the characteristic temperature is slowly raised: this creates a higher overall pressure in the lower segment and drives the flow in the channels upward. The opposite is done if the net flow is positive.

For the sake of stability, the characteristic temperature is calculated as a fraction of the distance between the melting temperature and the high temperature T_{high} in the flow field:

$$T_{char} = T_{melt} + F(T_{high} - T_{melt}) \tag{59}$$

where T_{melt} is the melting temperature. In most of these segmented simulations, F is set initially to 0.65, and updated according the following:

$$F = \begin{cases} F - 0.001, if\ flux_{channel} > a \\ F, if\ -a \leq flux_{channel} \leq a \\ F + 0.001, if\ flux_{channel} < -a \end{cases} \tag{60}$$

where $flux_{channel}$ is the computed net vertical flux through the channels between segments and a is a small coefficient chosen to avoid overcorrections ($10^{-8}\frac{m^3}{s}$ in most cases). In practice, F generally stays in the range between 0.55 and 0.75. T_{char} is updated approximately every 25 time steps.

4.4 Results

The Results section is divided into five sections. The first section explains the screening process used to reduce the number of independent variables from five to three. The following two sections explain the dynamic Kriging strategy used to create the objective function response surface and introduce the overall results of this optimization

process. The remaining two sections explore in detail the objective function surface for charging and discharging.

4.4.1 Variable Screening

As explained above, each design point in the parameter space is defined by five independent variables. However, creating a five-dimensional response surface is prohibitively expensive [137] , and so it is necessary to further reduce the number of independent variables. A screening process is used to eliminate those independent variables whose effect on the objective function is negligible.

The screening process used here, based on the work of Morris [136], calculates the sensitivity of the objective function to variation in the design parameters at random locations in the parameters space. The key component of this calculation is the elementary effect, which is a measure of change in the objective function when a single variable is perturbed. If a given problem has *k* independent normalized variables, an elementary effect d_i of variable x_i is defined as:

$$d_i(\boldsymbol{x}) = \frac{y(x_1, x_2, \dots, x_{i-1}, x_i + \Delta, x_{i+1}, \dots, x_k) - y(\boldsymbol{x})}{\Delta} \qquad (61)$$

where **x** is a "baseline" set of independent variables x_i, y is the objective function, and Δ is a change in the normalized variable x_i such that $x_i+\Delta$ remains in the region of experimentation (i.e. $x_i + \Delta \leq 1$). In the present study, Δ is set to 0.25; this is large enough to avoid any local oscillations in the objective function but not so large that it will fail to capture significant nonlinearities in the objective function [137].

The elementary effect for *n* independent variables is calculated by performing *n*+1 simulations [136]. To do this, a $(n+1) \times n$ matrix **B** is created where each row of ***B*** provides a set of input variables for a single simulation. The first row is a randomly generated set of input variables x_i; each subsequent row varies one input variable by Δ. Running all *n*+1 simulations produces a randomized elementary effect value for each of the *n* input

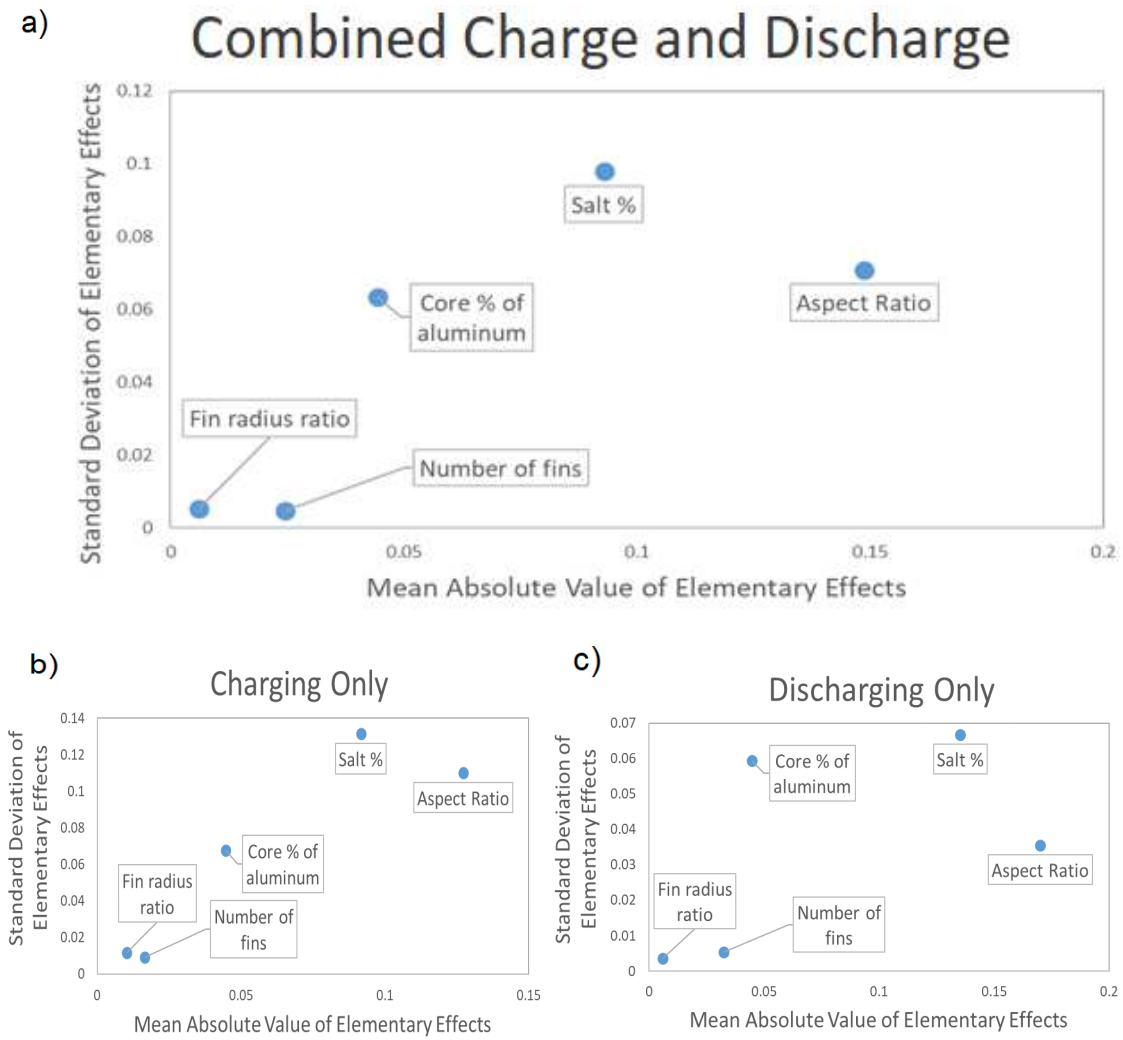

Figure 45. Results of the elementary effect-based screening process. A combination of a high standard deviation and a high mean value for the elementary effect indicates that an independent variable is of interest in the optimization process. The three variables with the largest and most widely varying elementary effects were the salt percentage, the core percentage of aluminum, and the aspect ratio.

variables. If *r* elementary effect calculations are desired for each input variable, the entire set of prescreening test cases **X** is defined by producing multiple versions of $\boldsymbol{B}$**:**

$$\boldsymbol{X} = \begin{bmatrix} \boldsymbol{B_1} \\ \boldsymbol{B_2} \\ \vdots \\ \boldsymbol{B_r} \end{bmatrix} \tag{62}$$

In this work, four sets of input variables ***B*** were used, requiring a total of 24 test cases and producing four elementary effects for each of the five independent variables (SP, AR, CP, NF, and FR).

Table 14: Final Variables for Optimization Procedure

Identifier	Variable	Dependency	Range
SP	Salt Percentage (by Volume)	Independent	0.5-0.75
AR	Aspect ratio	Independent	0.4-2.25
CP	Percentage of Aluminum in Core	Independent	0.3-0.75
--	Number of fins n	Constant	5
--	Fin radius percentage	$0.5 + 0.4\left(1 - \left(\left(\frac{(SP + 1 - AR + CP)}{3}\right)^2\right)\right)$	0.5-0.9

A large average size for the elementary effects of a given variable indicates that the objective function is sensitive to that variable. A large statistical spread among these effects suggests that changes to the variable produces nonlinear changes in the objective function. Figure 4 shows the results of the screening process. Three variables that significantly impact the objective function are seen to be: aspect ratio (AR), salt percentage (SP) and core percentage of aluminum (CP). As seen in Figure 4(a), the AR has the largest average elementary effect. From Figure 4(b-c) the SP displays the largest variation in its effect. The CP, although less important to the objective function than salt percentage or aspect ratio, has a significantly higher mean and standard deviation than the two fin variables. In addition, the charging and discharging results are quite similar, suggesting

that the same variables are equally important in the two different processes. The screening process shows that the fin radius percentage (FR) and number of fins (NF) cause only small variations in the objective function, for both charging and discharging simulations. Therefore, the optimization problem reduces to a three-dimensional parameter space defined by the AR, SP, and CP.

Table 14 shows the three independent variables in the parameter space. NF is set to five. FR is dependent on the normalized values of the three independent variables in order to keep fin thickness between 4 mm and 2 cm in the entire design space. Note that for the optimization procedure, the ranges for the three independent variables were altered slightly in response to the simulation results during the screening process (compare Table 12 and Table 14). The reduction in parameter dimensions in the present design therefore now leads to a computationally tractable three-parameter design space over which the response

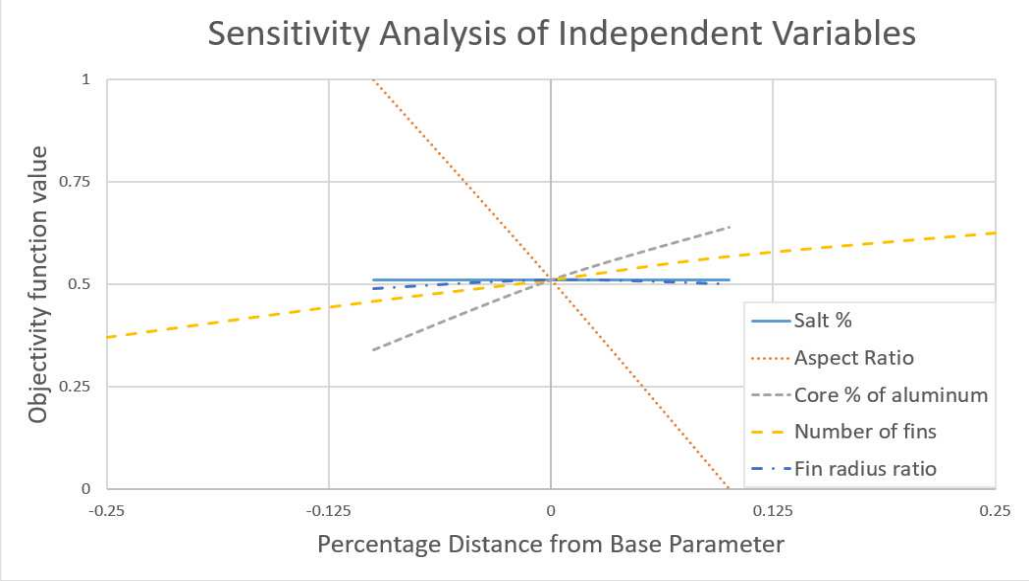

Figure 46. Results of sensitivity analysis of five independent variables. The objective function is clearly most sensitive to aspect ratio and core percentage of aluminum in the vicinity of the base design.

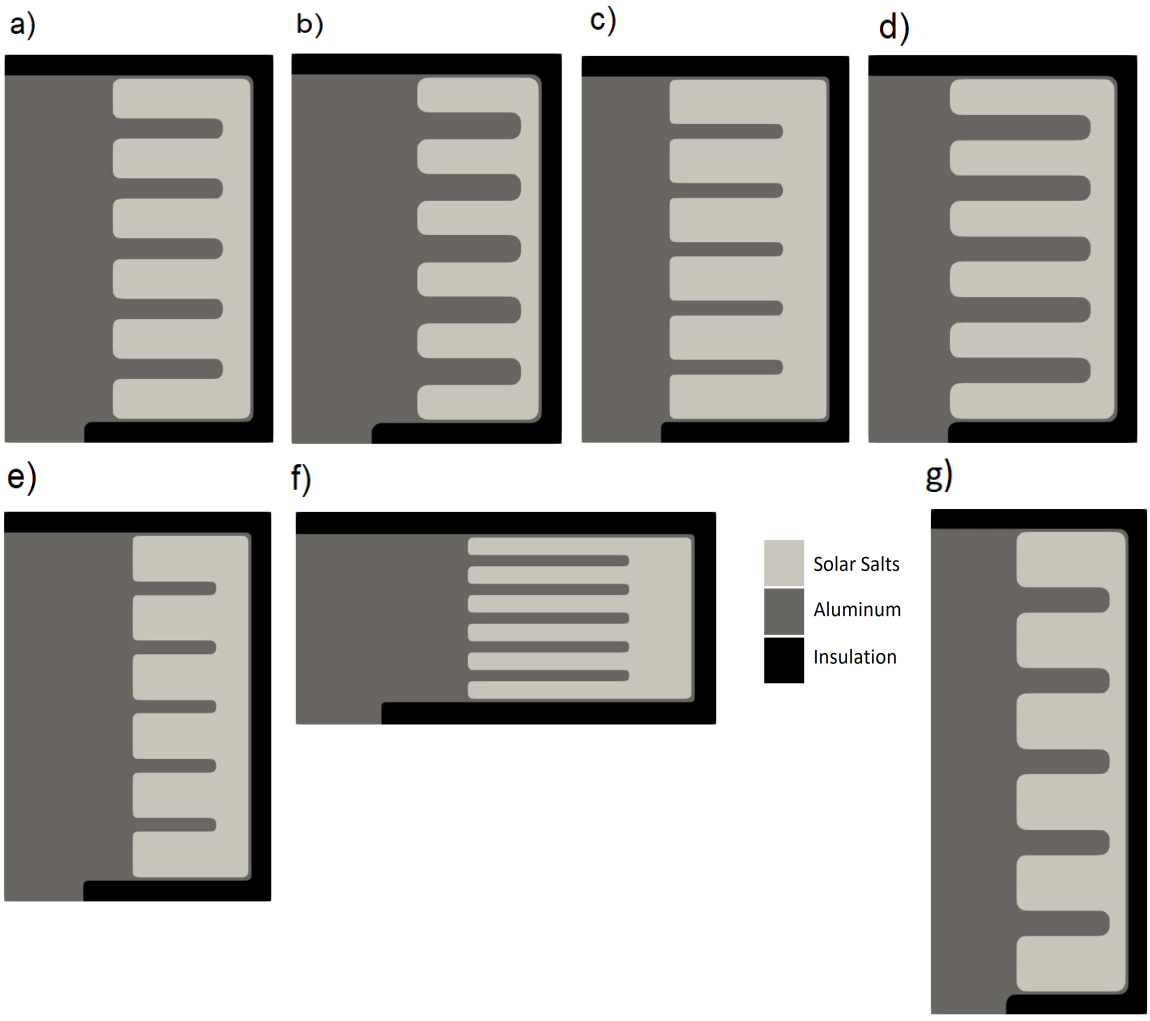

Figure 47. Examples of geometries within the parameter space. (a) middle point (0.5,0.5,0.5) (b) low SP (0,0.5,0.5) (c) high SP (1,0.5,0.5) (d) low CP (0.5,0,0.5) (e) high CP (0.5,1,0.5) (f) low AR (0.5,0.5,0) (g) high AR (0.5,0.5,1). Coordinates are listed as the normalized values for (SP, CP, AR).

surface needs to be constructed. Figure 47 illustrates a range of the designs within this 3-parameter space.

In order to protect against the possibility that an important variable might be eliminated by the variable screening process, a backup variable screening method--finite difference sensitivity analysis—was also performed. For this approach, the value of the

objective function is first determined at the base design. Then, for each independent variable, two additional simulations are run, one with the value of the independent variable increased by 10% and the other with the variable decreased by 10% while holding all other independent variables constant (note that in the case of the discrete "number of fins" variable, the variation is one fin (25%) rather than 10%). The results provide a first and second derivative value for the objective function in the direction of the independent variable in the vicinity of the base design. The advantage of this approach is that it provides this information with a relatively small number of test cases: in this case, eleven. The chief disadvantage is that this information is all determined in the vicinity of the base design. If these values vary significantly through the parameter space, this approach can produce misleading data about the overall sensitivity of the variables. As a backup procedure, however, this risk is not a problem.

The results from this backup process bolster those from the main variable screeing: it identifies AR and CP as two key variables. Interestingly, it does not suggest that SP is important. These results suggest that a more robust screening procedure, such as the elementary effect process used here, does provide a better understanding of the important independent variables than a simple sensitivity analysis. Indeed, the sensitivity analysis, which focuses on the behavior of variables at a base design point, indicated that the core percentage was a much more important variable than salt percentage, which proved (as seen below) to be false. Because the elementary effect procedure samples random design points throughout the parameter space, it correctly predicted that core percentage was a significantly less important than salt percentage and aspect ratio. Given that it only required about twice as many simulations as the sensitivity analysis, these results suggest that the elementary effect process is worth the extra investment in time.

4.4.2 Dynamic Kriging (DKG) Methods for Surrogate Modeling

Previous work [144] shows that dynamic Kriging (DKG) is an efficient and accurate approach to response surface creation, particularly when the number of known design points is on the order of 100, as it is in this case. For this reason DKG is used to build the response surface for this work.

DKG constructs a response surface by considering input data at known sample points as the result of a stochastic process [137]. Consider *n* design points **x** with corresponding *n* known responses **y**. The form of the Kriging surface at these sample points sums a mean surface with local fitted surface:

$$y(\boldsymbol{x_0}) = \sum_{i=0}^{r} \lambda_i p_i(\boldsymbol{x_0}) + Z(\boldsymbol{x_0}) \tag{63}$$

where y is the response, $\boldsymbol{x_0}$ is a design point, the first term on the right hand side is the fitted polynomial mean surface of order r, p_i is the polynomial function of order i, λ_i is the regression coefficient for the polynomial function, and $Z(\boldsymbol{x_0})$ is the correlation function, which represents local variations from the mean surface. The order r and the correlation function type must be chosen *a priori*. The most commonly used correlation function is a Gaussian function of the form:

$$\boldsymbol{R} = R_{ij} = corr(Z(\boldsymbol{x^i}), Z(\boldsymbol{x^j})) = exp\left[-\sum_{k=1}^{m} \theta_j \left[x_k^i - x_k^j\right]^2\right] \tag{64}$$

where m is the number of independent variables, x_k^i is the value of the kth dimension at the ith function center, and the shaping coefficient θ_j is the jth member of a vector $\boldsymbol{\theta}$. The values of $\boldsymbol{\theta}$ are determined by maximizing a log-likelihood function of the form:

$$likelihood = -\frac{n}{2} ln[2\pi\sigma^2] - \frac{1}{2} ln[|\boldsymbol{R}|] - \frac{1}{2\sigma^2}(\boldsymbol{y} - \boldsymbol{P\lambda})^T \boldsymbol{R^{-1}} (\boldsymbol{y} - \boldsymbol{P\lambda}) \tag{65}$$

In this formulation, n is the number of design points, $\mathbf{y} = [y(\mathbf{x_1})\ y(\mathbf{x_2})\ \ldots\ y(\mathbf{x_n})]$, $\mathbf{P} = P_{ji} = \mathbf{p}_i(x_j)$, and $\mathbf{y} - \mathbf{P\lambda}$ is the residual surface. σ^2 is the process variance, defined as:

$$\sigma^2 = \frac{1}{n}((\boldsymbol{y} - \boldsymbol{P\lambda})^T \boldsymbol{R^{-1}} (\boldsymbol{y} - \boldsymbol{P\lambda})$$

Maximizing this likelihood produces optimal values of $\boldsymbol{\theta}$, thus defining the most likely version of $\mathbf{y}$. With this complete, it is then possible to predict values at unknown design points:

$$\hat{y}(\boldsymbol{x_0}) = \boldsymbol{P\lambda} + \mathbf{r}^{\mathbf{T}}\boldsymbol{R}^{-\mathbf{1}}(\boldsymbol{y} - \boldsymbol{P\lambda}) \tag{66}$$

Here $\mathbf{x_0}$ is a design point with an unknown objective function value, and $\mathbf{r}$ is a correlation vector between the local known design points $\mathbf{x^i}$ and the unknown point $\mathbf{x^0}$. The end result is that Kriging produces a surface comprised of basis functions that are influenced by the spacing of known design points [137-139, 144-147].

DKG improves upon traditional Kriging [138, 139] because uses machine-learning techniques to obviate the need to choose the order of the polynomial function and the type of covariance function *a priori*. Because Kriging takes the known data to be the result of a stochastic process, it allows for the assignment of an uncertainty value at any design point in the parameter field. This uncertainty is defined by the predicted variance σ_p^2 at a given point $\mathbf{x^0}$:

$$\sigma_p^2(\boldsymbol{x_0}) = \sigma^2\left(1 + \boldsymbol{w_0^T R w_0} - 2\boldsymbol{w_0 r_0}\right) \tag{67}$$

where $\mathbf{w_0}$ is the weight vector from the predictor equation (66) when that equation is put in the form:

$$\hat{y}(\boldsymbol{x_0}) = \boldsymbol{w_0^T y} \tag{68}$$

This ability to estimate the uncertainty at unknown design points is important for the dynamic Kriging process [138, 141]. DKG uses these uncertainty values to check the accuracy of a range of polynomial and correlation functions. DKG tests 3 different polynomial orders (0, 1, and 2) and 7 different options for the correlation function (Gaussian, exponential, general exponential, linear, spherical, cubic, and spline) [148]. The DKG algorithm automatically selects the polynomial order r that results in the minimum cross-validation error, $\sum_{j=1}^{N}\left[\hat{y}(x_j) - \lambda_i p_i(x_j)\right]^2, i = 0, \ldots, r$, and the correlation function that produces the largest log-likelihood function (equation (65)).

4.4.3 Dynamic Kriging Results for the Construction of the Response Surface (Objective Function)

The Kriging response surface is built iteratively. Simulations are run at 25 initial design points, and the results at these points are used to calculate an initial surface. The DKG algorithm evaluates the uncertainty of this initial surface, and if necessary uses an machine-learning adaptive sampling process [138] to identify the next set of 20 design points. In the present case, three iterations are performed with DKG, meaning that a total of 85 design points are used to construct the final response surface. This requires 170 simulations, as both a charging and a discharging simulation must be run at each design point.

Table 15: Optimal Design Points for Charging, Discharging, and Combined

	Normalized Values			Actual Values		
	Salt %	*Aspect Ratio (H:W)*	*Core %*	*Salt %*	*Aspect Ratio (H:W)*	*Core %*
Charging	1.00	0.18	0.96	0.750	0.733	0.736
Discharging	0.48	0.29	0.57	0.620	0.936	0.599
Combined	0.71	0.27	0.54	0.677	0.899	0.589

The DKG algorithm allows for the calculation of the objective function value at any point in the parameter space. Because the objective function for the present case is not highly nonlinear, the optimal design points for charging, discharging, and the combination of the two are determined by directly searching the space for the highest objective function values. Objective function values at increments of 0.01 (normalized) for each independent variable are obtained; therefore, the total number of points searched is 100^3. The iso-surfaces for the three objective functions, shown in Figure 48, are constructed from these discrete objective function values. The cross sections of the objective function space at the combined optimal point in Figure 50 are obtained in the same manner. The design points

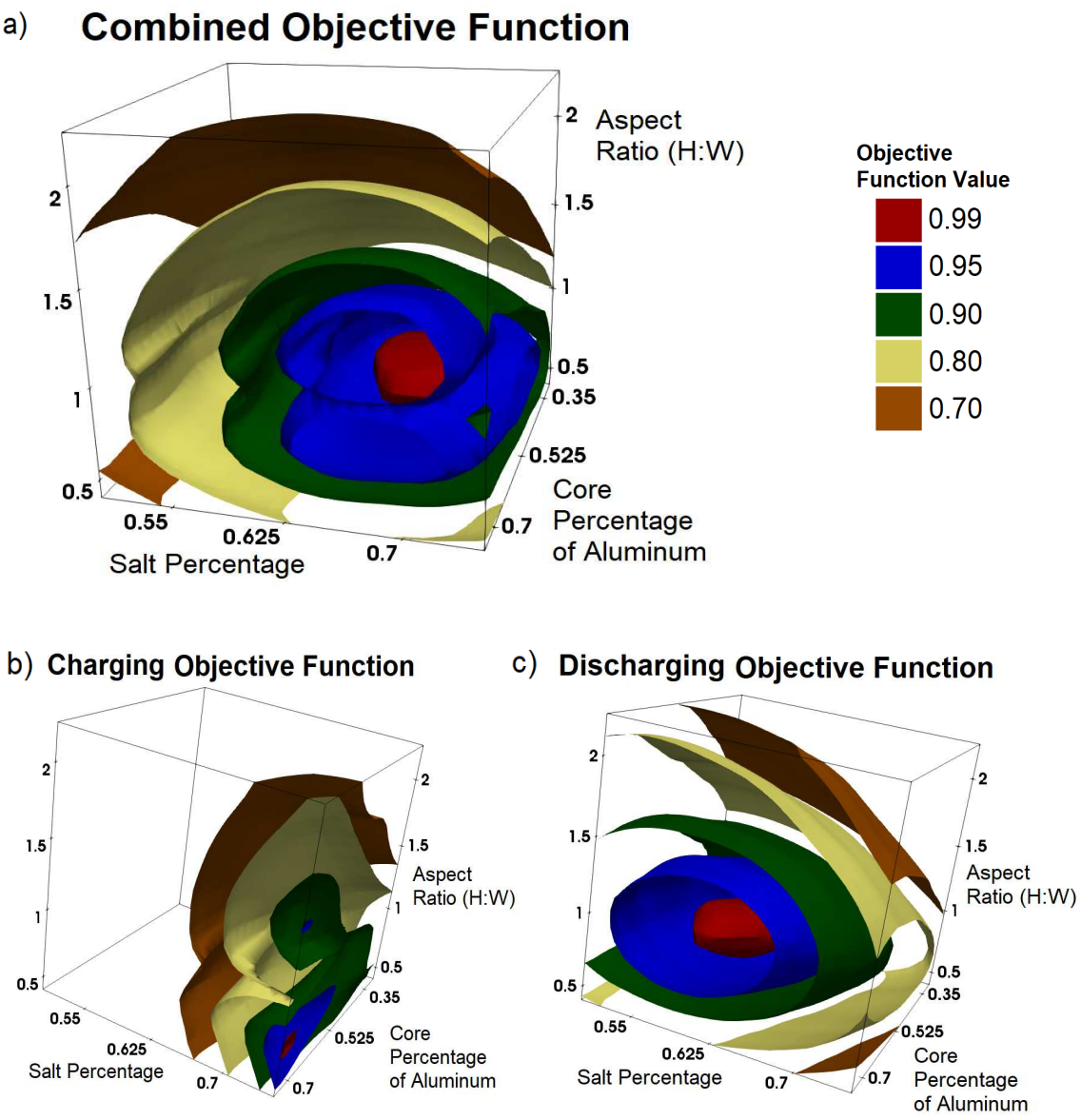

Figure 48. Isosurfaces of the normalized objective function for (a) combined charging and discharging (b) charging and (c) discharging. The objective function values range from 0 to 1.0, with 1.0 being the optimal design point. Therefore the red isosurfaces at 0.99 give a good indication of the location of the optimal point in each figure.

with the highest objective function value for charging, discharging, and the combined objective function (i.e. the optimal design points) are shown in Table 15. These optimal designs are also pictured in Figure 49.

In order to provide input data to analyze the accuracy and behavior of the objective function, simulations are run at seven new simulation points: one at the optimal combined point (0.678, 0.900, 0.543) and one in each orthogonal direction from the optimal point. Table 16 lists the percentage error between the response surface prediction of the objective function value and the simulation results at these seven design points. The error in the response surface for charging ranges from 0.73% to 6.3%; the error for discharging varies from 0.12% to 1.05%. The average errors for charging, discharging, and combined objective functions among the seven design points are 2.2%, 0.45%, and 0.75%, respectively.

While the average errors are very low, the errors are consistently higher error for the charging simulations than for discharging simulations. This can be explained at least in part by the narrow range of results obtained in the charging simulations (see Section 3.2), which makes small differences in simulation results appear larger in terms of a normalized objective function. For instance, the low AR charging simulation has the highest error among the test design points at 6.3%. For this design point, the predicted E_{gained} is 4.260 MJ; the actual E_{gained} is 4.299. Thus while the difference amounts to a 6% error in the

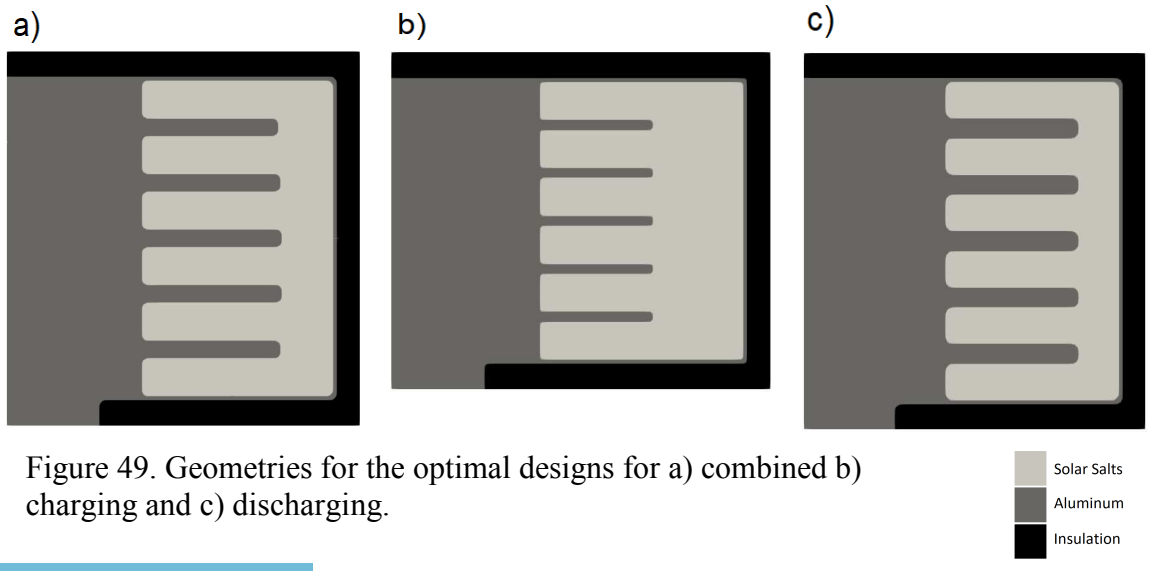

Figure 49. Geometries for the optimal designs for a) combined b) charging and c) discharging.

normalized objective function (the predicted objective function value is 0.723 while the simulation value is 0.786), it is an error of less than 1% (0.91%) in terms of simulation results. It is difficult to pinpoint exactly why the error is highest at this point in the charging objective function, since this is not a region with particularly high gradients or notable nonlinearity in the objective function. But a small change in the flow patterns within the

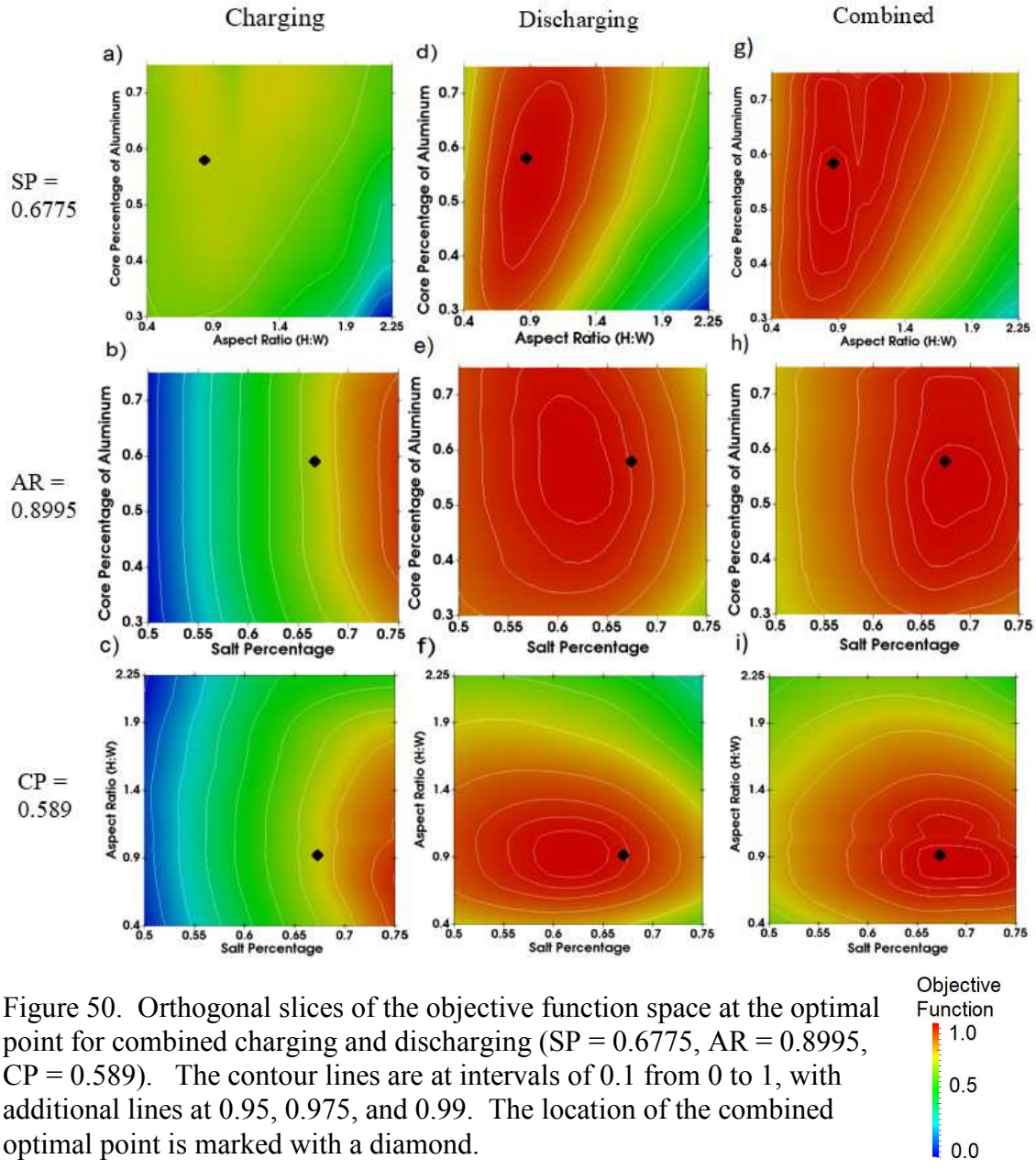

Figure 50. Orthogonal slices of the objective function space at the optimal point for combined charging and discharging (SP = 0.6775, AR = 0.8995, CP = 0.589). The contour lines are at intervals of 0.1 from 0 to 1, with additional lines at 0.95, 0.975, and 0.99. The location of the combined optimal point is marked with a diamond.

simulation or a small input error might easily lead to a 1% change in E_{gained}, and thus produce the noted error in the objective function. Despite this one relatively large error value, though, the fact that the average prediction errors for these seven design points are on the order of 1% suggest that the response surface provides a good representation of the behavior of the device in the vicinity of the optimal design within the parameter space.

Table 16: Test Point Results

	Design Points (Actual Values)			**Objective Function Percent Error (Predicted vs. Simulation Results)**		
	Salt %	*AR*	*Core %*	*Charging*	*Discharging*	*Combined*
Optimal	0.678	0.900	0.543	2.29	0.43	0.68
High S%	0.738	0.900	0.543	1.86	1.05	0.49
Low S%	0.550	0.900	0.543	1.11	0.13	0.08
High AR	0.678	1.880	0.543	1.92	0.33	0.09
Low AR	0.678	0.493	0.543	6.30	0.89	3.03
High C%	0.678	0.900	0.345	1.15	0.17	0.73
Low C%	0.678	0.900	0.705	0.73	0.12	0.13
			Average Error	**2.20**	**0.45**	**0.75**

4.4.4 Effect of AR, SP, and CP on the Objective Function during Charging

The optimization procedure results in a response surface that also provides insights into the effect of the aspect ratio (AR), salt percentage (SP) and Al core percentage (CP) on the design. These insights aid in understanding the behavior of the device in the charging and discharging phases and therefore can provide general guidelines for the design of such LHTSD devices.

The isosurfaces in Figure 48(b) and the contours in Figure 50(b) and (c) show that the gradients of the objective function are higher in the direction of the SP axis than in the direction of the AR or CP axes. The charging objective function is therefore seen to be dominated by SP: at almost all values of aspect ratio and core percentage, more salt in the chamber leads to a quicker absorption of energy into the LHTSD. The importance of SP is attributable to the fact that the devices with a higher percentage of salt have a higher energy density for a given temperature range. This can be seen in Figure 51(a). As the simulation nears the four hour mark, the low SP design has absorbed more energy than the high SP designs. Beyond four hours, however, the low SP design lags behind the high SP and optimal designs. The decline in the performance of the low SP design occurs between 3.5 hours and 4.5 hours. Figure 51(b) shows that this period coincides with the period in which the low SP design is fully melted while the high SP and optimal designs are not. During this time, the melted PCM in the low SP design cannot absorb as much heat energy as the partially melted salts in the high SP design. Figure 51(c) shows that this leads to a rapid increase in average aluminum temperature in the low SP design. The high aluminum temperatures in the low SP design lead to a lower flux of energy late in the simulation; by the end of the simulation time, the low SP design has fallen behind the high SP design in terms of E_{gained}. The larger volume of aluminum in the low SP design spreads heat quickly through the chamber, but the higher energy density of the optimal and high SP designs make them capable of absorbing more energy over the full simulation period.

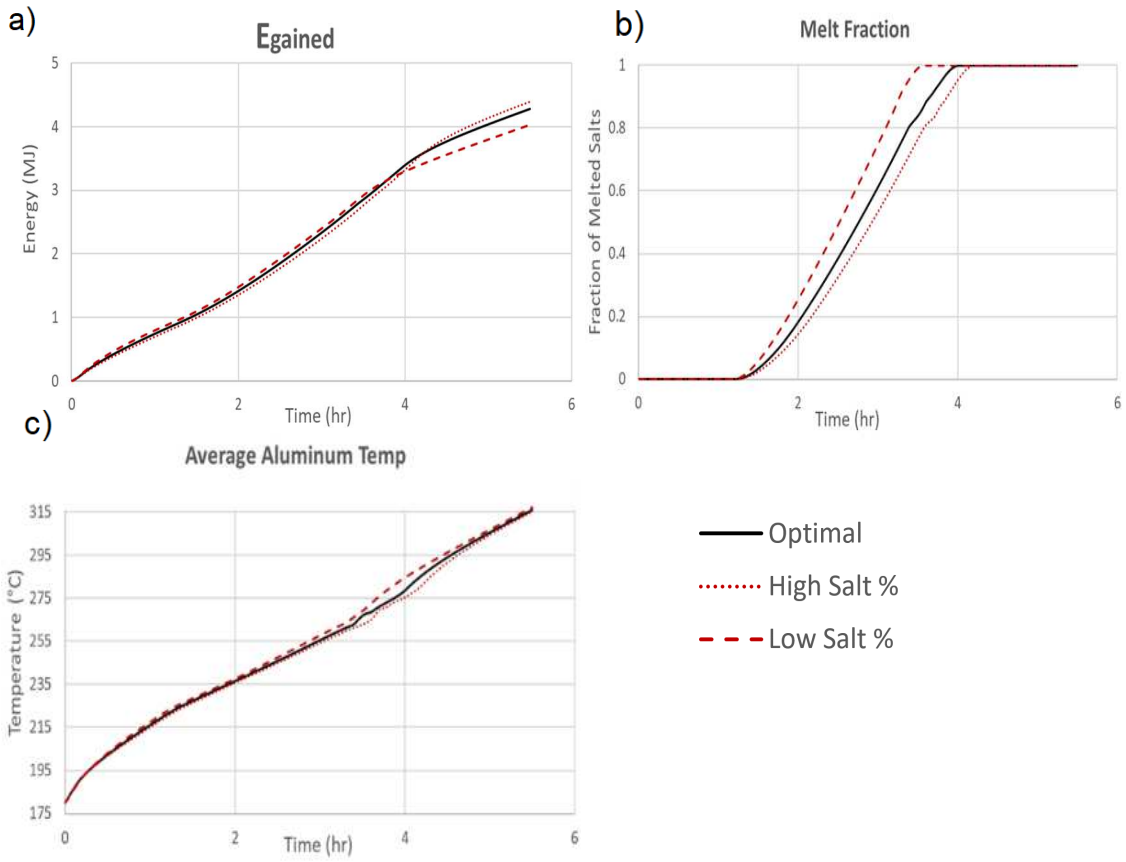

Figure 51. A comparison of the optimal, high salt percentage, and low salt percentage simulations during charging. (a) E_{gained} is the thermal energy stored in the salt and the aluminum. (b) Fraction of the salt within a design that is melted at a given time. (c) Average temperature of all aluminum within the design.

While SP dominates the charging objective function, AR has a significant effect on charging efficiency. Figure 52(a) shows that high AR designs produce significantly higher flow velocities than the low AR and optimal designs. But as Figure 52(b) illustrates, the horizontal fins restrict these flows: the recirculation within each section limits the movement of heat energy into the upper part of the chamber. Conduction is also limited by the high AR design. Figure 53(a) shows that the standard deviation of temperature within the aluminum is consistently high in high AR designs. This is because the narrow core of the high AR design impedes the movement of heat into the upper core and into the

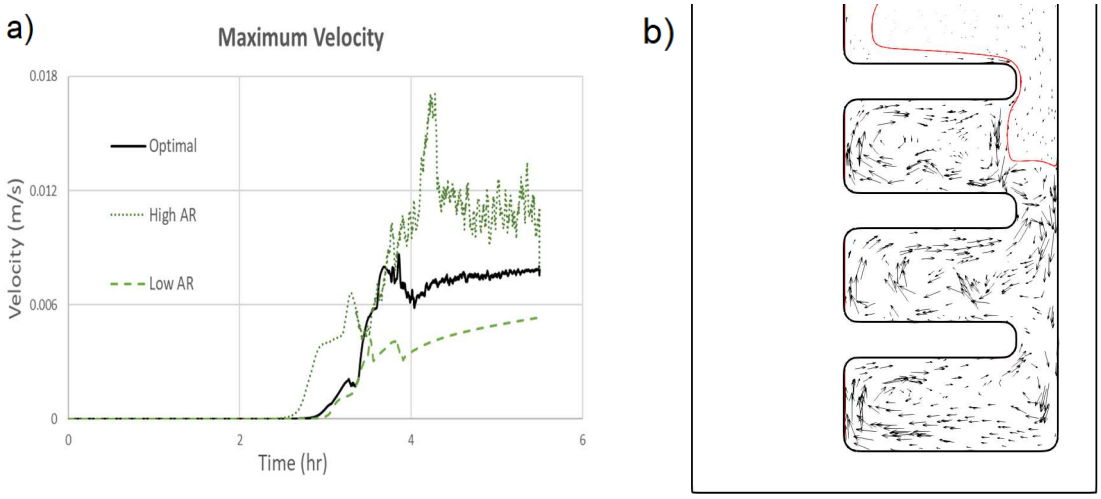

Figure 52. Comparison of charging simulations with different AR values. (a) Maximum velocity (b) lower section of high AR chamber at 3 hours 50 minutes. The red line is the melt boundary ($F_{LS} = 0.9$).

fins. Figure 53(b) shows that the result of this uneven distribution of heat in the aluminum is a decreased influx for the first four hours of the simulation. In short, the narrow aluminum core of the high AR design combined with the division of its chamber by the fins make it difficult for either conduction or convection to spread heat into the upper ends of the chamber. The low AR and optimal designs, on the other hand, have lower velocities, but their larger cores and surface area of the aluminum structures allow for more effective conduction of heat into the upper segments of the LHTSDs.

While the global parameters SP and AR have a significant effect on the objective function, the parameters governing the internal configuration of the LHTSD have a negligible effect on charging effectiveness. The screening procedure, as seen in Figure 45(b), demonstrates the low sensitivity of the charging objective function to fin radius and the number of fins. The optimization procedure confirms those conclusions from the screening process; the core percentage of aluminum (CP) is significantly less important to efficiency than SP and AR. Table 16 shows that at the optimal values for AR and SP, large changes in CP have small effects on the charging objective function. Similarly, Figure

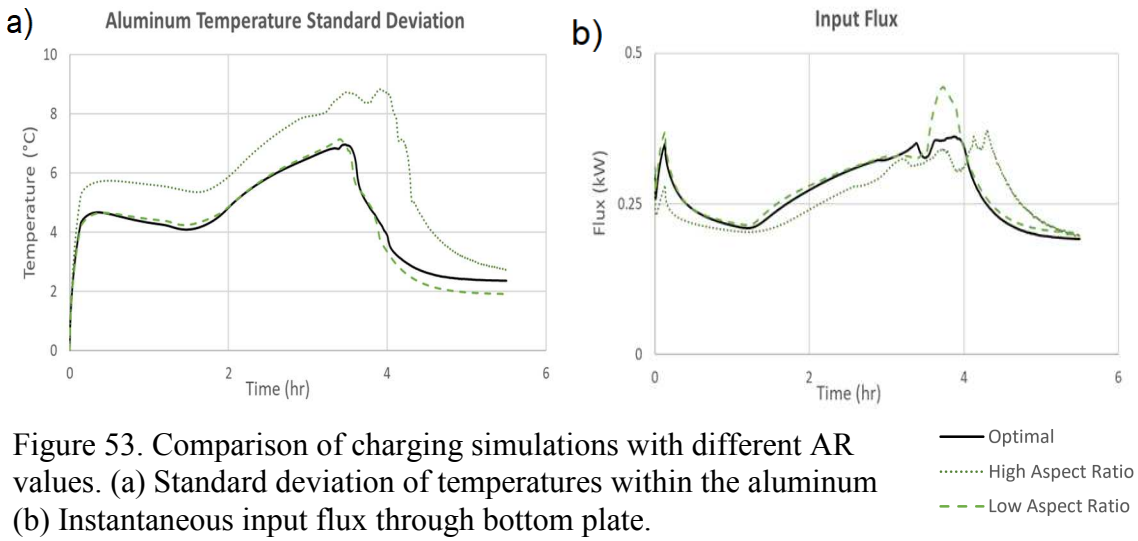

Figure 53. Comparison of charging simulations with different AR values. (a) Standard deviation of temperatures within the aluminum (b) Instantaneous input flux through bottom plate.

50(b) demonstrates that when the AR is held steady at 0.8995, charging effectiveness is strongly dependent on SP: the charging objective function value remains largely unchanged when CP is altered. Therefore, the amount of aluminum in the LHTSD is important to its performance. The way in which the aluminum is distributed within the LHTSD, such as in the core or the fins, is of secondary importance.

In summary, the charging objective function demonstrates two key points. First, the high energy density of the PCM makes a high salt percentage (SP) crucial to charging effectiveness. Second, the charging objective function is more sensitive to the parameters governing the overall structure of the LHTSD (SP and AR) than it is to the arrangement of aluminum within the LHTSD (CP and fin parameters).

4.4.5 Effect of AR, SP, and CP on the Objective Function During Discharging

Unlike charging, discharging effectiveness is not determined primarily by a high SP. Table 15 shows that the ideal SP for discharging is 0.62—approximately midway between the minimum of 0.5 and the maximum of 0.75. Figure 50(e) and (f) show the nonlinear relationship between SP and the discharging objective function: in both figures,

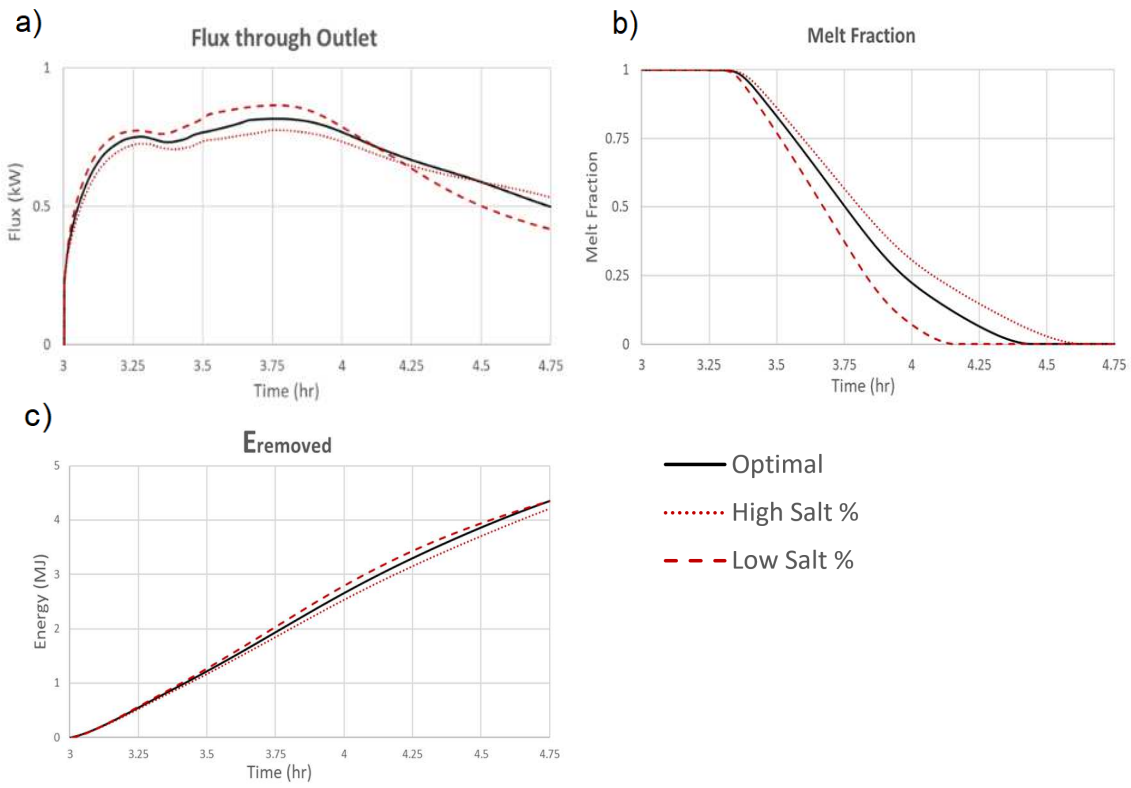

Figure 54. Comparison of high salt percentage, low salt percentage and optimal simulations during discharge. Notice that plots begin at 3 hours, when the active discharge phase occurs after 3 hours of the storage phase. (a) Instantaneous flux through the upper outlet. (b) Melt fraction. (c) $E_{removed}$

the objective function values fall off significantly from the optimal discharging point in the direction of both lower and higher SP. The optimal design combines the energy density of the high SP design with the enhanced heat movement of the low SP design. The heat spreading capabilities of the low SP design means that it performs well early in the active discharge phase, as seen in Figure 54(a). Figure 54(b) shows that this leads to an efficient solidification of salt. However, after an hour of active discharge, the low SP design has significantly less available energy for further discharge, as evidenced by the paucity of unmelted salts in Figure 55(a) in comparison to Figure 55(b). Figure 54(a) illustrates the rapid decline in outflux for the low SP design after this point. The high SP design has the

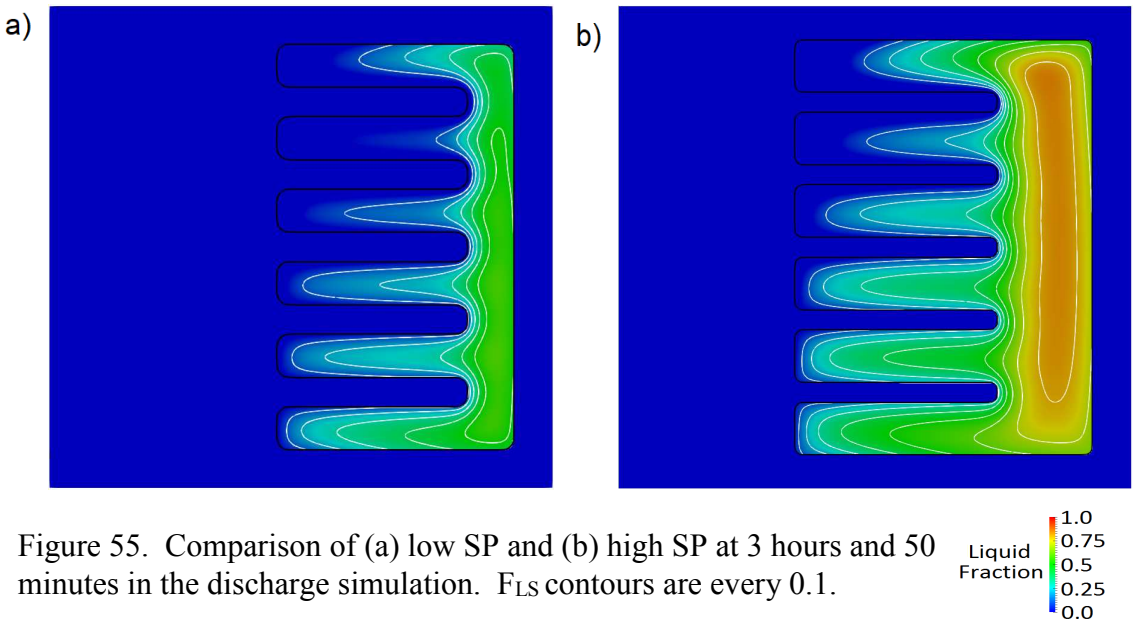

Figure 55. Comparison of (a) low SP and (b) high SP at 3 hours and 50 minutes in the discharge simulation. F_{LS} contours are every 0.1.

opposite problem. Figure 54(a) illustrates its outflux during the early active discharge period is significantly lower than the optimal and low SP designs. At the end of this period, as Figure 55(b) and Figure 54(b) show, it has large amounts of available latent heat energy. As a result, its outflux late in the active discharge period is high. But this effectiveness late in the simulation, Figure 54(c) demonstrates the high SP finishes the simulation with a low $E_{removed}$. The optimal design, as shown in Figure 54(a), is one that is able to best combine the efficient withdrawal of energy in the early stages with a sustained outflux in the later stages of discharge when the temperatures in the LHTSD decrease. These results suggest the necessity to balance the amount of energy stored in the device (encouraged by a high SP) with the ability to transfer heat from the salts to the outlet plate (demanding a low SP).

High SP is less important in the discharging phase than it is in the charging phase. But in both charging and discharging, the objective function is most sensitive to the variables associated with the overall structure of the LHTSD. The variable with the highest effect on efficiency in the discharge phase is AR. This is apparent in the Figure 48(c) and Figure 50(d) and (e): the highest gradients in the objective function are consistently in the

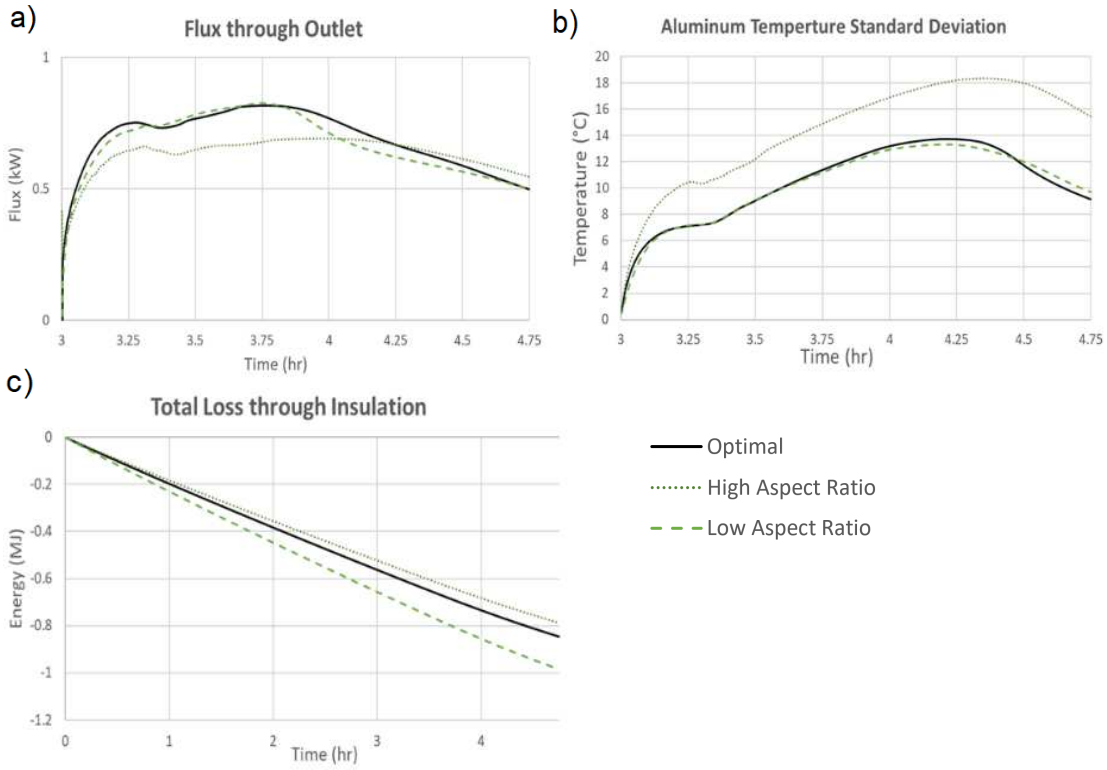

Figure 56. Comparison of high and low AR simulations during discharge: (a) instantaneous flux through the top outlet (b) standard deviation of temperature within the aluminum (c) the summed loss through the insulation, respectively.

direction of AR. As with SP, the effect of AR is nonlinear and the optimal AR is a matter of balance between two factors. In this case, the increased conductive heat transfer encouraged by a larger aluminum surface area and wider core of the low AR designs is balanced by larger heat losses of the low AR designs. Figure 56(a) reveals that high AR designs have consistently low outflux through the active discharge phase as the narrow core cannot transfer heat from the bottom of the chamber to the top as quickly as the wide core of the low AR designs. Figure 56(b) shows the resulting high standard deviation of temperature within the high AR design. The excess cooling near the top plate and top fin exacerbates the heat movement problem. As Figure 57 illustrates, solidification occurs

relatively uniformly along the core and fins in the low AR design, but in the high AR design the salts at the top of the chamber solidify more quickly than those near the bottom. As the low thermal conductivity salts solidify near the outlet of the high AR design, the flow of heat from the salts to the aluminum is further restricted. On the other hand, Figure 56(a) shows that the low AR design has a high outlet flux early in the active discharge phase. Figure 57(a) illustrates how low AR designs use aluminum to transfer energy to the outlet during discharging: the wide core eases energy transport from top to bottom, and slender fins increase contact between the salt and the aluminum. But while the high AR designs have significant disadvantages, the advantages of the low AR designs have a limit: the flat shape of the design means that the overall device has a large outer surface area. Figure 56(c) shows that this leads to large heat losses. The optimal design therefore must combine

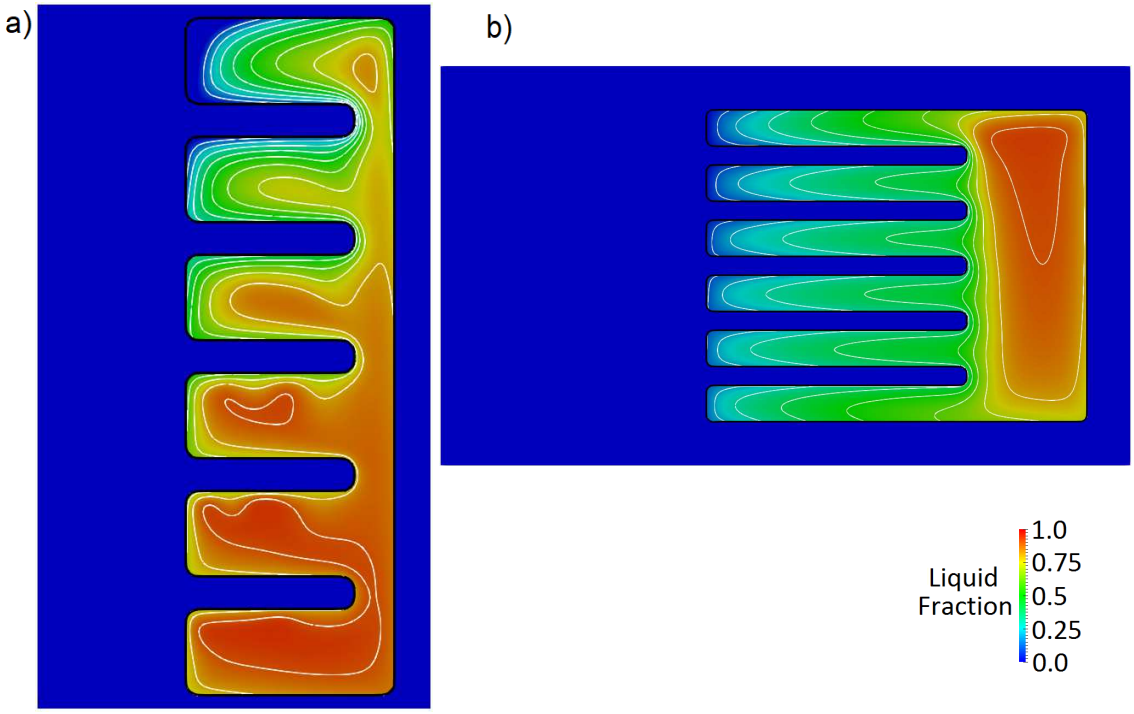

Figure 57. Comparison of (a) high and (b) low AR designs at 3 hours and 40 minutes in the discharge simulation. F_{LS} contours are every 0.1.

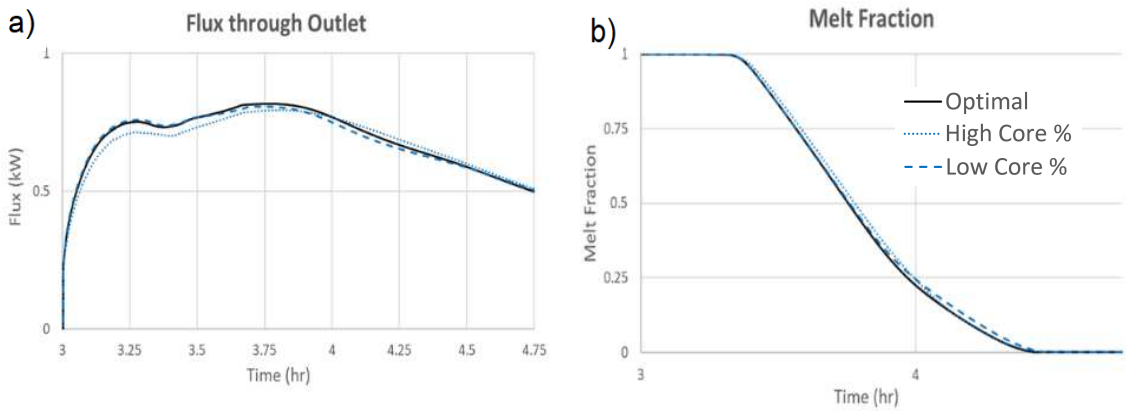

Figure 58. Comparison of high and low CP designs during discharge: (a) instantaneous outlet flux (b) melt fraction.

the conductive strength of the low aspect ratio with an overall shape that is conducive to energy storage.

As with charging, the variables associated with the internal configuration of the aluminum have negligible effects on the optimal configuration for discharging. Figure 45(c) shows that the fin variables are not significant. Among the three independent variables in the optimization procedure, CP is the independent variable with the smallest effect on the discharging objective function, as evidenced by the small vertical gradients in Figure 50(d) and (e). Figure 58 demonstrates that the high and low CP designs produce results that are very similar for all meaningful measures, including outlet flux and melt fraction. As with charging, the arrangement of aluminum in the core and fins has a much smaller effect on efficiency than the total amount of aluminum in the device.

In summary, while a higher SP leads to better charging performance throughout the parameter space, discharging effectiveness depends on two key balances. In the case of SP, this balance is between the high energy density of the high SP designs and the effective movement of heat encouraged by low SP designs. For AR, a balance must be struck between the conductive advantages of low AR designs and the lower insulative heat losses of moderate AR models. But just as with the charging simulations, discharging efficiency

depends more on the overall shape of the LHTSD than on the internal configuration of the aluminum.

4.5 Conclusion

This chapter uses numerical simulations to optimize the design for an aluminum-fin and PCM thermal storage device. The main challenge to optimizing such systems is the vast number of potential designs for such a LHTSD. We use three strategies to significantly decrease the expense of this process while retaining its accuracy. First, the expense of individual simulations is reduced by the numerical scheme, which utilizes adaptively refined Cartesian grid meshes, a strongly coupled implicit scheme for conjugate heat transfer, and a sharp interface method to define the boundary between different materials. Second, screening variables using the elementary effect analysis reduces the number of independent variables from five to three with marginal loss of accuracy in calculating the objective function. Assuming the necessity of simulating approximately ten design points in each variable direction in order to estimate the value of the objective function throughout the parameter space, this reduces the number of necessary known design points from 10^5 to 10^3. However, simulations at 10^3 design points are still prohibitive, even in 2D. The third strategy to decrease the required number of simulations is to use dynamic Kriging (DKG) to build a response surface for the objective function over the parameter space. This procedure produces an accurate response surface while running simulations at only 85 design points.

Aside from providing quantitative values of design parameters that yield an optimal design for this parameter space, this work provides several general insights concerning the optimization of such LHTSD designs. First, a higher percentage of salts has significant benefits due to the high energy density of the PCM. This is true especially for charging, where high salt percentage designs consistently absorb more energy than their counterparts

with lower salt percentages. In discharging, the benefits of a high salt percentage are still important, but are counterbalanced by the need for a robust heat spreading mechanism that limits the effectiveness of high salt percentage designs.

The second insight is that convection plays a smaller role in the success of the device than expected based on heuristics: designs with high aspect ratios consistently produce the highest maximum velocities in the simulations, particularly in charging, but these convection patterns are less helpful in transferring energy than conduction through the aluminum core-fin arrangement.

Finally, and most importantly, both the screening and the Kriging process suggest that the internal configuration of the aluminum finned device is less important than the broad characteristics of the chamber as a whole. The number of fins, the radius and thickness of the fins, and the division of aluminum between the core and the fins all had a less significant effect on performance than the shape of the chamber (aspect ratio) and the ratio of salt to aluminum within the device.

In summary, the results show that a LHTSD must balance the energy density of the PCM with the heat spreading capability of metal fins, and that this balance depends largely on the overall structure of the LHTSD rather than its internal configuration. The precise nature of this balance is governed by the particular design goals: energy storage needs, time of charging and discharging, the expected temperature range, and the particular materials will all have an effect on the optimal design. Such variability means not only that numerical simulations but also an efficient optimization process are a crucial tools in economically maximizing design performance. The cost of a full scale optimization of a LHTSD is significantly curtailed by the numerical, screening, and response surface construction procedures outlined in this chapter.

CHAPTER FIVE
CONCLUSION AND FUTURE WORK

For decades, engineers, environmental activists and public health officials alike have imagined solar cooking as a salve to the ecological, economic, and health wounds created by the widespread use of wood as a cooking fuel in the underdeveloped countries. Unfortunately, the inconveniences of solar cookers have led to very low rates of adoption in target communities. The inconvenience of cooking outdoors during the day, the inability of solar ovens to duplicate the high direct heat used in traditional cooking, and the undependability of solar energy, among other things, have made solar cooking unattractive to those who have access to it.

One potential solution to this problem is an effective small-scale thermal storage device (TSD). A cooker that could store solar energy and release it in the evening would be much more adaptable to traditional daily schedules. Furthermore, by collecting energy through the day and releasing it in a shorter amount of time, it could potentially reach the cooking temperatures necessary to fry and sauté food.

The main purpose of this thesis is to develop and apply a numerical simulation and optimization procedure to improve the design of a small-scale thermal storage device, such as one that might be used with a solar cooker. An effective storage device needs to absorb solar energy quickly, release the energy at a high temperature, be affordable, and be manageable within a small household. A latent-heat thermal storage device using solar salts fulfills the latter two requirements—solar salts are inexpensive and widely available, and the use of latent heat storage means a relatively small chamber can hold enough energy to cook a family meal. This project addresses the chief challenge of such a device: it needs to absorb and release energy from the solar salts quickly and effectively enough to cook food at a high temperature.

The thesis has made four central contributions to efforts to develop a practical LHTSD that would fulfill these requirements:

1) A robust numerical tool able to simulate accurately the performance of small-scale LHTSDs during both charging and discharging. The Cartesian grid solver developed is capable of simulating the numerically stiff, convection-dominated melting processes within the storage device. Test simulations demonstrate that results using the this numerical scheme match those of a range of experimental and numerical benchmarks, including three dimensional flows within complex geometries. In addition, the scheme is flexible enough to be capable of efficiently performing long-term (48 hour) simulations in two dimensions, smaller-scale simulations in three dimensions, and the hundreds of mid-scale simulations necessary for an optimization process.

2) A detailed description of the melt and flow behavior of solar salts within an aluminum-finned LHTSD. The thesis chapters describe the flow development in different geometries. Chapter three, for instance, describes the progression during charging of a bottom-heated LHTSD through thin layer melting, bottom-dominated melting, side-dominated melting, and top-dominated melting and shows that significantly different designs progress through these four stages. In addition, the melt and flow behavior during discharge are quite similar: lower circulation velocities and temperature gradients lead to an oblong melted section at the center of salt chambers. More surprisingly, the use of experimental data in chapter three leads to the conclusion that solar salt thermal properties are difficult to predict with precision. This uncertainty—which is not atypical of mixed material PCMs—has multiple causes, including hysteresis, material degradation, and uneven mixtures in resolidified salts. The work here suggests that researchers interested in mixed material PCMs, especially solar salts, need to carefully test the values of PCM thermal properties in different situations.

3) A set of general guidelines for the design of LHTSDs. It is difficult to predict the flow effects of different complex geometries; indeed, this is one reason that an effective numerical scheme is crucial to design development. Still, the thesis shows that a number of general rules about design can be formulated. For instance, one key design concern is attempting to balance the development of convective flows, which require open spaces within the device, with conductive effectiveness, which is boosted by small maximum distances between an aluminum surface and interior salt positions. A key concern for bottom-heated LHTSDs is transferring heat into the aluminum in the top half of the container early on in the charging process. This encourages the device to move through the bottom-dominated stage of heating as quickly as possible, which is crucial to encouraging the strong vertical circulation patterns typical of the side-dominated stage.

In discharging, the demands on the design can be significantly different. While design seems to matter little in the discharging process when the salts are completely melted, it becomes crucial as soon as a thin layer of salt solidifies on the aluminum surface. At this point, finned containers become much more effective at quickly transferring energy out of the salts. The smaller distance between the remaining liquid salts and the aluminum surfaces in the finned case means that the insulating effects of the solidified salts do less to slow the transfer of heat from the salts to the aluminum.

Finally, the thesis suggests that these questions of fin design might be secondary to broader questions of the container shape and composition. Chapter four shows that the internal configuration of the aluminum finned device is less important than the broad characteristics of the chamber as a whole. The number of fins, the radius and thickness of the fins, and the division of aluminum between the core and the fins all had a less significant effect on performance than the shape of the chamber (aspect ratio) and the ratio of salt to aluminum within the device.

4) An optimization process for fin design within an LHTSD that allows for a large parameter space and the efficient use of computational and human resources. There are

three main prongs that make this an effective approach to optimization. First, the numerical techniques accurately and efficiently compute heat and mass transport in a variety of geometries without generating grids to conform to each geometry. This moderates the expense of individual simulations. Second, a pre-screening process identifies the independent variables with the largest and most nonlinear effect on the objective function in the optimization process: this reduces the parameter space. Finally, a dynamic Kriging-based optimization approach constructs a multidimensional response surface using sparse input datasets and a machine-learning processes; the resulting response surface is then analyzed to identify an optimal design. The combination of the above three strategies is shown to result in an approach that can aid in the design of an optimal LHTSD.

Future work aims to expand the parameter space of LHTSDs which can be analyzed using the approach developed in this thesis. The current work has demonstrated the effectiveness of this numerical approach to the development and optimization of small-scale LHTSDs. Its chief limitation, however, lies in the availability of computer resources to perform optimization of a full range of possible designs; the designs beyond the capacity of the current approach designs include non-axisymmetric and larger-scale three-dimensional designs. In order to optimize a parameter field that includes such potential designs, it will be necessary to make the simulation of flows within a larger number of three-dimensional designs feasible. The most promising approach to this problem is use artificial diffusion in the momentum equation to allow for larger grid sizes in the simulations. Additional artificial diffusion would serve to wash out small scale velocity gradients, which require a very fine grid for resolution. The assumption is that these small scale movements are not significant in terms of the melt boundaries, flow behavior, and efficiency of LHTSDs. If the minimum grid size can be increased significantly by this process, it will be possible to combine the three-dimensional simulations of chapter three with the optimization procedures from chapter four. It would then be possible to optimize

the fin design within a more open parameter space and to optimize non-axisymmetric LHTSDs as large as those that would be necessary for a household solar cooker.

REFERENCES

[1] T. Bauer, N. Pfleger, N. Breidenbach, M. Eck, D. Laing, and S. Kaesche, "Material aspects of Solar Salt for sensible heat storage," *Applied Energy,* vol. 111, pp. 1114-1119, 2013.

[2] T. Bauer, D. Laing, and R. Tamme, "Overview of PCMs for Concentrated Solar Power in the Temperature Range 200 to 350°C," *Advances in Science and Technology,* vol. 74, pp. 272-277, 2010.

[3] X. Zhang, J. Tian, K. Xu, and Y. Gao, "Thermodynamic evaluation of phase equilibria in NaNO3eKNO3 system," *Journal of Phase Equilibria,* vol. 5, pp. 441-446, 2002.

[4] H. Ibrahim ElSaeedy, "Thermal Properties of (Na 0.6 K 0.4)NO3 Thermal Storage System in the Solid-Solid Phase," *International Journal of Energy and Power Engineering,* vol. 5, p. 34, 2016.

[5] "Global Health Risks: Mortality and Burden of Disease Attributable to Selected Major Risks," World Health Organization, Geneva, Switzerland2009.

[6] J. J. Lewis and S. K. Pattanayak, "Who adopts improved fuels and cookstoves? A systematic review," *Environ Health Perspect,* vol. 120, pp. 637-45, May 2012.

[7] J. Vanschoenwinkel, S. Lizin, G. Swinnen, H. Azadi, and S. Van Passel, "Solar cooking in Senegalese villages: An application of best-worst scaling," *Energy Policy,* vol. 67, pp. 447-458, 2014.

[8] F. Yettou, B. Azoui, A. Malek, A. Gama, and N. L. Panwar, "Solar cooker realizations in actual use: An overview," *Renewable and Sustainable Energy Reviews,* vol. 37, pp. 288-306, 2014.

[9] N. L. Panwar, S. C. Kaushik, and S. Kothari, "State of the art of solar cooking: An overview," *Renewable and Sustainable Energy Reviews,* vol. 16, pp. 3776-3785, 2012.

[10] E. Cuce and P. M. Cuce, "A comprehensive review on solar cookers," *Applied Energy,* vol. 102, pp. 1399-1421, 2013.

[11] M. Bansal, R. P. Saini, and D. K. Khatod, "Development of cooking sector in rural areas in India - A review," *Renewable and Sustainable Energy Reviews,* vol. 17, pp. 44-53, 2013.

[12] P. P. Otte, "Warming Up to Solar Cooking – A Comparative Study on Motivations and the Adoption of Institutional Solar Cookers in Developing Countries," *Energy Procedia,* vol. 57, pp. 1632-1641, 2014.

[13] A. Harmim, M. Merzouk, M. Boukar, and M. Amar, "Solar cooking development in Algerian Sahara: Towards a socially suitable solar cooker," *Renewable and Sustainable Energy Reviews,* vol. 37, pp. 207-214, 2014.

[14] A. H. Tesfay, O. J. Nydal, and M. B. Kahsay, "Energy storage integrated solar stove: A case of solar Injera baking in Ethiopia," in *4th IEEE Global Humanitarian Technology Conference, GHTC 2014, October 10, 2014 - October 13, 2014*, San Jose, CA, United states, 2014, pp. 659-666.

[15] D. Y. Dasin, A. S. Aliyu, and N. Y. Godi, "Verification of the performance of parabolic concentrating solar cooker on some food stuffs cooked in bauchi - North East, Nigeria," in *2015 6th International Renewable Energy Congress, IREC 2015, March 24, 2015 - March 26, 2015*, Sousse, Tunisia, 2015.

[16] P. P. Otte, "Solar cooking in Mozambique-an investigation of end-user's needs for the design of solar cookers," *Energy Policy,* vol. 74, pp. 366-375, 2014.

[17] F. Agyenim, N. Hewitt, P. Eames, and M. Smyth, "A review of materials, heat transfer and phase change problem formulation for latent heat thermal energy storage systems (LHTESS)," *Renewable and Sustainable Energy Reviews,* vol. 14, pp. 615-628, 2010.

[18] N. S. Dhaidan and J. M. Khodadadi, "Melting and convection of phase change materials in different shape containers: A review," *Renewable and Sustainable Energy Reviews,* vol. 43, pp. 449-477, 2015.

[19] R. M. Muthusivagami, R. Velraj, and R. Sethumadhavan, "Solar cookers with and without thermal storage-A review," *Renewable and Sustainable Energy Reviews,* vol. 14, pp. 691-701, 2010.

[20] A. Mawire, M. McPherson, and R. R. J. van den Heetkamp, "Discharging simulations of a thermal energy storage (TES) system for an indirect solar cooker," *Solar Energy Materials and Solar Cells,* vol. 94, pp. 1100-1106, 2010.

[21] A. Sharma, C. R. Chen, V. V. S. Murty, and A. Shukla, "Solar cooker with latent heat storage systems: A review," *Renewable and Sustainable Energy Reviews,* vol. 13, pp. 1599-1605, 2009.
[22] S. D. Sharma, D. Buddhi, R. L. Sawhney, and A. Sharma, "Design, development and performance evaluation of a latent heat storage unit for evening cooking in a solar cooker," *Energy Conversion and Management,* vol. 41, pp. 1497-1508, 2000.
[23] T. Bauer and N. Breidenbach, "Overview of Molten Salt Storage Systems and Material Development for Solar Thermal Power Plants," in *World Renewable Energy Forum*, 2012.
[24] B. Zivkovic and I. Fujii, "An Analysis of Isothermal Phase Change Within Rectangular and Cylindrical Containers," *Solar Energy,* vol. 70, pp. 51-61, 2001.
[25] K. Nithyanandam and R. Pitchumani, "Optimization of an encapsulated phase change material thermal energy storage system," *Solar Energy,* vol. 107, pp. 770-788, 2014.
[26] P. Charvát, L. Klimeš, and M. Ostrý, "Numerical and experimental investigation of a PCM-based thermal storage unit for solar air systems," *Energy and Buildings,* vol. 68, pp. 488-497, 2014.
[27] S. Jegadheeswaran and S. D. Pohekar, "Performance enhancement in latent heat thermal storage system: A review," *Renewable and Sustainable Energy Reviews,* vol. 13, pp. 2225-2244, 2009.
[28] C. Alkan, A. Sarı, A. Karaipekli, and O. Uzun, "Preparation, characterization, and thermal properties of microencapsulated phase change material for thermal energy storage," *Solar Energy Materials and Solar Cells,* vol. 93, pp. 143-147, 2009.
[29] A. Sarı and A. Karaipekli, "Thermal conductivity and latent heat thermal energy storage characteristics of paraffin/expanded graphite composite as phase change material," *Applied Thermal Engineering,* vol. 27, pp. 1271-1277, 2007.
[30] O. Mesalhy, K. Lafdi, A. Elgafy, and K. Bowman, "Numerical study for enhancing the thermal conductivity of phase change material (PCM) storage using high thermal conductivity porous matrix," *Energy Conversion and Management,* vol. 46, pp. 847-867, 2005.
[31] B. Chen, X. Wang, R. Zeng, Y. Zhang, X. Wang, J. Niu*, et al.*, "An experimental study of convective heat transfer with microencapsulated phase change material suspension: Laminar flow in a circular tube under constant heat flux," *Experimental Thermal and Fluid Science,* vol. 32, pp. 1638-1646, 2008.
[32] L. Fan and J. M. Khodadadi, "Thermal conductivity enhancement of phase change materials for thermal energy storage: A review," *Renewable and Sustainable Energy Reviews,* vol. 15, pp. 24-46, 2011.
[33] Y. Dutil, D. R. Rousse, N. B. Salah, S. Lassue, and L. Zalewski, "A review on phase-change materials: Mathematical modeling and simulations," *Renewable and Sustainable Energy Reviews,* vol. 15, pp. 112-130, 2011.
[34] M. Gharebaghi and I. Sezai, "Enhancement of Heat Transfer in Latent Heat Storage Modules with Internal Fins," *Numerical Heat Transfer, Part A: Applications,* vol. 53, pp. 749-765, 2007.
[35] V. Shatikian, G. Ziskind, and R. Letan, "Numerical investigation of a PCM-based heat sink with internal fins: Constant heat flux," *International Journal of Heat and Mass Transfer,* vol. 51, pp. 1488-1493, 2008.
[36] S. Tiari, S. Qiu, and M. Mahdavi, "Numerical study of finned heat pipe-assisted thermal energy storage system with high temperature phase change material," *Energy Conversion and Management,* vol. 89, pp. 833-842, 2015.
[37] J. Y. Long, "Simulation Investigation for Heat Transfer in Fin-Tube Thermal Storage Unit with Phase Change Material," *Advanced Materials Research,* vol. 168-170, pp. 895-899, 2010.
[38] H. Shokouhmand and B. Kamkari, "Numerical Simulation of Phase Change Thermal Storage in Finned Double-Pipe Heat Exchanger," *Applied Mechanics and Materials,* vol. 232, pp. 742-746, 2012.
[39] D. Groulx and W. Ogoh, "Solid-liquid Phase Change Simulation Applied to a Cylindrical Latent Heat Energy Storage System," *Proceedings of the COMSOL Conference,* 2009.
[40] V. Shatikian, G. Ziskind, and R. Letan, "Numerical investigation of a PCM-based heat sink with internal fins," *International Journal of Heat and Mass Transfer,* vol. 48, pp. 3689-3706, 2005.
[41] R. Akhilesh, A. Narasimhan, and C. Balaji, "Method to improve geometry for heat transfer enhancement in PCM composite heat sinks," *International Journal of Heat and Mass Transfer,* vol. 48, pp. 2759-2770, 2005.
[42] K. Schwarzer and M. E. V. da Silva, "Characterisation and design methods of solar cookers," *Solar Energy,* vol. 82, pp. 157-163, 2008.

[43] F. Fornarelli, S. M. Camporeale, B. Fortunato, M. Torresi, P. Oresta, L. Magliocchetti, *et al.*, "CFD analysis of melting process in a shell-and-tube latent heat storage for concentrated solar power plants," *Applied Energy,* vol. 164, pp. 711-722, 2016.

[44] S. Liu, Y. Li, and Y. Zhang, "Mathematical solutions and numerical models employed for the investigations of PCMs′ phase transformations," *Renewable and Sustainable Energy Reviews,* vol. 33, pp. 659-674, 2014.

[45] S. K. Sambasivan, S. Krishnan, A. Kapahi, and H. S. Udaykumar, "Tree-based Local Mesh Refinement for compressible multiphase flows," in *47th AIAA Aerospace Sciences Meeting including the New Horizons Forum and Aerospace Exposition, January 5, 2009 - January 8, 2009*, Orlando, FL, United states, 2009.

[46] K. Wittig and P. A. Nikrityuk, "Three-dimensionality of fluid flow in the benchmark experiment for a pure metal melting on a vertical wall," *IOP Conference Series: Materials Science and Engineering,* vol. 27, p. 012054, 2012.

[47] S. Kashani, A. A. Ranjbar, M. M. Madani, M. Mastiani, and H. Jalaly, "Numerical study of solidification of a nano-enhanced phase change material (NEPCM) in a thermal storage system," *Journal of Applied Mechanics and Technical Physics,* vol. 54, pp. 702-712, 2013.

[48] Y. Kim, A. Hossain, and Y. Nakamura, "Numerical Study of melting of a phase change material (PCM) enhanced by deformation of a liquid-gase interface," *International Journal of Heat and Mass Transfer,* vol. 63, pp. 101-112, 2013.

[49] H. Mirzaei, A. Dadvand, M. Mastiani, S. Sebti, and S. Kashani, "Melting of a phase change material in a horizontal annulus with discrete heat sources," *Thermal Science,* 2013.

[50] G. Petrone and G. Cammarata, "Numerical Simulation of Phase Change Materials Melting Process," *Computational Thermal Sciences,* vol. 5, pp. 227-237, 2013.

[51] S. Bellan, J. Gonzalez-Aguilar, M. Romero, M. M. Rahman, D. Y. Goswami, E. K. Stefanakos, *et al.*, "Numerical analysis of charging and discharging performance of a thermal energy storage system with encapsulated phase change material," *Applied Thermal Engineering,* vol. 71, pp. 481-500, 2014.

[52] V. R. Voller, "An Overview of Numerical Methods for Solving Phase Change Problems," in *Advances in Numerical Heat Transfer*. vol. 1, ed Washington, D.C.: Taylor and Franscis, 1996.

[53] S. Marella, S. Krishnan, H. Liu, and H. S. Udaykumar, "Sharp interface Cartesian grid method I: An easily implemented technique for 3D moving boundary computations," *Journal of Computational Physics,* vol. 210, pp. 1-31, 2005.

[54] H. S. Udaykumar, R. Mittal, P. Rampunggoon, and A. Khanna, "A Sharp Interface Cartesian Grid Method for Simulating Flows with Complex Moving Boundaries," *Journal of Computational Physics,* vol. 174, pp. 345-380, 2001.

[55] H. Kim and M.-S. Liou, "Adaptive Cartesian sharp interface method for three-dimensional multi-phase flows," in *19th AIAA Computational Fluid Dynamics Conference, June 22, 2009 - June 25, 2009*, San Antonio, TX, United states, 2009.

[56] H.-J. Kim and M.-S. Liou, "Three dimensional cut-cell Cartesian method for interfacial discontinuity of multi-phase fluids," in *18th AIAA Computational Fluid Dynamics Conference, June 25, 2007 - June 28, 2007*, Miami, FL, United states, 2007, pp. 2035-2051.

[57] H.-J. Kim and M.-S. Liou, "Numerical analysis of compressible two-phase flows using cartesian cut-cell method," in *46th AIAA Aerospace Sciences Meeting and Exhibit, January 7, 2008 - January 10, 2008*, Reno, NV, United states, 2008.

[58] P. Lapka and P. Furmanski, "Fixed Cartesian grid based numerical model for solidification process of semi-transparent materials II: Reflection and refraction or transmission of the thermal radiation at the solid-liquid interface," *International Journal of Heat and Mass Transfer,* vol. 55, pp. 4953-4964, 2012.

[59] C.-F. Tai and J. N. Chung, "A direct numerical simulation of axisymmetric cryogenic two-phase flows in a pipe with phase change," *Computers and Fluids,* vol. 48, pp. 163-182, 2011.

[60] Y. Yang and H. S. Udaykumar, "Sharp interface Cartesian grid method III: Solidification of pure materials and binary solutions," *Journal of Computational Physics,* vol. 210, pp. 55-74, 2005.

[61] H. S. Udaykumar and L. Mao, "Sharp-interface simulation of dendritic solidification of solutions," *International Journal of Heat and Mass Transfer,* vol. 45, pp. 4793-4808, 2002.

[62] V. R. Voller, "A fixed grid numerical modelling methodology for convection-diffusion mushy region phase-change problems," *International Journal of Heat and Mass Transfer,* vol. 30, pp. 1709-1719, 1987.
[63] P. A. Galione, O. Lehmkuhl, J. Rigola, A. Oliva, and I. Rodriguez, "Numerical Simulations of Thermal Energy Storage Systems with Phase Change Materials," in *30th ISES Biennial Solar World Congress 2011*, 2011, pp. 4785-4796.
[64] V. John and J. Novo, "On (essentially) non-oscillatory discretizations of evolutionary convection–diffusion equations," *Journal of Computational Physics,* vol. 231, pp. 1570-1586, 2012.
[65] C. Gau and R. Viskanta, "Melting and Solidification of a Pure Metal on a Vertical Wall," *Journal of Heat Transfer,* vol. 108, pp. 174-181, 1986.
[66] D. McDaniel and N. Zabaras, "A Least-squares Front-tracking Finite Element Method Analysis of Phase Change with Natural Convection," *International Journal for Numerical Methods in Engineering,* vol. 37, pp. 2755-2777, 1994.
[67] N. Hannoun, "Resolving the Controversy over Tin and Gallium Melting in a Rectangular Cavity Heated from the Side," *Numerical Heat Transfer. Part B, Fundamentals,* vol. 44, pp. 253-276, 2003.
[68] D. Mansutti and E. Bucchignani, "On the Importance of Solid Deformations in Convection Dominated Liquid/Solid Phase Change of Pure Materials," *Applications of Mathematics,* vol. 56, pp. 117-136, 2011.
[69] M. Hribersek and G. Kuhn, "Conjugate Heat Transfer by Boundary-Domain Integral Method," *Engineering Analysis with Boundary Elements,* vol. 24, pp. 297-305, 2000.
[70] B. Gore and M. Tandale, "Review of Solar Cooking Using Latent Heat Storage," *Applied Mechanics and Materials,* vol. 592-594, pp. 1761-1765, 2014.
[71] B. Iverson, S. T. Broome, and N. P. Siegel, "Temperature Dependent Mechanical Property Testing of Nitrate Thermal Storage Salts," presented at the SolarPACES, Perpignan, France, 2010.
[72] N. Siegel, "Thermophysical Property Measurement of Nitrate Salt Heat Transfer Fluids," *Proceedings of ASME 2011 5th International Conference on Energy Sustainability,* p. 9, 2011.
[73] G. T. Shirole, M. G. Takwale, K. C. Mohite, and A. M. Pathak, "Evaluation of optical and thermal performance of community type parabolic solar cooker," in *29th Biennial Solar World Congress of the International Solar Energy Society, ISES 2009, October 11, 2009 - October 14, 2009*, Johannesburg, South africa, 2009, pp. 816-820.
[74] T. Eshetu, S. Desalegn, and V. Ramayya, "Development and Testing of a Regenerative Rechargable Solar Stove System," *ESME Journal,* vol. 5, pp. 25-33, December 2005 2005.
[75] P. Mishra, A. Chakraverty, and H. D. Banerjee, "Studies on physical and thermal properties of rice husk related to its industrial application," *Journal of Materials Science,* vol. 21, pp. 2129-2132, 1986.
[76] K. G. Mansaray and A. E. Ghaly, "Physical and Thermochemical Properties of Rice Husk," *Energy Sources,* vol. 19, pp. 989-1004, 1997.
[77] M. J. Ahmad and G. N. Tiwari, "Evaluation and comparison of hourly solar radiation models," *International Journal of Energy Research,* vol. 33, pp. 538-552, 2009.
[78] S. K. Shukla and S. K. Gupta, "Performance evaluation of concentrating solar cooker under Indian climatic conditions," in *2008 2nd International Conference on Energy Sustainability, ES 2008, August 10, 2008 - August 14, 2008*, Jacksonville, FL, United states, 2009, pp. 393-398.
[79] H. Zamani, M. Moghiman, and A. Kianifar, "Optimization of the parabolic mirror position in a solar cooker using the response surface method (RSM)," *Renewable Energy,* vol. 81, pp. 753-759, 2015.
[80] N. I. Ibrahim, F. A. Al-Sulaiman, S. Rahman, B. S. Yilbas, and A. Z. Sahin, "Heat transfer enhancement of phase change materials for thermal energy storage applications: A critical review," *Renewable and Sustainable Energy Reviews,* vol. 74, pp. 26-50, 2017.
[81] Y. Lin, Y. Jia, G. Alva, and G. Fang, "Review on thermal conductivity enhancement, thermal properties and applications of phase change materials in thermal energy storage," *Renewable and Sustainable Energy Reviews,* 2017.
[82] Z. Khan, Z. Khan, and A. Ghafoor, "A review of performance enhancement of PCM based latent heat storage system within the context of materials, thermal stability and compatibility," *Energy Conversion and Management,* vol. 115, pp. 132-158, 2016.
[83] L. Liu, D. Su, Y. Tang, and G. Fang, "Thermal conductivity enhancement of phase change materials for thermal energy storage: A review," *Renewable and Sustainable Energy Reviews,* vol. 62, pp. 305-317, 2016.

[84] P. D. Myers, T. E. Alam, R. Kamal, D. Y. Goswami, and E. Stefanakos, "Nitrate salts doped with CuO nanoparticles for thermal energy storage with improved heat transfer," *Applied Energy,* vol. 165, pp. 225-233, 2016.
[85] L. Zhong, X. Zhang, Y. Luan, G. Wang, Y. Feng, and D. Feng, "Preparation and thermal properties of porous heterogeneous composite phase change materials based on molten salts/expanded graphite," *Solar Energy,* vol. 107, pp. 63-73, 2014/09/01/ 2014.
[86] Z. Deng, X. Liu, C. Zhang, Y. Huang, and Y. Chen, "Melting behaviors of PCM in porous metal foam characterized by fractal geometry," *International Journal of Heat and Mass Transfer,* vol. 113, pp. 1031-1042, 2017.
[87] C. Zhang, L. Wu, and Y. Chen, "Study on Solidification of Phase Change Material in Fractal Porous Metal Foam," *Fractals,* vol. 23, p. 1540003, 2015.
[88] J. Fukai, Y. Hamada, Y. Morozumi, and O. Miyatake, "Improvement of thermal characteristics of latent heat thermal energy storage units using carbon-fiber brushes: experiments and modeling," *International Journal of Heat and Mass Transfer,* vol. 46, pp. 4513-4525, 2003/11/01/ 2003.
[89] T. Wang, S. Wang, R. Luo, C. Zhu, T. Akiyama, and Z. Zhang, "Microencapsulation of phase change materials with binary cores and calcium carbonate shell for thermal energy storage," *Applied Energy,* vol. 171, pp. 113-119, 2016/06/01/ 2016.
[90] Y. Zhang, X. Wang, and D. Wu, "Microencapsulation of n-dodecane into zirconia shell doped with rare earth: Design and synthesis of bifunctional microcapsules for photoluminescence enhancement and thermal energy storage," *Energy,* vol. 97, pp. 113-126, 2016/02/15/ 2016.
[91] C. W. Robak, T. L. Bergman, and A. Faghri, "Enhancement of latent heat energy storage using embedded heat pipes," *International Journal of Heat and Mass Transfer,* vol. 54, pp. 3476-3484, 2011/07/01/ 2011.
[92] N. Sharifi, S. Wang, T. L. Bergman, and A. Faghri, "Heat pipe-assisted melting of a phase change material," *International Journal of Heat and Mass Transfer,* vol. 55, pp. 3458-3469, 2012/06/01/ 2012.
[93] A. M. Abdulateef, S. Mat, J. Abdulateef, K. Sopian, and A. A. Al-Abidi, "Geometric and design parameters of fins employed for enhancing thermal energy storage systems: a review," *Renewable and Sustainable Energy Reviews,* 2017.
[94] N. S. Dhaidan and J. M. Khodadadi, "Improved performance of latent heat energy storage systems utilizing high thermal conductivity fins: A review," *Journal of Renewable and Sustainable Energy,* vol. 9, p. 034103, 2017.
[95] B. Kamkari and H. Shokouhmand, "Experimental investigation of phase change material melting in rectangular enclosures with horizontal partial fins," *International Journal of Heat and Mass Transfer,* vol. 78, pp. 839-851, 2014.
[96] L.-W. Fan, Y.-Q. Xiao, Y. Zeng, X. Fang, X. Wang, X. Xu*, et al.*, "Effects of melting temperature and the presence of internal fins on the performance of a phase change material (PCM)-based heat sink," *International Journal of Thermal Sciences,* vol. 70, pp. 114-126, 2013.
[97] W.-B. Ye, "Enhanced latent heat thermal energy storage in the double tubes using fins," *Journal of Thermal Analysis and Calorimetry,* vol. 128, pp. 533-540, 2016.
[98] A. Khalifa, L. Tan, A. Date, and A. Akbarzadeh, "A numerical and experimental study of solidification around axially finned heat pipes for high temperature latent heat thermal energy storage units," *Applied Thermal Engineering,* vol. 70, pp. 609-619, 2014.
[99] S. Kuboth, A. König-Haagen, and D. Brüggemann, "Numerical Analysis of Shell-and-Tube Type Latent Thermal Energy Storage Performance with Different Arrangements of Circular Fins," *Energies,* vol. 10, p. 274, 2017.
[100] Y. Kozak, T. Rozenfeld, and G. Ziskind, "Close-contact melting in vertical annular enclosures with a non-isothermal base: Theoretical modeling and application to thermal storage," *International Journal of Heat and Mass Transfer,* vol. 72, pp. 114-127, 2014.
[101] W. Ogoh and D. Groulx, "Effects of the number and distribution of fins on the storage characteristics of a cylindrical latent heat energy storage system: a numerical study," *Heat and Mass Transfer,* vol. 48, pp. 1825-1835, 2012.
[102] R. W. Berg and D. H. Kerridge, "The NaNO(3)/KNO(3) system: the position of the solidus and sub-solidus," *Dalton Trans,* pp. 2224-9, Aug 07 2004.
[103] B. Iverson, "Thermal Property Testing of Nitrate Thermal Storage Salts in the Solid-Phase," *Proceedings of ASME 2011 5th International Conference on Energy Sustainability,* 2011.

[104] Y. Nagasaka and A. Nagashima, "The Thermal Conductivity of Molten NaNO3 and KNO3," *International Journal of Thermophysics,* vol. 12, pp. 769-781, 1991.
[105] A. Kruizenga, D. Gill, M. LaFord, and G. McConohy, "Corrosion of high temperature alloys in solar salt at 400, 500, and 680 degrees Celsius," Sandia National Laboratories, Albuquerque, New Mexico2013.
[106] R. Serrano-Lopez, J. Fradera, and S. Cuesta-Lopez, "Molten salts database for energy applications," *Chemical Engineering and Processing,* vol. 73, pp. 87-103, 2013.
[107] Á. G. Fernández, S. Veliz, E. Fuentealba, and H. Galleguillos, "Thermal characterization of solar salts from north of Chile and variations of their properties over time at high temperature," *Journal of Thermal Analysis and Calorimetry,* 2016.
[108] C. M. Kramer and C. J. Wilson, "The phase diagram of NaNO3-KNO3," *Thermochimica Acta,* vol. 42, pp. 253-264, 1980.
[109] D. J. Rogers, George, "Melting-crystallization and Premelting Properties of $NaNO_3$-KNO_3 Enthalpies and Heat Capacities," *Jounral of Chermical Engineering Data,* vol. 27, pp. 424-428, 1982.
[110] C. Martin, T. Bauer, and H. Müller-Steinhagen, "An experimental study of a non-eutectic mixture of KNO3 and NaNO3 with a melting range for thermal energy storage," *Applied Thermal Engineering,* vol. 56, pp. 159-166, 2013.
[111] N. Pfleger, T. Bauer, C. Martin, M. Eck, and A. Worner, "Thermal energy storage - overview and specific insight into nitrate salts for sensible and latent heat storage," *Beilstein J Nanotechnol,* vol. 6, pp. 1487-97, 2015.
[112] H. Mehling, C. Barreneche, A. Solé, and L. F. Cabeza, "The connection between the heat storage capability of PCM as a material property and their performance in real scale applications," *Journal of Energy Storage,* vol. 13, pp. 35-39, 2017.
[113] M. Augspurger, K. K. Choi, and H. S. Udaykumar, "Optimizing fin design for a PCM-based thermal storage device using dynamic Kriging," *International Journal of Heat and Mass Transfer,* vol. 121, pp. 290-308, 2018.
[114] M. Augspurger and H. S. Udaykumar, "Transient multi-day simulations of thermal storage and heat extraction for a finned solar thermal storage device," *Solar Energy,* vol. 151, pp. 48-60, 2017.
[115] M. Augspurger and H. S. Udaykumar, "A Cartesian grid solver for simulation of a phase-change material (PCM) solar thermal storage device," *Numerical Heat Transfer, Part B: Fundamentals,* vol. 69, pp. 179-196, 2016.
[116] D. D. Gray and A. Giorgini, "The validity of the boussinesq approximation for liquids and gases," *International Journal of Heat and Mass Transfer,* vol. 19, pp. 545-551., 1976.
[117] J. M. Mahdi and E. C. Nsofor, "Melting enhancement in triplex-tube latent thermal energy storage system using nanoparticles-fins combination," *International Journal of Heat and Mass Transfer,* vol. 109, pp. 417-427, 2017.
[118] H. Shmueli, G. Ziskind, and R. Letan, "Melting in a vertical cylindrical tube: Numerical investigation and comparison with experiments," *International Journal of Heat and Mass Transfer,* vol. 53, pp. 4082-4091, 2010.
[119] P. A. Galione, O. Lehmkuhl, J. Rigola, A. Oliva, and I. Rodriguez, "Numerical Simulations of Thermal Energy Storage Systems with Phase Change Materials," 2011.
[120] A. Keheirabadi and D. Groulx, "Simulating Phase Change Heat Transfer Using Comsol and Fluent: Effect of the Mushy Zone Constant," *Computational Thermal Sciences,* vol. 7, pp. 427-440, 2015.
[121] Y. Kozak and G. Ziskind, "Novel enthalpy method for modeling of PCM melting accompanied by sinking of the solid phase," *International Journal of Heat and Mass Transfer,* vol. 112, pp. 568-586, 2017.
[122] R. R. Kasibhatla, A. König-Haagen, F. Rösler, and D. Brüggemann, "Numerical modelling of melting and settling of an encapsulated PCM using variable viscosity," *Heat and Mass Transfer,* vol. 53, pp. 1735-1744, 2016.
[123] M. Faden, A. König-Haagen, S. Höhlein, and D. Brüggemann, "An implicit algorithm for melting and settling of phase change material inside macrocapsules," *International Journal of Heat and Mass Transfer,* vol. 117, pp. 757-767, 2018.
[124] A. Lazaro, C. Penalosa, A. Sole, G. Diarce, T. Haussmann, M. Fois*, et al.*, "Intercompariative tests on phase change materials characterization with differential scaning calorimeter," *Applied Energy,* vol. 109, pp. 415-420, 2013.

[125] A. Lomonaco, D. Haillot, E. Pernot, E. Franquet, and J.-P. Bedecarrats, "Sodium nitrate thermal behavior in latent heat thermal energy storage: A study of the impact of sodium nitrite on melting temperature and enthalpy," *Solar Energy Materials and Solar Cells,* vol. 149, pp. 81-87, 2016.
[126] T. Bauer, L. Dort, K. Ulrike, and R. Tamme, "Sodium Nitrate for High Temperature Latent Heat Storage," presented at the 11th International Conference on Thermal Energy Storage, Effstock, 2008.
[127] N. Sharifi, T. L. Bergman, and A. Faghri, "Enhancement of PCM melting in enclosures with horizontally-finned internal surfaces," *International Journal of Heat and Mass Transfer,* vol. 54, pp. 4182-4192, 2011.
[128] M. Eslami and M. A. Bahrami, "Sensible and latent thermal energy storage with constructal fins," *International Journal of Hydrogen Energy,* vol. 42, pp. 17681-17691, 2017.
[129] H. Eslamnezhad and A. B. Rahimi, "Enhance heat transfer for phase-change materials in triplex tube heat exchanger with selected arrangements of fins," *Applied Thermal Engineering,* vol. 113, pp. 813-821, 2017.
[130] S. Paria, S. Baradaran, A. Amiri, A. A. D. Sarhan, and S. N. Kazi, "Performance evaluation of latent heat energy storage in horizontal shell-and-finned tube for solar application," *Journal of Thermal Analysis and Calorimetry,* vol. 123, pp. 1371-1381, 2016.
[131] S. Almsater, W. Saman, and F. Bruno, "Performance enhancement of high temperature latent heat thermal storage systems using heat pipes with and without fins for concentrating solar thermal power plants," *Renewable Energy,* vol. 89, pp. 36-50, 2016.
[132] A. Sciacovelli, F. Gagliardi, and V. Verda, "Maximization of performance of a PCM latent heat storage system with innovative fins," *Applied Energy,* vol. 137, pp. 707-715, 2015.
[133] A. Pizzolato, A. Sharma, K. Maute, A. Sciacovelli, and V. Verda, "Topology optimization for heat transfer enhancement in Latent Heat Thermal Energy Storage," *International Journal of Heat and Mass Transfer,* vol. 113, pp. 875-888, 2017.
[134] R. Alayil and C. Balaji, "Conjugate Heat Transfer in Latent Heat Thermal Storage System with Cross Plate Fins," *Journal of Heat Transfer,* vol. 137, 2015.
[135] H. S. Udaykumar, "Eulerian-Lagrangian front tracking method for immersed boundaries," in *ASME International Mechanical Engineering Congress*, 1998, pp. 33-46.
[136] M. Morris, "Factorial Sampling Plans for Preliminary Computational Experiments," *Technometrics,* vol. 33, pp. 161-174, 1991.
[137] A. Forrester, A. Soberst, and A. Keane, *Engineering Design via Surrogate Modeling*. West Sussex: Wiley, 2008.
[138] L. Zhao, K. Choi, and I. Lee, "A Metamodeling Method Using Dynamic Kriging and Sequential Sampling," presented at the 13th AIAA/ ISSMO Multidisciplinary Analysis and Optimization Conference, Fort Worth, Texas, 2010.
[139] L. Zhao, K. K. Choi, and I. Lee, "Metamodeling Method Using Dynamic Kriging for Design Optimization," *AIAA Journal,* vol. 49, pp. 2034-2046, 2011.
[140] J. Arora, *Introduction to Optimum Design*, Third Edition ed. Amsterdam, Netherlands: Elsevier, 2012.
[141] O. Sen, "Evaluation of Kriging Based Surrogate Models Constructed from Mesoscale Computations of Shock Interaction with Particles."
[142] R. Dunlap, *Sustainable Energy*, SI Edition ed. Boston, MA: Cengage Learning, 2016.
[143] L. Nkhonjera, T. Bello-Ochende, G. John, and C. K. King'ondu, "A review of thermal energy storage designs, heat storage materials and cooking performance of solar cookers with heat storage," *Renewable and Sustainable Energy Reviews,* 2016.
[144] O. Sen, S. Davis, G. Jacobs, and H. S. Udaykumar, "Evaluation of convergence behavior of metamodeling techniques for bridging scales in multi-scale multimaterial simulation," *Journal of Computational Physics,* vol. 294, pp. 585-604, 2015.
[145] L. Zhao, K. K. Choi, and I. Lee, "Response Surface Method Using Sequential Sampling for Reliability-Based Design Optimization," presented at the Proceedings of the ASME 2009 International Design Engineering Technical Conferences, San Diego, CA, 2009.
[146] S. Jeong, M. Murayama, and K. Yamamoto, "Efficient Optimization Design Using Kriging Model," *Journal of Aircraft,* vol. 42, pp. 413-420.
[147] G. Bohling. (2005). *Kriging*.

[148] N. Gaul, "Modified Bayesian Kriging for Noisy Response Problems and Bayesian Confidence-based Reliability-based Design Optimization," PhD, University of Iowa, Iowa City, 2014.